CHARACTERIZATION OF TWO-PHASE FLOW MORPHOLOGY EVOLUTION DURING BOILING VIA HIGH-SPEED VISUALIZATION

by

Carolina Mira Hernández

A Thesis

Submitted to the Faculty of Purdue University

In Partial Fulfillment of the Requirements for the degree of

Doctor of Philosophy

School of Mechanical Engineering

West Lafayette, Indiana

May 2019

THE PURDUE UNIVERSITY GRADUATE SCHOOL
STATEMENT OF COMMITTEE APPROVAL

Dr. Suresh V. Garimella, Co-chair
School of Mechanical Engineering
Dr. Justin A. Weibel, Co-chair
School of Mechanical Engineering
Dr. Eckhard A. Groll
School of Mechanical Engineering
Dr. Pavlos P. Vlachos
School of Mechanical Engineering
Dr. Shripad T. Revankar
School of Nuclear Engineering

Approved by:
Dr. Jay P. Gore
Head of the Graduate Program

To all the great mentors I have encountered in my life,
beginning with my loving parents

ACKNOWLEDGMENTS

I would like to express my gratitude to my advisors, Dr. Suresh V. Garimella and Dr. Justin A. Weibel, for their continuous support and valuable guidance during my studies at Purdue University. They have encouraged me to think both critically and creatively when approaching research questions. I truly appreciate their commitment and understanding as mentors.

I would also like to thank the members in my advisory committee, Dr. Eckhard A. Groll, Dr. Pavlos P. Vlachos and Dr. Shripad T. Revankar for their guidance. Collaboration with Dr. Eckhard A. Groll and Dr. Pavlos P. Vlachos challenged me to explore new research topics and expand my skills; I am grateful for their feedback and insight.

I have always admired the environment of cooperation and kindness in our diverse research group, which empowers the members to reach their potential. My lab mates, past and present, greatly helped me by generously sharing their ideas, time, good judgement and humor. Special thanks to Dr. Matthew Rau, Dr. Susmita Dash, Dr. Suchismita Sarangi, Dr. Pierre Valiorgue, Dr. Scott Flueckiger, Dr. Kevin Drummond, Dr. Han Hu, Aditya Chandramohan, Todd Kingston, Julián Castillo, Gaurav Patankar, Aakriti Jain, Taylor Allred, Matthew Clark, Rishav Roy, Sara Lyons and Casey Carter.

I would also like to acknowledge my friends, the ones that stayed in Colombia, and the ones that I met at Purdue. I thank the vote of confidence they gave me in crucial moments, and the numerous conversations that have enriched my perspective. Special thanks to Prof. Luis Santiago Paris, Dr. María José Cadena, Dr. David Restrepo, Dr. David Orrego, Óscar Díaz, Nicolás Guarín, William Sánchez and Carolina Vivas.

Finally, I would like to thank my parents, Augusto and María Helena, and sisters, Natalia, Juliana and Valeria, for their unconditional love and support. In the strong bond that our family shares, I find the confidence to pursue my dreams and the purpose that guides my path.

Financial support for my PhD studies and research was provided by the Colombia-Purdue Institute (CPI), and the Colombian Administrative Department for Science, Technology and Innovation (Colciencias).

TABLE OF CONTENTS

LIST OF TABLES

LIST OF FIGURES

NOMENCLATURE

A_c	jet unit cell area, s^2, mm^2
A_f	ratio of orifice area to cell area, $\pi/(4(s/d)^2)$, mm^2
Bl^*	modified boiling number, $(\pi/4)D^2q''/\dot{m}c_p(T_{sat}-T_j)$, -
corr	correlation, -
C	constants in heat transfer profile
c_p	fluid specific heat, J kg^{-1} K^{-1}
d	orifice diameter, mm
D	heat source diameter, mm
f	focal length, mm
h	local convective heat transfer coefficient, W m^{-2} K^{-1}
$\bar{h}$	area-averaged heat transfer coefficient, W m^{-2} K^{-1}
h_0	stagnation-point heat transfer coefficient, W m^{-2} K^{-1}
H	confinement gap height, mm
I	image intensity, -
k	liquid thermal conductivity, W m^{-}1 K^{-1}
k_1	first radial distortion coefficient mm^{-2}
l	orifice plate thickness, mm
$\dot{m}$	mass flow rate, kg s^{-1}
M	fluid molecular mass, kg mol^{-1}
N	number of jets in the array, -
Nu	local Nusselt number, hd/k, -
$\overline{\mathrm{Nu}}$	area-averaged Nusselt number, $\bar{h}d/k$. -
Nu_0	stagnation Nusselt number, h_0d/k, -
p_c	fluid critical pressure, kPa
p_{op}	operating pressure, kPa
Pr	liquid Prandtl number, $c_p\mu/k$, -
q''	heat flux, W cm^{-2}
r	radial distance from stagnation point, mm

r_{eq} equivalent radius of jet unit cell, $s/\sqrt{\pi}$, mm

R_p peak roughness, μm

Re Reynolds number, $\rho_j v_j d/\mu_j$, -

s jet-to-jet spacing and square unit cell dimension, mm

s_x pixel skew factor, -

t time, s

T temperature, K

T_s surface temperature, K

T_{sat} saturation temperature, K

ΔT_{sub} degree of subcooling (T_{sat} - T_j), K

u, v pixel coordinates, -

u_0, v_0 image principal point, -

v velocity, m s^{-1}

W correlation window, -

x, y, z world coordinates, mm

x_0, y_0, z_0 camera center of projection, mm

Greek symbols

α rotation angle of camera coordinate system about world coordinate axis, deg

θ contact angle of liquid-vapor interface, deg

μ fluid dynamic viscosity, Pa s

ρ fluid density, kg m^{-3}

σ heat transfer profile width parameter

Subscript

f evaluated at film temperature

j jet inlet condition

l left camera or image

nb nucleate boiling region

r right camera or image

ref reference heat transfer value for single-phase jet impingement

s	surface
sat	saturated condition
sp	single-phase heat transfer region
x	x-coordinate axis
y	y-coordinate axis
z	z-coordinate axis

ABSTRACT

Author: Mira Hernández, Carolina. PhD
Institution: Purdue University
Degree Received: May 2019
Title: Characterization of Two-Phase Flow Morphology Evolution during Boiling via High-Speed Visualization
Committee Chair: Suresh V. Garimella, Justin A. Weibel

Nucleate boiling is an efficient heat transfer mechanism that enables the dissipation of high heat fluxes at low temperature differences. Heat transfer phenomena during nucleate boiling are closely linked to the two-phase flow morphology that evolves in time and based on the operating conditions. In particular, the critical heat flux, which is the upper limit for the nucleate boiling regime, can be triggered by hydrodynamic mechanisms resulting from interactions between the liquid and vapor phases. The aim of this thesis is to characterize the two-phase flow morphology evolution during nucleate boiling at high heat fluxes in two configurations: pool boiling, and confined and submerged two-phase jet impingement. The characterization is performed via non-invasive, high-speed optical based diagnostic tools.

Experimental characterization of liquid-vapor interfaces during boiling is often challenging because the rapidly evolving vapor structures are sensitive to invasive probes and multiple interfaces can occlude one another along a line of sight. In this thesis, a liquid-vapor interface reconstruction technique based on high-speed stereo imaging is developed. Images are filtered for feature enhancement and template matching is used for determining the correspondence of local features of the liquid-vapor interfaces between the two camera views. A sampling grid is overlaid on the reference image and windows centered at each sampled pixel are compared with windows centered along the epipolar line in the target image to obtain a correlation signal. To enhance the signatures of true matches, the correlation signals for each sampled pixel are averaged over a short time ensemble correlation. The three-dimensional coordinates of each matched pixel are determined via triangulation, which yields a set of points in the physical world representing the liquid-vapor interface. The developed liquid-vapor interface reconstruction technique is a high-speed, flexible and non-invasive alternative to the various existing methods for phase-distribution mapping. This technique also has the potential to

be combined with other optical-based diagnostic tools, such as tomographic particle image velocimetry, to further understand the phase interactions.

The liquid-vapor interface reconstruction technique is used to characterize liquid-vapor interfaces above the heated surface during nucleate pool boiling, where the textured interface resulting from the boiling phenomena and flow interactions near the heated surface is particularly suited for reconstruction. Application of the reconstruction technique to pool boiling at high heat fluxes produces a unique quantitative characterization of the liquid-vapor interface morphology near heated surface. Analysis of temporal signals extracted from reconstructions indicate a clear transition in the nature of the vapor flow dynamics from a plume-like vapor flow to a release mode dominated by vapor burst events. Further investigation of the vapor burst events allows identification of a characteristic morphology of the vapor structures that form above the surface that is associated to the square shape of the heat source. Vapor flow morphology characterization during pool boiling at high heat fluxes can be used to inform vapor removal strategies that delay the occurrence of the critical heat flux during pool boiling.

As compared to pool boiling, nucleate boiling can be sustained up to significantly higher heat fluxes during two-phase jet impingement. The increases in critical heat flux are explained via hydrodynamic mechanisms that have been debated in the literature. The connection between two-phase flow morphology and the extension of nucleate boiling regime is investigated for a single subcooled jet of water that impinges on a circular heat source via high-speed visualization from two synchronized top and side views of the confinement gap. When boiling occurs under subcooled exit flow conditions and at moderate heat fluxes, the regular formation and collapse of vapor structures that bridge the heated surface and the orifice plate is observed, which causes significant oscillations in the pressure drop across. Under saturated exit flow conditions, the vapor agglomerates in the confinement gap into a bowl-like vapor structure that recurrently shrinks, due to vapor break-off at the edge of the orifice plate, and replenishes due to vapor generation. The optical visualizations from the top of the confinement gap provide a unique perspective and indicate that the liquid jet flows downwards through the vapor structure, impinges on the heated surface, and then flows underneath the vapor structure, as a fluid wall jet the keeps the heated surface wetted such that discrete bubbles continue to nucleate. At high heat fluxes, intense vapor generation causes the fluid wall jet to transition from a bubbly to a churn-like regime, and some liquid droplets are sheared off into the vapor structure. The origin of

critical heat flux appears to result from a significant portion of the liquid in the wall jet being deflected off the surface, and the remaining liquid film on the surface drying out before reaching the edge of the heater.

The flow morphology characterizations presented in this dissertation further the understanding of flow and heat transfer phenomena during nucleate boiling. In the pool boiling configuration, the vapor release process was quantitatively described; during two-phase jet impingement, a possible mechanism for critical heat flux was identified. Opportunities for future work include the utilization of image processing techniques to extract quantitative measurements from two-phase jet impingement visualizations. Also, the developed liquid-vapor interface reconstruction technique can be applied to a boiling situation with a simpler liquid-vapor interface geometry, such as film boiling, to generate benchmark data for validation and development of numerical models.

1. INTRODUCTION

1.1 Background

Boiling is an efficient heat transfer mechanism that is harnessed in a wide range of applications that require dissipation of high heat fluxes or involve high temperatures, such as, power generation, electronics cooling, materials processing, chemical processing and propulsion. Boiling has been extensively studied for decades in an effort to explain the complex and multiscale phase interactions involved and their effects on the heat transfer performance. However, many fundamental questions remain unanswered, and the design of most devices that use boiling as heat transfer mechanism still relies on empirical correlations applicable to specific configurations.

Detailed diagnostic tools are key for a better understanding of boiling phenomena, and can provide rich data sets for validation of transport models for multiphase flows. Conventionally, diagnostic tools include discrete measurements of temperature, pressure and flow rate. Invasive probes are sometimes used to determine average distributions of liquid and vapor phases [1]. High-speed imaging is commonly used for qualitative classification of flow morphology, and quantitative measurements on identifiable isolated bubbles. More complex tomographic approaches have been used in a few instances to determine phase distribution [2,3]. Recently, three-dimensional particle image velocimetry techniques have been applied to boiling situations to resolve the liquid velocity field [4,5]. However, there is a persistent need for techniques that provide temporally and spatially resolved measurements of properties over the flow field, and, in particular, enable tracking of the dynamically changing liquid-vapor interface.

Nucleate boiling is the preferred regime of operation in many applications because of the very high heat transfer performance. Continuous nucleation, growth and departure of vapor bubbles from the heated surface yields high heat transfer coefficients. The favorable heterogeneous conditions of the flow near the surface are interrupted when the critical heat flux is reached, and an insulating layer of vapor blankets the surface, which drastically reduces the heat transfer coefficient. Different configurations are used in nucleate boiling applications, which include pool and flow boiling under saturated and subcooled conditions. Pool boiling is advantageous because it precludes the need for pumping the liquid, but the nucleate boiling

regime is reduced as compared with flow boiling. During pool boiling at high heat fluxes from a horizontal upward facing surface, large vapor structures form and hover above the heated surface, which are fed by much smaller vapor columns that stem from the nucleation sites. Hydrodynamic theories [6,7] postulate that the large vapor structures limit the supply of liquid to the heated surface, and predict that critical heat flux will occur when the liquid underneath the vapor structures depletes during the hovering time, which causes blanketing of the heated surface with vapor. Quantitative characterization of these vapor structures is limited, and models for the critical heat flux based on the hydrodynamic theory assume that the vapor structures are spherical in order to estimate the hovering time using a force balance [7,8]. Detailed characterization of the morphology evolution of the vapor structures can lead to better predictive tools, and can be used to inform vapor removal strategies to delay the critical heat flux.

The use of a subcooled jet that impinges on the heated surface is an alternative to significantly extend the nucleate boiling regime beyond the critical heat flux that can be achieved with pool boiling at a low additional pumping power [9]. Several experimental studies have been performed and correlations have been developed to estimate the critical heat flux in two-phase jet impingement, with a special focus on free-surface jets [10,11]. However, a mechanistic understanding of the flow characteristics that lead to the extension of the nucleate boiling regime is still lacking. For confined and submerged jet impingement, which is a configuration favored for its flexibility and compactness, vapor removal and surface wetting by the liquid jet are potential mechanisms by which the occurrence of the critical heat flux is delayed. Flow morphology characterization is required to elucidate these mechanisms, but the formation of vapor structures inside the gap impedes the observation of flow phenomena close to the heated surface.

1.2 Objectives and Major Contributions

The main goals of the present work are to: (1) develop a three-dimensional liquid-vapor interface reconstruction technique based on high-speed stereo imaging, (2) exploit the developed technique to dynamically track liquid-vapor interfaces near the heated surface during nucleate pool boiling, and (3) understand the flow interactions that enable efficient nucleate boiling up to high heat fluxes during confined, submerged jet impingement.

A non-invasive liquid-vapor reconstruction technique based on high-speed stereo imaging is developed. A simple and flexible optical set up is used to capture stereoscopic images of a liquid-vapor interface, which consists of a single high-speed camera with a stereo adapter and diffuse front and back illumination. Feature information from the textured liquid-vapor interface is match between views to recover the three dimensional interface geometry. In the matching process, a short-time ensemble correlation is used to attenuate noise effects.

The developed technique is applied in the reconstruction of liquid-vapor interfaces during nucleate pool boiling of water. Very good reconstruction results are obtained for highly textured liquid-vapor interfaces near the heated surface, with the curvature of the lower part of large vapor structures and the connecting meniscus to the surface being appropriately captured. A transition in the behavior of vapor of structures above the heater with increasing heat flux is identified from a plume-like vapor flow to a vapor-bursting behavior. During the vapor burst events, a characteristic interface morphology is identified which is associated with the square shape of the heated surface.

Flow morphology during confined and submerged two-phase jet impingement of water is characterized from incipience up to critical heat flux via synchronized high-speed visualization from the top and side views of the confinement gap. Under subcooled exit flow conditions, the behavior of unsteady vapor structures inside the confinement gap induces strong oscillations in the pressure drop. Under saturated exit flow conditions, a characteristic dynamic behavior of a bowl-like vapor structure inside the confinement gap is established. The liquid jet flows downward through the bowl-like vapor structure, impinges on the surfaces and transforms into a wall jet, which confirms continual surface wetting as the mechanism for extension of the nucleate boiling regime. The unique observations from the top of the confinement gap indicate that the critical heat flux occurs when vigorous vapor generation diverts a considerable portion of the liquid away from the heated surface, and the remaining wetting portion dries out.

1.3 Organization of the Document

The document is organized into four chapters. Chapter 1 contains background information regarding the role of two-phase flow morphology during boiling heat transfer and presents the objectives and major contributions of this work. Chapter 2 reviews relevant literature regarding techniques for phase distribution mapping in two-phase flows, and characteristics of two-phase jet impingement heat transfer. Chapter 3 describes the development of a non-invasive stereoscopic

technique for reconstruction of liquid-vapor interfaces during boiling and analyzes the dynamic behavior of the liquid-vapor interfaces above the heated surface during a nucleate pool boiling case. Chapter 4 presents the characterization of two-phase flow morphology during confined and submerged jet impingement via synchronized high speed visualization from the top and the side of the confinement gap. Chapter 5 summarizes the conclusions of the studies presented in the thesis and proposes future research directions.

2. LITERATURE REVIEW

2.1 Experimental Methods for Phase Distribution Mapping

An ideal measurement system to scan the gaseous phase distribution and track the interface in a two-phase flow should be accurate, non-invasive, applicable to different flow configurations, easy to implement, and have high spatial and temporal resolution [12]. In practice, multiple different techniques have been developed with inherent tradeoffs in these traits, typically with an emphasis on characterizing dispersed bubbly flows.

Invasive probe-based techniques take advantage of the contrast in different physical properties, such as electrical impedance [13], refractive index [14] and thermal transport properties [15], to instantaneously detect the phase present at a single point in the flow. Temporally-averaged phase distributions in steady-state flows can be estimated by translating the probe across the domain. The capabilities of conductivity based probes have been extended to measure interfacial area concentration across different two-phase flow regimes by using multiple sensors that enable the measurement of independent interface velocity components, and by sensor miniaturization that resolves small bubbles and reduces deformation of the interface [13,16]. An extension of local probes, wire-mesh sensors use an electrode grid to determine the void fraction distribution over the mesh cross section at a high temporal resolution [17,18]. Flow disruption is the main concern in application of probes, wire-mesh sensors, or any invasive technique.

Non-invasive approaches include photon-attenuation-based tomography using X-rays or gamma rays, electrical impedance tomography, ultrasonic tomography, and direct imaging. Tomographic approaches provide multi-dimensional information of the phase distribution but require numerical reconstruction techniques based on inverse methods, which induce uncertainty [19]. X-ray and gamma-ray tomography estimate phase (density) distribution across two-phase flows by analyzing beam attenuation due to absorption [20]. High-energy photon tomography is capable of studying flows with complex gaseous structures and high void fractions, with multiple interfaces along a line of sight, due to the weak interaction for scattering between high energy photons and common fluids. To lessen noise effects, the most common X-ray tomographic configurations use a small focused beam that is raster-scanned through the domain, limiting the

temporal resolution [17,20]. Implementation of X-ray tomography is non-trivial because of the X-ray source requirements and safety precautions that need to be implemented. Electrical-impedance-based tomographic systems having electrodes at the wall of tank, pipe or channel are attractive because they are easy to implement. However, reconstruction is more challenging because of the complex dependence between the phase distribution and impedance. Ultrasonic-based tomography can be used in dispersed bubbly flows, however, its application is limited to low void fractions because a strong signal attenuation is induced by wave reflections at interfaces [19].

With the recent developments in high-speed and high-resolution digital imaging, direct imaging techniques can yield high-fidelity measurements for transparent fluids when visual access is available [20,21]. Direct imaging has been primarily applied to dispersed bubbly flows, where image processing algorithms are used to identify individual bubbles, which are usually approximated by ellipses to determine geometric and dynamic characteristics, such as, bubble volume, interfacial area, and velocity [21–23]. The main challenge is segmentation of individual bubbles when they appear overlapped in the captured images; failing to separate groups of bubbles can induce significant errors in phase distribution measurements. Bubble overlapping effects limit the application of direct imaging to flows with void fractions lower than ~10 % [21]. In detailed studies of single bubble dynamics, direct imaging from perpendicular views has been used to find a three-dimensional approximation to the bubble shape by estimating the closest ellipsoid consistent with the bubble silhouette in both views [24].

Direct imaging of the phase distribution can be combined with other optical-based techniques, such as, particle image velocimetry (PIV), to obtain a complete description of the flow field. Particle seeding allows the determination of velocities for the liquid phase, and, in dispersed bubbly flows, the velocity and distribution of the gaseous phase is determined via identification and tracking of single bubbles in the images. In two-phase PIV, the optical equipment and image processing algorithms are tailored to improve phase discrimination. Laser-induced fluorescence of the seeding particles is commonly used to reduce the flaring caused by reflections on the bubbles interfaces. In planar PIV, a separate imaging system that operates at a different wavelength can be used to capture shadow images of the bubbles, and obtain information of the dispersed phase [25,26]. In single-camera systems, dispersed bubbles are separated from seeding particles using a size-based filter [27–30]. Investigation via PIV of the

three-dimensional features of two-phase flows has also been explored. Three-dimensional liquid velocities measurement along with ellipsoidal bubble reconstruction has been achieved with a stereoscopic PIV setup to study single bubble dynamics [31]. In two-phase flow situations drastically different from bubbly flows, such as large vapor structures formed by boiling from a flat surface, three-dimensional flow characterization has also been performed; however, the gaseous phase reconstruction has been limited to a coarse visual hull formed by the intersection of the projection cones from the vapor silhouettes in the different views [4,5]. Outside the scope of two-phase flows, tomographic PIV measurements have been performed around moving objects [32,33]. Three-dimensional reconstruction of the moving solid surface has been attempted via feature matching techniques [33].

2.2 Two-phase Jet Impingement Heat Transfer

Two-phase jet impingement is an attractive cooling technology that allows dissipation of high heat fluxes at low wall superheats [10,11,34,35]. During two-phase jet impingement, the mode of heat transfer depends on the surface heat flux. At low heat fluxes, single-phase heat transfer exists over the entire surface; the heat transfer coefficient is non-uniform across the surface, with a peak at the stagnation point directly under the jet orifice and lower values in the wall jet region approaching the periphery of the heated surface. As the heat flux increases, nucleate boiling initiates at the periphery of the surface, and creeps inwards toward the stagnation region [36–39]. Further increases in heat flux cause nucleate boiling to occur over the entire heated surface and a fully boiling regime is achieved. During fully boiling, the heat transfer coefficient across the surface is relatively uniform and insensitive to conditions of the liquid jet, such as velocity and subcooling [10,11,40–42]. Based on these observed heat transfer modes, Mira-Hernández *et al.* [43] developed and validated a semi-empirical model for predicting two-phase heat transfer from arrays of confined and submerged impinging jets. The model description and validation are included in APPENDIX C.

A key difference between boiling in a stagnant pool and fully boiling during jet impingement is that the inclusion of the jet significantly delays the occurrence of critical heat flux, which enables operation in the efficient nucleate boiling regime up to higher heat fluxes [10,11,40,42,44,45]. This phenomenon was reported by Katto and Kunihiro [40] while evaluating two alternatives to extend the nucleate boiling from a horizontal surface in a shallow

pool of water, namely, forced collapse of the vapor structures by mechanical means, and liquid supply to the surface by a saturated impinging jet. Improvements to critical heat flux using forced bubble collapse were limited by bubble dynamics. Much larger increases in critical heat flux were obtained using the saturated impinging jet. The authors suggested that the critical heat flux in the presence of the impinging jet occurred when the liquid supply to the heated surface was hindered by splashing of the jet due to vapor generation at the surface.

A mechanistic understanding of critical heat flux during two-phase jet impingement is still lacking. Several studies have experimentally measured the critical heat flux in free surface jets and developed empirical correlations [10,11,44,46–50]. The functional form of the empirical correlations has been determined either from dimensional analysis or by considering possible mechanisms that can trigger critical heat flux [10]. Lienhard and Eichhorn [46] applied a mechanical energy stability criterion to the case of a free surface jet impinging on a flat surface, and postulated that critical heat flux occurs when the kinetic energy of the upward vapor flow exceeds the energy expended in the formation of droplets that shear away from the heated surface. Monde [47] proposed a different mechanism for critical heat flux for a free surface impinging jet, which postulated that the jet supplies liquid to the heated surface via a thin liquid layer that exists underneath large vapor bubbles. The vapor generated at the surface flows upwards across the thin liquid layer in the form of discrete vapor columns into the large vapor bubbles. The critical heat flux condition is reached when the liquid film fed by the jet dries out. In both studies [46,47], the critical heat flux is found to be proportional to the cube root of the jet velocity. This functional dependency has been confirmed in several experimental studies for free-surface jets under moderate velocities and near atmospheric pressures [10,11]. Other functional dependencies have been identified under less common operating conditions, such as at very low or very high jet velocities and near critical pressures [48,50].

For confined, submerged two-phase jet impingement, fewer parametric studies of the critical heat flux phenomenon have been performed despite the suitability of this configuration for compact electronics cooling. Mudawar and Wadsworth [44] performed an experimental study on critical heat flux for planar confined jets of FC-72 and developed an empirical correlation for moderate jet velocities that predicts a considerably stronger dependence on jet velocity than in the case of free-surface jets; this was attributed to flow confinement effects that prevent the bulk flow of liquid from separating from the heated surface [44]. For high jet velocities, a reduction in

the critical heat flux with increase in velocity was observed, which was attributed to entrapment of vapor bubbles that have insufficient momentum to enter the bulk flow. In experiments with HFE-7100, Clark *et al.* [42] found a linear relation between critical heat flux and jet velocity.

3. THREE-DIMENSIONAL LIQUID-VAPOR INTERFACE RECONSTRUCTION FROM HIGH-SPEED STEREO IMAGES DURING POOL BOILING

The current investigation aims to extend the capabilities of direct imaging for gaseous phase distribution mapping beyond dispersed bubbly flows, to dynamically track complex liquid-vapor interfaces with a high-speed, flexible and non-invasive technique. The proposed technique uses template matching between stereoscopic views to reconstruct the three-dimensional interface shape; it is applicable to two-phase flow structures having rippled or otherwise textured interfaces and has the potential to be combined with other optical-based diagnostic tools, such as tomographic PIV.

The technique is applied to a particular case of pool boiling from a finite heat source, where highly textured bubbles are found near the heated surface. During pool boiling, quantitative characterization of vapor flow dynamics has been limited to discrete bubble departure at low heat fluxes [51]. At high heat fluxes, optical visualization has been generally limited to qualitative observations [52,53], except for approximation of the departure diameter of large vapor structures [8]. Conductivity probes have been used to determine the departure frequency of large vapor structures [54] and the time-averaged void fraction distribution [1]. The current work yields a unique characterization of the liquid-vapor interface morphology near the heated surface during pool boiling at high heat fluxes, which offers insight into the vapor release mechanisms that may lead to critical heat flux. A version of this chapter has been accepted for publication in the International Journal of Heat and Mass Transfer.

3.1 Experimental Methods

3.1.1 Experimental Setup

The liquid-vapor interface reconstruction approach is applied to pool boiling from a heated surface occurring inside a sealed test section. Figure 3.1a is a schematic illustration of the test section for the pool boiling experiment. The walls of the test section are made of 19 mm-thick polyether ether ketone (PEEK) slabs to provide insulation. The front and rear walls have glass viewing windows of 76 mm height and 50 mm width. The 27.2 mm × 27.2 mm square

heated surface is located at the bottom center of the test section and has an arithmetic average roughness of 0.63 μm. This heated surface forms the top of a copper block which consists of a top neck of small square cross-section that widens at the bottom to form a base with larger square cross-section. Twelve 150 W cartridge heaters are inserted into the base of the copper block. Rakes of T-type thermocouples (± 0.35 K) are positioned along the top neck of the copper block to determine the heat flux at the surface and extrapolate the surface temperature, assuming one-dimensional conduction.

The test section is filled with deionized water to a level of ~90 mm above the heater. The vapor generated from the boiling process is condensed on the surface of a copper coil located at the top of the test section, through which cold water flows. Two 170 W auxiliary immersion heaters are used to maintain saturated conditions inside the pool and for degassing. A pressure transducer (Omegadyne PX409) is installed to measure the pressure (and hence saturation temperature) inside the test section. The uncertainty in the saturation temperature (±0.12°C) is evaluated based on the manufacturer-quoted uncertainty for the pressure transducer. Additional details about the test section can be found in Ref. [55].

Figure 3.1b presents the optical setup to acquire stereoscopic images of the liquid-vapor interface during pool boiling. Images are acquired with a single high-speed camera (Phantom Veo 710L) at 2000 fps using a stereo adapter. The stereo adapter (Loreo 3D Macro LA9006) allows simultaneous capture of two different views with a single sensor, obtaining images such as those presented in Figure 3.1c. Front illumination is achieved with two arc lamps symmetrically positioned with respect to the front viewing window. Backlighting through the rear viewing window is achieved with an array of light emitting diodes (LEDs). The intensity of the light sources is adjusted to obtain good contrast of the texture on the front liquid-vapor interface while preserving a sharp vapor silhouette.

The stereo adapter has an approximate stereo base line of 20 mm and an adjustable focusing range of 230 to 850 mm. The closest focusing range is used and the aperture is set such that objects located 30 mm behind or in front of the center of the heated surface are in focus. The short stereo base line, obtained by using the stereo adapter instead of a two-camera system, reduces the relative distortion between the left and right views, favoring the correlation-based stereo correspondence search (described later in Section 3.2.4), and decreases the incidence of

occlusion [56]. However, sensitivity to changes in depth is reduced, requiring a sub-pixel resolution approach to be used during the correspondence search.

3.1.2 Pool Boiling Experimental Procedure

Before running the pool boiling experiments, the test section is degassed by vigorously boiling the water in the pool using the auxiliary immersion heaters. The vapor generated is condensed in a Graham reflux condenser that is installed at the top of the facility, while non-condensable gases vent out. After degassing for ~1 hr, flow of cold water through the condenser coil is initiated and controlled to maintain a constant pressure of 1 atm inside the chamber. The valve of the Graham reflux condenser is quickly closed. The power input to the immersion heaters is reduced and kept constant during the pool boiling experiment to maintain uniform, saturated conditions in the chamber.

During the saturated pool boiling experiment, power input to the heater block is incremented in steps from 148 W to 742 W, which correspond to measured heat fluxes at the surface of 17 to 92 W/cm^2. The power input is kept constant at each heat flux setting, and the system is allowed to reach steady state. At steady state, images are acquired for a total of 4 s; temperature and pressure data are acquired for ~75 s and averaged over this steady period.

3.2 Liquid-Vapor Interface Reconstruction

The liquid-vapor interface reconstruction process infers the three-dimensional interface position from the obtained stereo image pairs. For this purpose, it is necessary to identify pixels in the left and right views that correspond to the same point on the interface in the physical world, which is known as the correspondence problem [12]. Once the correspondences are determined, the geometric information about the camera system, which is known from the calibration process, is used to determine the three-dimensional coordinates of the matched points among the views. The specific steps in the liquid-interface reconstruction process are described in detail in the subsections that follow.

3.2.1 Camera Calibration Procedure

In order to obtain the mapping functions for the camera system, a calibration procedure is conducted prior to the experiment with a glass dot-matrix flat target having 0.5 mm-diameter

dots spaced 1.0 mm apart (Edmund Optics 59-217). For the calibration, the test section is filled with water at ambient temperature. The calibration target is placed parallel to the back wall of the test section, with the bottom line of calibration dots positioned ~5 mm above the heated surface, and translated through the depth of the volume of interest. Calibration images are taken at 2 mm increments for a total of 15 calibration planes. The calibration volume is 60 mm high, 40 mm wide, and 26 mm deep. The origin for the world coordinate system is located at the center of the heated surface, with the axes defined as shown in Figure 3.1.

Correspondences between physical world coordinates and pixel coordinates in each view are fitted independently to find pinhole-camera model parameters for the resulting left and right pseudo cameras. The camera parameters consist of the position and orientation of each pseudo camera, as well as focal length, optical center, pixel size, and distortion parameters. A first estimate of the pseudo-camera parameters is obtained following the procedure outlined by Tsai [57], in which distortion effects are neglected and the pixel size and pixel coordinates for the image center are assumed to be known. The estimate is further refined using the Levenberg-Marquardt optimization algorithm [58,59]. A standard pinhole-camera model for a single optical medium is fitted; parameters of the pinhole-camera model provide enough flexibility to account for the distortion effects due to the presence of the air-glass and glass-water optical interfaces [60]. The calibration image processing and estimation of pinhole camera parameters are performed with an in-house code using MATLAB [61]. The resulting pseudo-camera parameters after the calibration procedure are summarized in Table 3.1 (rotations of the pseudo-camera coordinate system about world coordinate axes are assumed to be applied in the order of x, y, and then z).

3.2.2 Image Rectification

The images captured with the high-speed camera using the stereo adapter are split vertically in stereo image pairs (left and right images) of equal width. To facilitate the correspondence search, the stereo image pairs are rectified. Image rectification allows the search of corresponding points between the images along horizontal scanlines, *i.e.*, a point in the right image that corresponds to a point in the left image will appear at the same vertical position but will have a horizontal shift. The horizontal shift in pixels in between corresponding points is known as disparity.

Image rectification is achieved through a geometric transformation of the coordinate systems of the left and right cameras. The transformation consists of a rotation that makes the optical axes of both cameras parallel to each other and perpendicular to the line connecting the centers of projection (origin of the camera coordinate system) of both cameras [62,63].

3.2.3 Vapor Masking and Feature Extraction

The correspondence search is performed on feature-filtered images instead of raw grayscale images. Performing the search on feature-filtered images helps to minimize the effects of unbalanced lighting in between the left and right views that occur in grayscale images. The brightness of corresponding regions in the left and right view may differ due to uncontrollable reflections and bubble lensing effects; also, the system of mirrors in the stereo adapter induces a shadowed region near the center of the camera sensor close to the merging line for both views, as can be seen in Figure 3.1c.

In order to extract the features in the liquid-vapor interface, a difference-of-Gaussian filter is applied to the grayscale images. The difference-of-Gaussian filter provides a close approximation to the scale-normalized Laplacian of Gaussian [64]. For the current data, a standard deviation of 1 pixel and a non-dimensional difference of 0.1 between scales are used. The field obtained after applying the difference of Gaussian is normalized by the standard deviation in intensity of the field inside the region of interest. Then, values greater than 1.0 are saturated and set to 1, values lower than 0.1 are set to 0. Figure 3.2a shows a sample grayscale left image and Figure 3.2b presents the feature-filtered version of this image. Most features are recovered with high contrast and the observable non-uniform illumination effects are clearly attenuated. In regions with poor illumination, like the bottom right corner of the sample image, the feature detection is moderately weaker.

To accelerate the correspondence search and to eliminate sources of error in the interface reconstruction, the search is restricted to the regions covered by vapor in each frame, which are dynamically masked. In the dynamic masking algorithm, visible elements from the background are eliminated by computing the difference between the grayscale images of the two-phase flow with a background image in the absence of vapor that is taken after the boiling test with the cartridge heaters turned off. Features are extracted from the image difference following the procedure described for grayscale images. Then, a Gaussian filter with a standard deviation of

2 pixels is applied to smooth noise resulting from the feature extraction procedure, and the image is binarized to obtain the boundaries of the vapor regions. A morphological closing operation is applied with a 3 pixels × 3 pixels circular structuring element to fill small gaps in the boundaries of the vapor regions. Finally, holes inside the boundaries of the vapor regions are selectively filled. Large holes with high intensity in the grayscale images are excluded because they are likely to be either a portion of the background surrounded by vapor bubbles, or smooth regions of large bubbles without the required feature information for the correspondence search. Figure 3.2c presents the resulting mask for the sample image in Figure 3.2a. The masking process is satisfactory but has a tendency to overestimate the vapor regions. The regions falsely detected as vapor are easily filtered during the generation of a surface representation for the liquid-vapor interface (Section 3.2.5).

3.2.4 Correspondence Search

Many algorithms have been proposed to estimate similarity between features on the images, establish the position of corresponding pixels, and impose smoothness assumptions [65]. In the present study, template matching based on correlation windows is used to estimate similarity between features, while a maximum correlation value criterion is used to establish the position of corresponding pixels. More complex approaches are available, such as comparison of feature descriptors that are less sensitive to distortion between views [66,67], or optimization techniques that explicitly handle surface smoothness [68]. However, template matching has a straightforward implementation and is widely used as the baseline to evaluate proposed algorithmic improvements.

The search algorithm compares a reference window in the left feature-filtered image with windows of the same size along the respective horizontal scan line in the right feature-filtered image. Correlation of the intensity values in the feature-filtered images is used to assess the similarity between two windows. The correlation is normalized by the mean and second moment of the intensity values in each window. The correlation is computed as:

$$corr = \frac{\sum_{W}\left(I_l - \bar{I}_l\right)\left(I_r - \bar{I}_r\right)}{\sqrt{\left[\sum_{W}\left(I_l - \bar{I}_l\right)^2\right]\left[\sum_{W}\left(I_r - \bar{I}_r\right)^2\right]}} \tag{3.1}$$

The correspondence search on the right image is limited to the range of expected disparities assuming the liquid-vapor interfaces are in the vicinity of the heater, - 150 pixels $\leq d \leq$ -115 pixels. For each reference pixel centered at a window in the left image, a correlation signal is computed with windows across the horizontal scan line on the right image within the disparity limits. For the results presented, windows of 30 pixels × 30 pixels are used, and pixels in the left (reference) image are sampled with a window overlap of 90%.

The matching or corresponding pixel should be located where the correlation signal reaches a maximum peak value. However, due to the presence of noise in the feature images, several peaks of comparable value can be detected in the correlation signal, which generates ambiguity in the correspondence search. To overcome this ambiguity, an ensemble correlation signal is computed by averaging the correlation signals at each pixel from the previous three frames, the current frame, and the following three frames. The false peaks should attenuate with the averaging process, while the peak coincident with the actual matching pixel should remain.

The ensemble correlation approach is widely used in PIV to find mean displacement fields when dealing with image sequences having low particle seeding [69,70]. This approach is beneficial for the liquid-vapor interface reconstruction problem because the texture on the interface evolves at a smaller time scale than the overall shape of the interface. Hence, the information used to estimate the correlation signal is different between frames, allowing improved inference of the three-dimensional interface position that is consistent between frames.

Once the ensemble correlation is computed, the pixel coordinate in the right image corresponding to the reference pixel is determined at the maximum peak value. To achieve subpixel accuracy in the correspondence estimate, the location of the correlation peak is estimated using a quadratic fit between the peak value and the two neighboring values.

Figure 3.3a presents the resulting disparity field when a single-frame correlation is used on the sample frame, while Figure 3.3b presents the results obtained with the seven-frame ensemble correlation. In the single-frame correlation, several patches of incorrect disparity values can be identified. The seven-frame ensemble correlation corrects these patches (see lower right region of the frame at the center of the bubble at the front of the heater). Figure 3.3c and Figure 3.3d present the relative magnitude of the first peak to the second peak in the correlation signal (peak-to-peak ratio) for the single-frame correlation and seven-frame ensemble correlation, respectively. The ambiguity in peak detection is reduced with the implementation of

the ensemble approach in some regions, such as the center of the bubble at the front of the heater. Remaining regions with high peak-to-peak ratio are boundary lines in between bubbles located at different depths, or regions where the ambiguity in the correspondence estimate is persistent. The most probable causes for persistent ambiguity are poor feature detection in regions with low contrast and contamination of the recovered features by ripples in an interface behind the front interface that can be seen due to transparency. This is a consequence of the transparency and specular reflectivity of vapor structures, which challenge the assumptions of opacity and diffuse reflectivity in stereo surface reconstruction.

3.2.5 Surface Representation of the Liquid-Vapor Interface

From each pair of corresponding pixels, the three-dimensional position of a point is computed using the geometric information of the camera system to obtain a cloud of points on the interface in space. To reconstruct the surface which corresponds to the liquid-vapor interface, a triangular mesh is chosen as a robust and simple surface representation.

The connectivity for the triangular mesh representation is established in the two-dimensional pixel domain for the set of pixels on the left image for which the disparity is estimated. Each isolated vapor region detected during the masking process is triangulated separately. Before computing the triangulation, each region is trimmed to eliminate small protruding features. If necessary, regions connected by a single pixel are split and triangulated separately.

The raw three-dimensional reconstruction of the liquid-vapor interface, represented as a triangular mesh, is shown in Figure 3.4a for the sample frame. Additional filtering is required to eliminate errors induced by incorrect correspondence estimates and to eliminate elements connecting bubbles that overlap in the images but are located at different depths. First, elements with high skewness and those for which the front face is not simultaneously visible in both views are eliminated. Small surface patches are then removed because they are likely to correspond to erroneous matches, tiny vapor bubbles, or noise induced in previous processing steps. Figure 4b presents the final liquid-vapor interface reconstruction for the sample frame. The reconstruction region extends vertically from the heat source up to 50 mm ($0 \text{ mm} \leq y \leq 50 \text{ mm}$), has a width of 40 mm centered around the heat source ($-20 \text{ mm} \leq x \leq 20 \text{ mm}$), and a depth of 40 mm also centered around the heater ($-20 \text{ mm} \leq z \leq 20 \text{ mm}$). Reconstruction of interfaces beyond the

calibration volume is justified by the robustness of the pinhole camera model. The liquid-vapor interface reconstruction is validated by imaging spherical representative samples, as described in the APPENDIX A.

3.3 Results and Discussion

3.3.1 Three-dimensional Reconstruction of Liquid-Vapor Interfaces

Figure 3.5 shows three-dimensional reconstruction results for a sequence of frames in which a large vapor structure grows and detaches from the heat source, while small and tiny vapor bubbles rise The sample frame used to describe the reconstruction process (Section 3.2) is taken as the initial frame, $t = 0$ ms. At this initial time, it can be seen in the grayscale images that the vapor structure attached to the surface, labeled as A, extends across the heat source width and has an irregular shape with a medium-sized bump on the right and two small bumps on the left. The three-dimensional reconstruction (Figure 3.5b and Figure 3.5c) for the large vapor structure adequately captures the irregular shape of the interface, exhibiting three bumps, and the necking of the interface towards the contact line with the heat source edge. Good three-dimensional reconstruction results are obtained from regions where the interface is textured, and the texture is captured with adequate contrast in the grayscale images. For example, the connecting meniscus is composed of many tiny vapor structures that originate on the heated surface and feed the large vapor structure. The tiny vapor structures provide a texture pattern that enables matching in the correspondence search. On the top part of the vapor structure, ripples on the liquid-vapor interface resulting from flow interactions are the features matched in the correspondence search. Poor feature detection occurs on the right edge of the left view and on the left edge of the right view because the optics in the stereo adapter cast a shadow near the line that divides both views on the camera sensor (see in Figure 3.1c); this introduces some minor artifacts in the reconstruction at the right bottom of the medium size bump and at the left-most small bump (Figure 3.5b and Figure 3.5c). Near the center of the medium-sized bump at the right of the frame, a patch is missing in the interface reconstruction. In this region, a bright spot with poor feature contrast is captured, caused by backlighting and bubble lensing effects; moreover, ambiguity is induced in the correspondence search because features from the rear interface are captured along with features from the front interface.

Also at the initial frame, $t = 0$ ms, a small bubble labeled as B is growing and departing from the heater as an elongated vapor slug behind the large vapor structure (bubble A) on the left. Above and behind the vapor structure (bubble A) on the right of the frame, two small bubbles are rising and are labeled as C and D, one behind the other. The small bubbles B, C and D are rather smooth with little texture on the interface to match. The correspondence is mainly established between the silhouettes on both views and grayscale intensity gradients caused by the illumination and bubble lensing effects. Hence, these small bubbles are reconstructed as jagged surface patches confined to a narrow depth interval that can be used for estimation of the bubbles location in space. The tiny bubbles in the upper part of the grayscale image are absent in the three-dimensional reconstruction because they are filtered along with small noisy interface patches during the generation of a surface representation of the interface, as described in Section 3.2.5.

As time progresses, the vapor structure (bubble A) grows ($t = 15$ ms), and its shape becomes similar to a mushroom cap as the meniscus connecting to the heated surface starts to detach ($t = 30$ ms). As the vapor structure starts to detach form the surface ($t = 30$ ms), the interface becomes smooth enough that grayscale intensity gradients due to illumination dominate in the correspondence search and the vapor structure interface is reconstructed as a set of jagged patches. In the region close to the surface, the meniscus attached to the heat source edge is adequately reconstructed. The interface geometry and dynamics are best captured near the heat source, where the boiling behavior generates distinctive features that can be appropriately matched between left and right views.

3.3.2 Behavior of Liquid-Vapor Interface near the Heated Surface during Pool Boiling

Table 3.2 lists the heat fluxes for the pool boiling cases considered, along with the corresponding surface superheat (difference between the heated surface temperature and the saturation temperature). The observed heat transfer behavior is consistent with the well-known behavior for nucleate pool boiling. Most of the pool boiling cases considered lie in a regime with growing vapor mushroom structures. In this regime, vapor structures are formed near the heated surface by the coalescence of vapor bubbles from neighboring nucleation sites. The ‘vapor mushroom’ term is used to describe such vapor structures when they are attached to the heated

surface and fed by several columnar stems of vapor [53]. After a vapor mushroom leaves the surface, vapor again accumulates on the surface and new vapor mushrooms grow and coalesce.

At the lowest heat flux for which the liquid-vapor interface is reconstructed, 36 W/cm^2, vapor mushrooms typically leave the surface as medium-sized bubbles, with widths comparable to half of the heat source side dimension, as can be seen in the sequence of grayscale images in Figure 3.6a. These bubbles form and rise frequently in groups, forming a plume strongly dominated by upward buoyancy forces. As the heat flux increases, vapor mushrooms become larger before departing from the surface and fan out beyond the heat source footprint. When large vapor structures depart, a strong trailing wake entrains vapor from the heated surface, forming a trailing slug which efficiently strips most vapor from the heater before new vapor mushroom structures form again grow. At the highest heat fluxes such as 82 W/cm^2, the formation and departure of large vapor mushrooms dominates, with bursts of vapor periodically leaving the surface (see sequence of grayscale images in Figure 3.7a).

Figure 3.6b and Figure 3.7b present a sequence of liquid-vapor interface reconstruction results for heat fluxes of 36 and 82 W/cm^2, respectively. The reconstruction adequately captures the general dynamics of the liquid-vapor interface near the heated surface. The front interface of the newly formed mushroom bubbles is consistently well reconstructed, as are lower portions of the larger mushroom bubbles where the meniscus connects to the heater surface. As the bubbles grow and depart from the surface, the liquid-vapor interface reconstruction further away from the heater is prone to the artifacts described in Section 3.3.1. Liquid-interface reconstruction fails for the lowest experimental heat flux, 17 W/cm^2, for which bubbles above the heater are small and without sufficient texture for their front interface to be reconstructed as a curved surface.

The median contact angle of the interface attached to the front edge of the heated surface is computed from reconstruction results in a region that extends 0.5 mm above the surface. The contact angle is defined as the angle between the interface and the heated surface measured across the liquid phase. When the vapor is removed from the heated surface and the interface recedes inwards toward the heat source, the contact angle tends to 180° ($\cos\theta = -1$). Conversely, when the vapor structures grow and extend beyond the heated footprint, the contact angle tends to 0° ($\cos\theta = 1$). The cosine of the contact angle is determined based on the dot product of the reconstructed interface normal and the heated surface normal. However, when the vapor structures extend beyond the heated surface footprint and the contact angle is very low, the

portion of the interface that attaches to the heated surface is not reconstructed due to visibility constraints. When this occurs, an approximation of this portion of the interface is found by connecting the reconstruction results to the heater edge. Hence, the contact angle is estimated from triangular elements 0.5 mm or less above the heated surface as the angle formed by the shortest ray connecting the centroid of the element and the heater front edge with the heated surface plane.

Figure 3.6c and Figure 3.7c present the temporal behavior of the cosine of the median contact angle of the liquid vapor interface attached to the front edge of the heater, shown for heat fluxes of 36 W/cm^2 and 82 W/cm^2, respectively. For the heat flux of 36 W/cm^2, the cosine of the contact angle signal has random fluctuations that are confined to a narrow range of mostly negative values, which is consistent with the observations from the grayscale images and the reconstructions of the vapor flowing in a plume dominated by buoyancy forces. For the heat flux of 82 W/cm^2, several events having similar characteristics are observed in the signal; the cosine of the contact angle rises quickly to a value close to unity, remains constant for some time, and then falls. These events correspond to the release of vapor bursts, for which large vapor mushrooms quickly form and hover over the surface before departing. The different behavior for the two cases is highlighted in their probability density functions for the cosine of the contact angle, presented in Figure 3.6d and Figure 3.7d. As the heat flux increases, the probability density function changes from a narrow and symmetric unimodal distribution to a wider distribution with a dominant peak near unity. The dominant peak close to unity for high heat fluxes is associated with the more frequent vapor burst events.

3.3.3 Liquid-Vapor Interface Morphology during Vapor Burst

During vapor burst events, large vapor mushrooms hover over the heated surface, preventing the liquid from rewetting the surface. Hydrodynamic theories [6,7] predict that critical heat flux will occur when the liquid macrolayer underneath the vapor mushroom depletes during the hovering time, which causes blanketing of the heated surface with vapor. Hence, characterization of the vapor burst release mechanism can provide insight into the critical heat flux phenomenon. At high heat fluxes, the vapor burst events have a characteristic signature in the cosine of the contact angle signals. This characteristic signature indicates that the liquid-vapor interface undergoes similar morphological changes during the evolution of the vapor burst

events. The interface morphology evolution of a characteristic vapor burst event is studied by combining interface reconstruction results for a set of vapor burst events extracted from the 82 W/cm^2 and 92 W/cm^2 heat flux cases.

The interface morphology of the characteristic vapor burst event is constructed by averaging reconstruction results for 33 vapor burst events aligned in time. Figure 3.8 presents the alignment of the interface contact angle signatures over all events, and confirms the similarity of the vapor burst events. The resulting average signature and bounds at one standard deviation are also presented. The average time that the liquid-vapor interface is pinned to the front edge of the heater is 26.7 ms, defined as the duration of the plateau in the cosine of the contact angle signal.

Figure 3.9 presents the evolution of the interface morphology for the characteristic vapor burst event. The formation of the vapor mushroom starts with detachment of the previous vapor mushroom and the development of a thin layer of vapor covering the heated surface (t = -15 ms). The thin layer is slightly non-uniform, with accumulation of vapor at the heat source corners because the detachment of the previous vapor mushroom progresses from the corners to the center of the heater. Hence, the new vapor layer develops first at the corners. As the vapor layer continues to grow, the accumulation of vapor at the corners accentuates, and the layer evolves into a lobed vapor structure that fans out beyond the heater footprint (t = 0 ms). Finally, the lobed vapor structure begins to detach, which causes the meniscus to recede (t = 15 ms). The interface lobed morphology is a consequence of the square shape of the heater, which favors the accumulation of vapor at the corners during the initial vapor mushroom formation. This finding warrants further investigation of the relation between the vapor mushroom morphology identified and the hovering time, as well as the effects of heater shape on the morphology and removal of vapor from the heated surface.

3.4 Conclusion

A liquid-vapor interface reconstruction technique using high-speed stereo imaging is implemented and applied to vapor structures formed above a finite heated surface during pool boiling. The technique extends the capabilities of using direct imaging for non-invasive three-dimensional phase-distribution mapping beyond dispersed bubbly flows, and is inherently compatible with other optical-based flow characterization techniques, such as tomographic PIV. The reconstruction procedure relies on feature extraction and matching between stereo views to

establish the three-dimensional coordinates of points lying on the liquid-vapor interface, and consequently requires textured interfaces. The feature correspondence search benefits from the use of ensemble correlation, which helps to attenuate the effects of false matches due to transparency effects and poor detection of features in low-contrast regions of the images. For textured interfaces close to the heated surface, an appropriate surface representation of the liquid-vapor interfaces is obtained that is suited to studying interface dynamics. The feasibility of using stereo imaging for three-dimensional phase distribution mapping is demonstrated using a straightforward implementation of template matching. Modifications in the optical set up can also advance the capabilities of the reconstruction technique; these include expanding the spatial and angular coverage with the utilization of more high-speed camera and stereo adapter sets.

The interface reconstruction technique is applied to mushroom-like vapor structures on top of the heated surface during pool boiling for a range of heat fluxes. The reconstruction technique produces good results for liquid-vapor interfaces close to the heated surface, where the interface is highly textured. Hence, the front interface of small vapor mushrooms attached to the heated surface, and the lower part of large vapor mushrooms where the meniscus connects to the surface, are appropriately captured. As the vapor mushrooms detach from the surface, the interface becomes smooth and the reconstruction results deteriorate. A transition is observed in the nature of the vapor structures with increasing heat flux from a plume-like vapor flow to a vapor release mode dominated by vapor burst events. The transition is discernible in the temporal data for the cosine of the contact angle of the interface attached to the front edge of the heat source, in which the vapor burst events have a characteristic signature. The probability density distributions for the cosine of the contact angle signals also reveal a clear distinction between the continuous vapor plume and vapor burst mode. For the continuous vapor plume release mode, the distribution is unimodal and restricted to a narrow range, while for the vapor burst mode, the distribution has a larger spread with a dominant peak near unity. A characteristic morphology evolution of the vapor structures during vapor burst events is identified. The square shape of the heater favors the accumulation of vapor at the corners at the early stages of the formation of large vapor mushrooms, which results in the development of lobed structures.

Table 3.1. Pinhole-camera model parameters obtained after calibration of the camera system.

Camera	Center of projection [mm]			Rotation angles [deg]			Focal length [mm]	Image center [-]		Pixel skew [-]	Radial distortion [mm^{-2}]
	x_0	y_0	z_0	α_x	α_y	α_z	f	u_0	v_0	s_x	k_1
Left	-7.3	34.7	342.1	1.1	172.1	-0.2	66.2	788.1	319.0	1.00	5.2×10^{-5}
Right	13.1	35.4	341.8	0.7	192.1	0.2	65.9	-304.2	332.7	1.00	4.5×10^{-5}

Table 3.2. Experimental pool boiling cases.

Heat flux q'' [W/cm^2]	Surface superheat, T_s - T_{sat} [K]
17	10.6
36	12.1
54	13.3
64	13.9
73	14.4
82	15.0
92	15.4

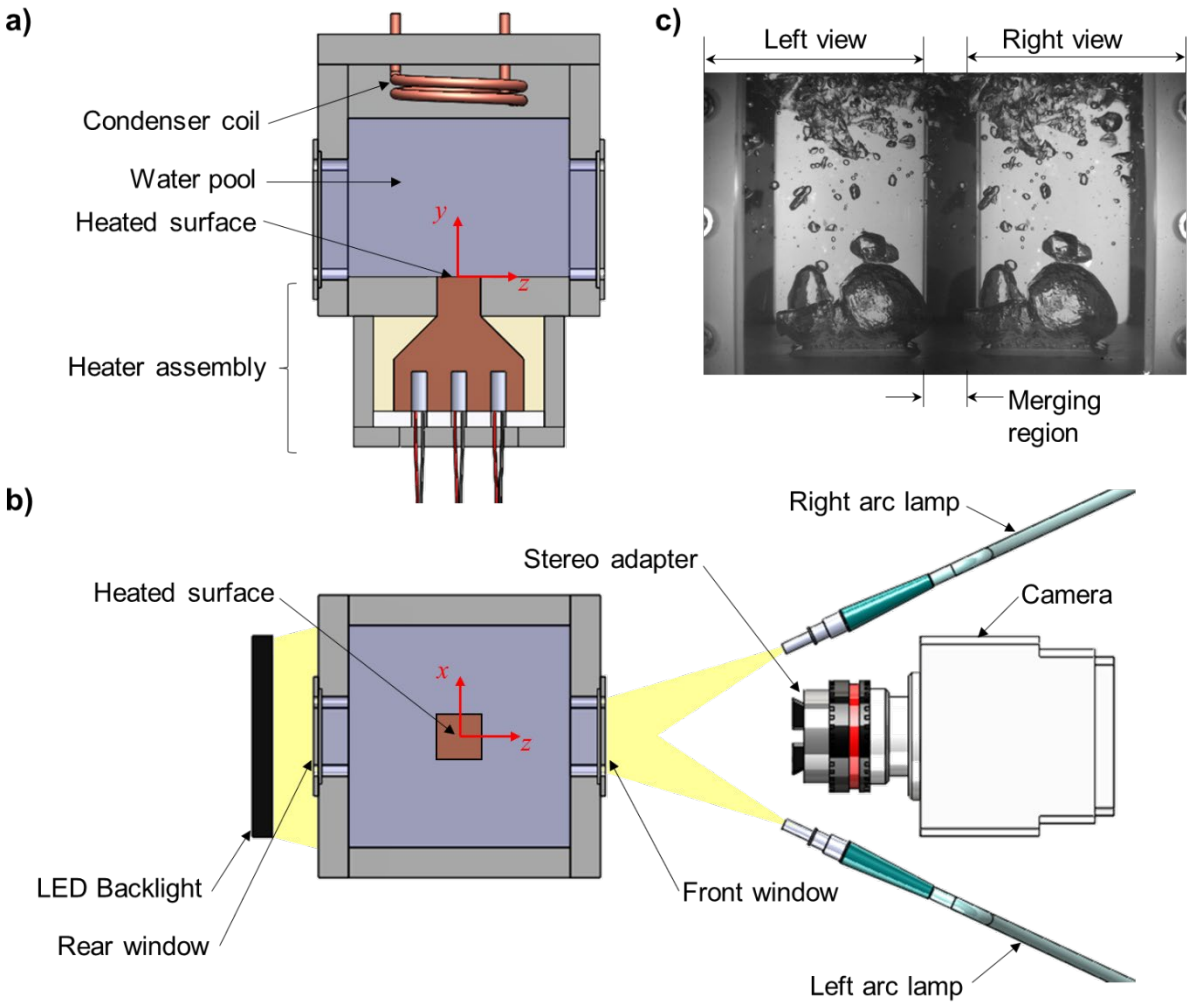

Figure 3.1. Schematic illustration of (a) the pool boiling experimental setup, (b) optical equipment, and (c) a sample grayscale stereoscopic image at 73 W/cm^2.

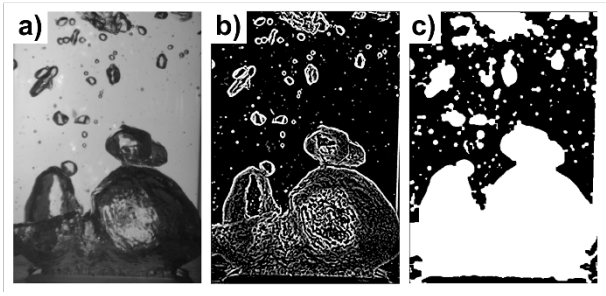

Figure 3.2. Sample (a) original left grayscale image, (b) featured-filtered image, and (c) vapor mask at 73 W/cm^2 (left view cropped to the region of interest).

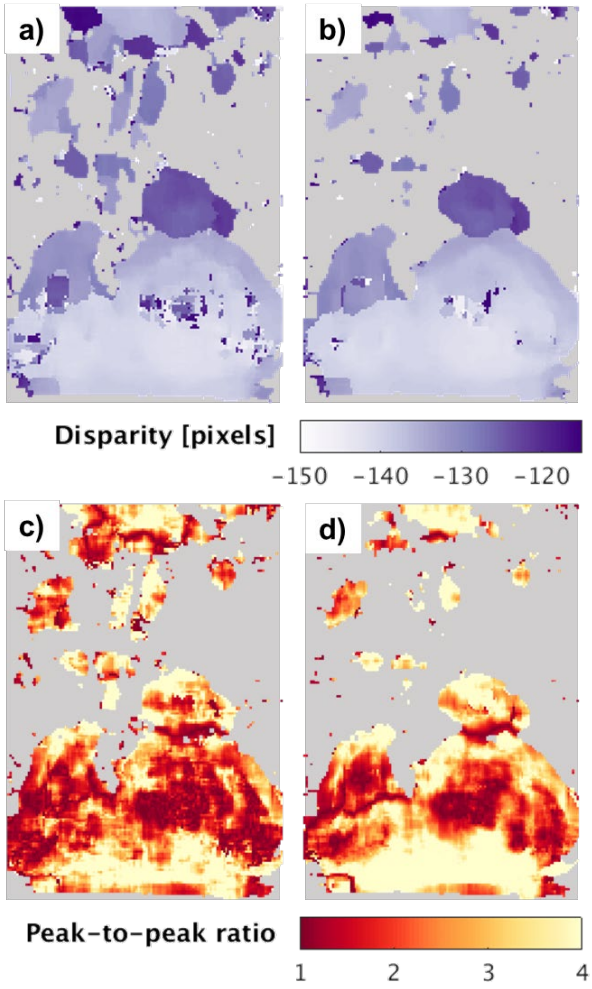

Figure 3.3. Disparity estimates with correlation-based template matching for (a) a single frame and (b) seven-frame ensemble correlation; ratio between first and second peak correlation values for (c) a single frame and (d) seven-frame ensemble correlation (shown for sample stereoscopic image at 73 W/cm^2).

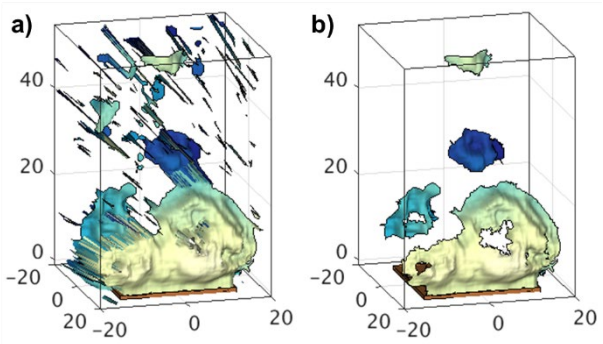

Figure 3.4. Three-dimensional views of reconstructed liquid-vapor interface (a) before and (b) after filtering based on the visibility constraint, element skewness, and size of surface patch (shown for sample stereoscopic image at 73 W/cm^2).

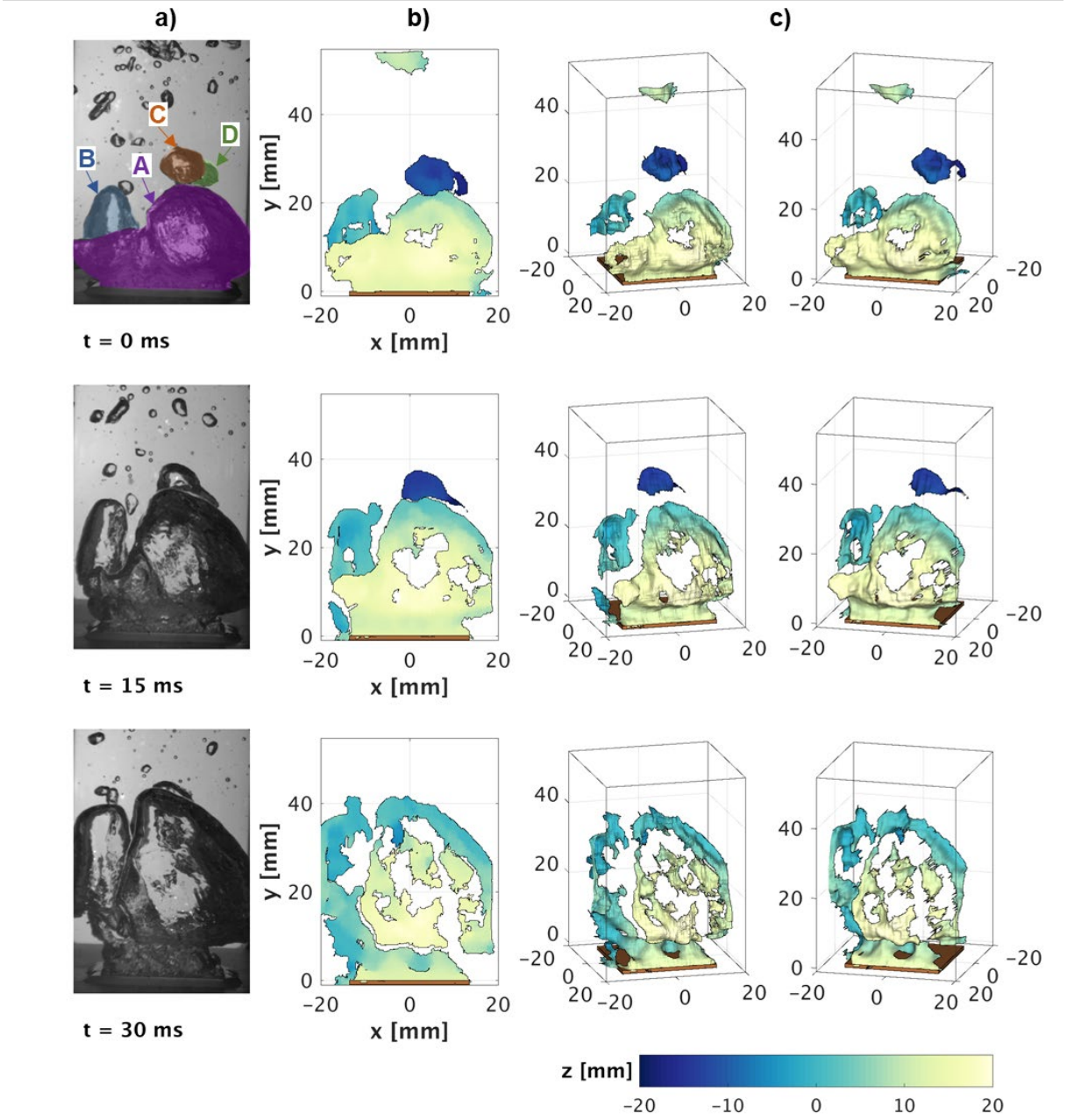

Figure 3.5. Sequence of (a) left grayscale images, (b) reconstructed map of the interface depth, and (c) three-dimensional views (as observed from two different angles) of the reconstructed interface for the growth of a mushroom-like bubble on top of the heated surface at 73 W/cm^2.

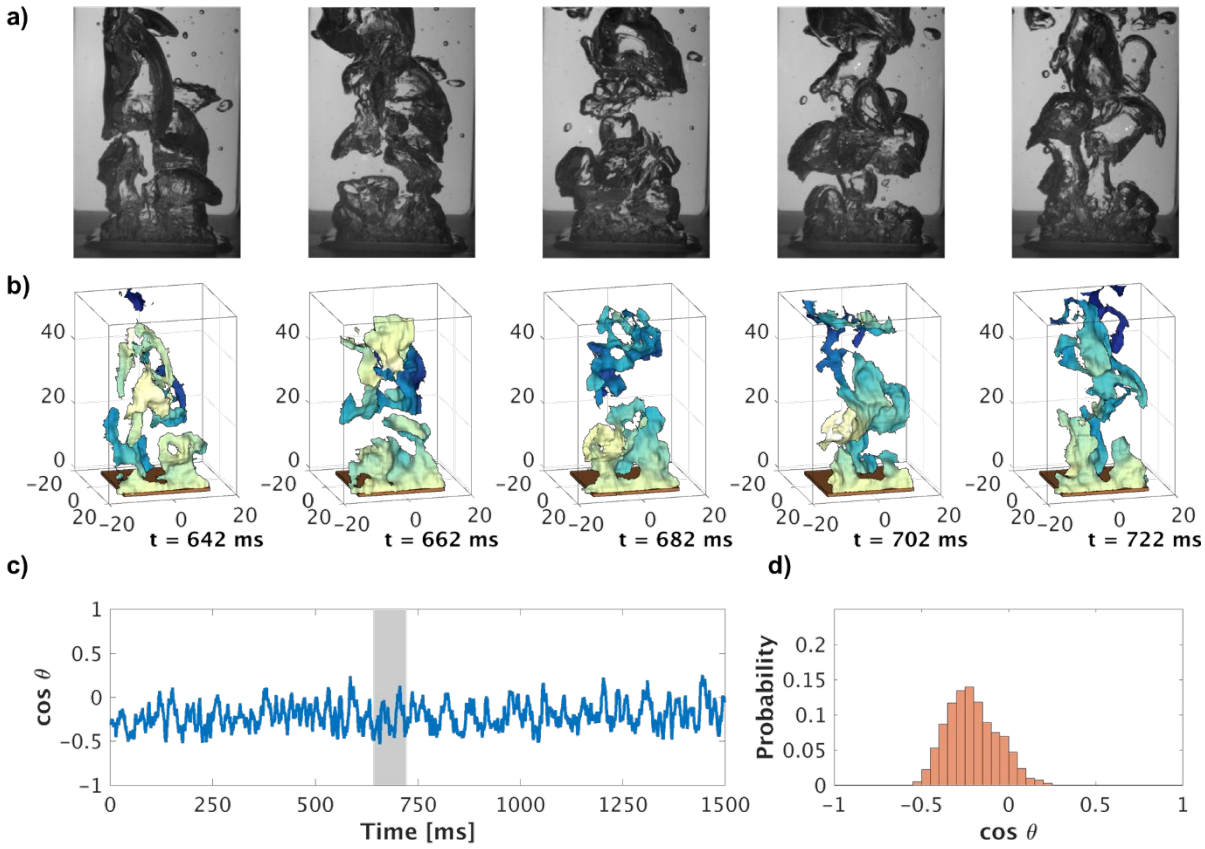

Figure 3.6. Sequence of (a) left grayscale images and (b) three-dimensional views of reconstructed liquid-vapor interface for a heat flux of 36 W/cm^2, as well as the (c) time signal and (d) probability density function for the cosine of the contact angle of the liquid vapor interface attached to the front edge of the heat source.

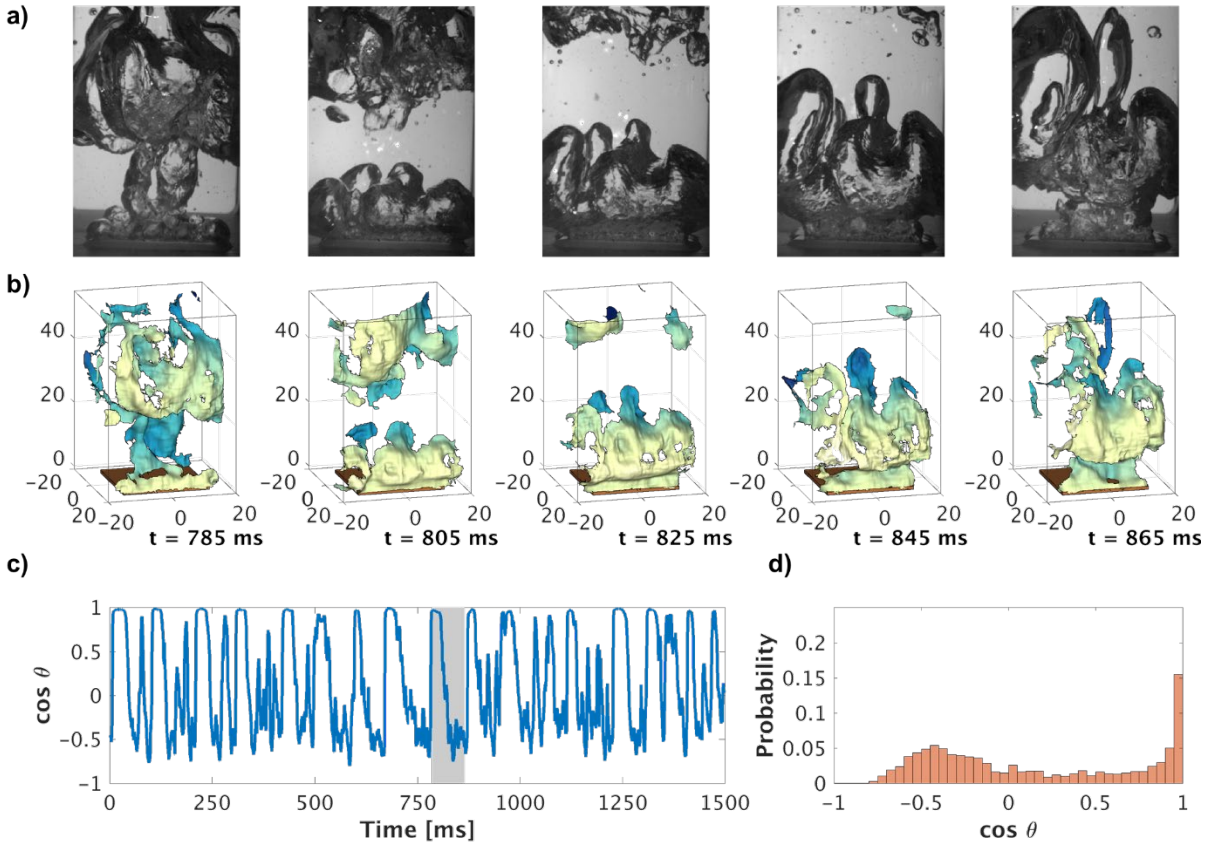

Figure 3.7. Sequence of (a) left grayscale images and (b) three-dimensional views of reconstructed liquid-vapor interface for a heat flux of 82 W/cm^2, as well as the (c) time signal and (d) probability density function for the cosine of the contact angle of the liquid vapor interface attached to the front edge of the heater.

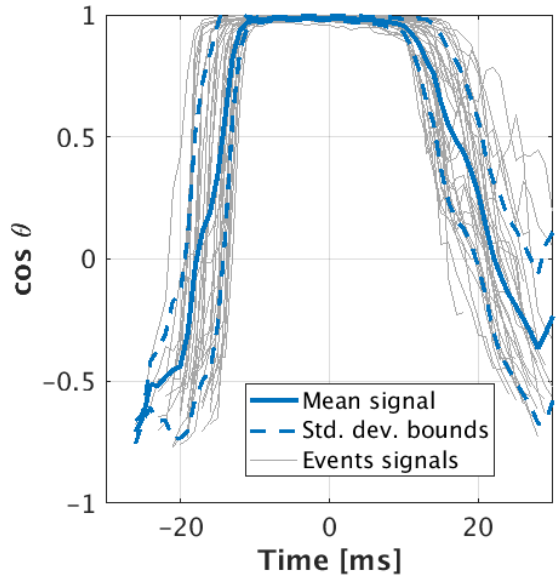

Figure 3.8. Cosine of contact angle signals for 33 similar vapor burst events aligned in time.

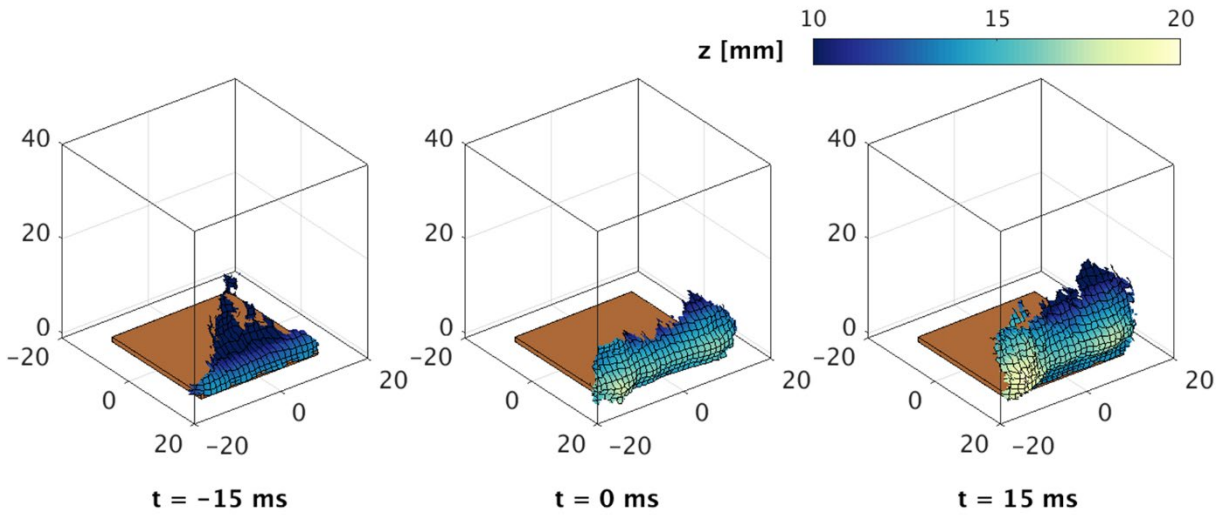

Figure 3.9. Evolution of the interface morphology for the characteristic vapor burst event.

4. VISUALIZING NEAR-WALL TWO-PHASE FLOW MORPHOLOGY DURING CONFINED AND SUBMERGED JET IMPINGEMENT BOILING TO THE POINT OF CRITICAL HEAT FLUX

During confined, submerged two-phase jet impingement of water at low orifice-to-target spacings, the formation of large vapor structures in the confinement gap has been observed for a wide range of surface heat fluxes [5]. The vapor structures remain in the confinement gap for long periods as compared with the characteristic times for formation and departure of large vapor bubbles during nucleate pool boiling. However, the heat transfer performance does not deteriorate, and the nucleate boiling regime is still significantly extended beyond the critical heat flux for pool boiling. This behavior is intriguing because it indicates that, for this configuration, the main effect of the jet is not to remove vapor from the confinement gap but to continuously rewet the surface by breaking through the vapor structure close to the heated surface. The current study investigates the connection between the flow morphology inside the confinement gap and the extension of the nucleate boiling regime during two-phase jet impingement of water at small orifice-to-target spacings. For characterization of the flow morphology, synchronized high-speed visualizations are performed from the top and the side of the confinement gap. During confined and submerged jet impingement, two-phase flow morphology characterization has been mainly limited to optical visualizations from the side of the confinement gap [4,5,42,71], but the formation of large vapor structures prevents examination of flow phenomena close to the surface in the side view. Visualization from the top of the confinement gap, as performed in this work, enables direct observation of boiling behavior on the heated surface, which is critical to unraveling the connection between flow morphology and the occurrence of critical heat flux. A version of the materials in this chapter have been submitted for publication.

4.1 Experimental Methods

4.1.1 Flow Loop

Figure 4.1a shows a diagram of the flow loop that is used to perform the experiments and is described in detail in Ref. [4]. The flow loop delivers degassed water to the test section at a controlled mass flow rate and temperature. Water is circulated through the loop by a

magnetically-coupled gear pump with adjustable rotational speed. The mass flow rate to the test section is measured by a Coriolis flow meter (CMFS015M, Emerson), and finely tuned by controlling the flow through a bypass loop with a metering valve. The power input to a preheater upstream of the test section is adjusted to set the inlet temperature. Water is drawn from and returns to a reservoir that is open to the ambient. The liquid in the reservoir is continuously boiled during testing to maintain a degassed state, and the reservoir is hence at the saturation temperature. The water is slightly cooled in a heat exchanger downstream of the reservoir to prevent cavitation in the pump.

4.1.2 Test Section

Figure 4.1b presents a schematic illustration of the test section, in which the plenum is modified from the original design in Ref. [4] to permit visualization of the flow from the top of the confinement gap. The walls of the test section are made of polyether ether ketone (PEEK), except for the front and back walls, which are made of polycarbonate to allow side-view optical access of the confinement gap. Liquid enters laterally at the top of the plenum through a radial flow distributor as shown in Figure 4.1c. The radial flow distributor attenuates the turbulence and asymmetry in the flow induced by the lateral fluid inlet and is additively manufactured using polyamide 12 (PA 12) [72]. Inside the radial flow distributor, a baffle diverts the liquid to flow circumferentially along an annular channel. From there, the liquid flows radially through slits in the inner wall of the annular channel and into the plenum. The liquid then flows downward in the straight section of the polycarbonate plenum of inner diameter 69.85 mm and length 113 mm, before entering a sharp-edged orifice at the bottom of the plenum to form an impinging liquid jet. The jet orifice has a diameter of 3.75 mm and a length of 6.35 mm. A T-type thermocouple is inserted through a port in the radial flow distributor and bent downward to measure the liquid temperature just upstream of where the jet is formed. A capillary tube is similarly inserted to probe the pressure upstream of the orifice. The pressure probe is connected to a differential pressure transducer (Omega PX409-015DWU5V-EH) to measure the difference in pressure upstream of the orifice and inside the chamber. The orifice plate, as well as the plate that seals the plenum on the top, are transparent and made of polycarbonate. The jet flows into a confinement gap of height 7.50 mm ($H/d = 2$) and diameter 76.20 mm.

The jet impinges on a smooth circular heated surface of 25.4 mm diameter that is gold-plated to prevent oxidation. The heated surface is the top of a copper block composed of two cylindrical sections. The lower section of the copper block has a larger diameter to accommodate twelve 100 W cartridge heaters. Along the top section of the copper block, rakes of T-type thermocouples (± 0.5 K) are positioned to provide the surface temperature by extrapolation, assuming a linear profile. The copper block is sealed flush to the bottom wall of the test section with a small bead of silicone sealant, and circumferentially insulated with ceramic fiber. A heat loss analysis is performed using a numerical model to estimate the actual heat flux into the fluid, as described in Ref. [9]. After impingement, the fluid flows beyond the confinement gap and leaves the chamber through an exit port on the top wall. The absolute pressure inside the chamber is monitored with a pressure tap (Gems 2200BG3F002A3UA) located at the bottom of the test section. The bath temperature is measured by a T-type thermocouple that is inserted through the side wall of the test section.

4.1.3 Experimental Procedure

Before running the two-phase jet impingement experiments, the flow loop and the test section are filled with water and a degassing procedure is initiated. During degassing, the fluid is circulated through the flow loop at 480 ml/min, and any solid contaminants larger than 7 μm are trapped in the particulate filter. Immersion heaters are used to vigorously boil the water in the reservoir, while the power to the preheater is adjusted to keep the temperature in the test section at ~80 °C. The vapor generated in the reservoir is condensed in two Graham reflux condensers located on the top of the reservoir, while non-condensable gases are vented. After degassing for 6 h, a priming procedure is performed on the heated surface to attenuate the effect of surface aging on the consistency of the boiling behavior [73]. The flow rate is increased to ~1100 ml/min, the particulate filter is bypassed, and the power input to the cartridge heaters inside the copper block is set to a relatively high value of around 700 W. After obtaining a steady response, the flow rate and inlet temperature are gently adjusted to the experimental conditions – a flow rate of 860 ml/min and an inlet temperature of 90 °C – and the surface is allowed to boil for an extended period to prime the surface. When consistent boiling behavior is achieved, the power to the heated surface is turned off and the experiment is started.

During the jet impingement experiments, power to the heated surface is increased in steps starting from 100 W until the critical heat flux is reached, as characterized by a dramatic rise in the surface temperature after a power increment. The power is kept constant at each increment until the system reaches a steady state. If necessary, the flow rate and inlet temperature are finely readjusted at each increment to maintain the nominal experimental conditions, namely, a Reynolds number of 15000 and an inlet subcooling of 10 °C. At steady state, temperature and flow data are acquired at 0.5 Hz and recorded for 2 min. During steady-state operation, synchronized high-speed videos of the flow in the confinement gap are acquired through the top of the plenum (Phantom Veo 710L) and the side of the test section (Phantom v1212) at 2000 fps each. A separate data acquisition system is used to record pressure drop data at high frequency; these measurements are also synchronized with the high-speed visualizations.

4.2 Results and Discussion

The boiling curve obtained during the jet impingement experiments is presented in Figure 4.2. The boiling curve includes all characteristics expected of the heat transfer modes that occur during jet impingement: single-phase heat transfer with a linear relationship between heat flux and wall superheat ($q'' < 35$ W/cm^2), partial boiling heat transfer as a transition mode, and fully boiling heat transfer with a weak non-linear dependence on the heat flux of the wall superheat ($q'' > 144$ W/cm^2). The boiling curve extends up to a heat flux of 255 W/cm^2, which is the last steady-state operating point that was tested before the next power increment induced critical heat flux. This maximum heat flux is ~2.3 times the value of critical heat flux predicted by Zuber's correlation [74] for pool boiling of 110 W/cm^2, which is commonly observed in experiments.

The morphology of vapor structures inside the confinement gap is controlled by the balance between vapor generation due to boiling at the heated surface and vapor condensation in the confinement gap due to the jet subcooling. The modified boiling number, $Bl^* = (\pi/4) D^2 q'' \big/ \dot{m} c_p \left(T_{sat} - T_j\right)$, introduced by Rau *et al.* [5], is a heat flux non-dimensionalization that is used to characterize the thermodynamic state of the fluid at the exit as either subcooled, $Bl^* < 1$, or saturated, $Bl^* \geq 1$. Relative to use of a vapor quality, the modified boiling number is more useful in describing the phenomena of interest that span across subcooled and saturated exit flow conditions. The flow morphologies observed during the jet impingement

experiments are classified according to the thermodynamic exit condition of the fluid, namely, as having subcooled or saturated exit flow conditions, and are described in detail in the following.

4.2.1 Flow Morphology during Subcooled Exit Flow Conditions

During subcooled exit flow conditions, the vapor generated due to boiling at the heater condenses inside the confinement gap, and the morphology of vapor structures inside the gap strongly depends on the heat flux, which controls the rate of vapor generation. Figure 4.3a and Figure 4.3b respectively present the top- and side-view observations of the flow morphology during these subcooled exit flow conditions. Figure 4.3c shows sketches of the flow morphology based on the visualizations.

At $Bl^* \sim 0.4$, nucleate boiling starts. Inside the fluid wall jet, nucleation and growth of tiny bubbles is observed, with a higher concentration at the periphery of the heated surface where the single-phase heat transfer coefficient is the lowest (Figure 4.3a). The tiny bubbles either condense inside the jet stream or are dragged to the edge of the heat source, and do not escape from the wall jet into the confinement gap. The bubbles coalesce as they are dragged to the periphery to form small vapor petals around the edge of the circular heated surface. Continuous vapor condensation prevents the petals from growing and departing the heated surface into the confinement gap as discrete vapor bubbles. A few air bubbles at the top of the confinement gap (underside of the orifice plate) slightly occlude the top view, despite extensive degassing.

Increases in heat flux intensify the vapor generation ($Bl^* \sim 0.62$), and the rim of petals is able to grow into bubbles that depart from the surface and condense inside the confinement gap. When $Bl^* \sim 0.78$, the vapor is generated fast enough that the petals grow into vapor blobs that partially bridge the confinement gap, without departing from the heated surface. The blobs merge into a single vapor structure. Then, the vapor structure collapses due to condensation and the blobs start forming again. The growing blobs are noticeable in the top view in Figure 4.3a. The bubble in the center of the image is an air bubble that is attached to the orifice plate. Two different images of the vapor flow morphology are included in the side-view observations in Figure 4.3b at $Bl^* \sim 0.78$ to illustrate the two key states, formation (state 1) and growth (state 2) of the vapor blobs. To represent the transient alternation between these states, they are respectively drawn in dark versus light gray in the flow morphology sketches in Figure 4.3c.

When the exit flow is close to saturation, $Bl^* = 0.94$, vapor generation is strong enough to form an unsteady, bowl-like axisymmetric vapor structure that bridges across the confinement gap and expands toward the outer edge of the orifice plate. In some instances, the bowl-like structure breaks into a vapor layer at the top of the confinement gap and a thick vapor rim attached to the heat source (Figure 4.3b, state 1). The bowl-like vapor structure is reformed as the vapor rims grows and reconnects with the top vapor layer (Figure 4.3b, state 2). In other instances, the bowl-like vapor structure extends beyond the edge of the orifice plate and some vapor escapes the confinement gap; afterward, the vapor structure either shrinks or breaks into two parts.

When the bowl-like vapor structure forms, the heated surface can be seen through the vapor in the top view, Figure 4.3a ($Bl^* = 0.94$). However, this view can be obstructed by liquid droplets that condense on the underside of the relatively colder orifice plate. The condensed droplets are swept away when the vapor structure breaks due to condensation, or when it shrinks due to vapor escaping from the gap, which enables unobstructed visualization of the boiling phenomena at the surface at some intervals. Although bubble nucleation occurs on the entire surface for $Bl^* = 0.94$, the density increases with the distance from the center of the heater, and nucleation sites are sparse in the vicinity of the impingement region under the orifice.

The dynamic behavior of the vapor structures in the confinement gap causes oscillations in the pressure drop between the inlet plenum and downstream of the confinement gap, with a magnitude that is linked to the vapor morphology. Figure 4.5 presents the relative standard deviation in pressure drop for the tested heat fluxes along with schematic illustrations of the observed vapor morphology inside the confinement gap. Slight oscillations occur during single-phase heat transfer and boiling at low heat fluxes ($Bl^* < 0.62$). When the vapor blobs grow large enough to form vapor bridges in the confinement gap, the amplitude of pressure oscillations increases due to partial obstruction of the jet flow. The amplitude of oscillations reaches a maximum when the exit flow is close to saturation ($Bl^* = 0.94$) and the vapor morphology is an unsteady bowl-like structure.

4.2.2 Flow Morphology during Saturated Exit Flow Conditions

Figure 4.4 presents the observed flow morphology during saturated exit flow conditions. When the boiling number is increased above unity, vapor escapes the confinement gap frequently

by breaking off when the bowl-like vapor structure reaches the edge of the orifice plate. The vapor structure alternates between a reestablishing vapor bowl, and an asymmetric shape skewed at the top towards one side of the orifice plate where the vapor breaks off. As seen in Figure 4.5, the amplitude of the oscillations in pressure decreases dramatically when the exit flow thermodynamic conditions become saturated, and vapor continuously bridges the confinement gap. From this point on, the amplitude of pressure oscillations increases almost monotonically with heat flux (Figure 4.5) because the vapor break-off events become more frequent and dramatic. At high heat fluxes, $Bl^* > 1.78$, as the vapor bowl is reestablished, the confinement gap can be completely covered with vapor, and the vapor break-off can be violent enough to almost clear all vapor from the gap.

Top view observations indicate that the liquid jet flows downward through the vapor structure and impinges on the surface. The heated surface is always visible through the orifice across the tested heat fluxes, which confirms that the jet is not diverted by the vapor before it impinges (see Figure 4.3a and Figure 4.4a). After impingement, the liquid jet transforms into a fluid wall jet, flowing radially outwards underneath the vapor structure. Boiling occurs within the fluid wall jet, exhibiting different flow regimes that depend on the heat flux. Under saturated exit flow conditions and up to a heat flux of ~175 W/cm^2, $1.0 > Bl^* > 1.44$, intense boiling occurs on the entire heated surface in a bubbly flow regime, as can be seen in the top view in Figure 4.4a, and is illustrated in the corresponding sketch of the flow morphology in Figure 4.4c. The vapor bubbles accumulate into the vapor structure and ultimately escape the confinement gap at the top, while the remaining liquid is expelled at the edge of the heated surface. This provides direct evidence that the impinging jet extends the nucleate boiling regime by a mechanism of continuously wetting the heated surface.

As the heat flux is increased further, the intense vapor generation at the surface significantly disrupts the flow of the fluid wall jet. As can be seen in Figure 4.4a, for the heat flux of 215 W/cm^2 and $Bl^* = 1.78$, the fluid wall jet flow becomes more chaotic with increasing radius, signaling a churn-like behavior. Also part of the fluid wall jet is sheared off the surface, and some liquid droplets break into the vapor structure. Close examination of the high-speed videos indicates that the sheared droplets travel inside the vapor structure to the liquid-vapor interface and merge with the liquid in the bath. The rest of the liquid flow remains attached to the surface, forming a liquid film that extends to the edge of the heater.

At the last steady-state operating point before critical heat flux, $q'' = 255$ W/cm^2 and $Bl^* = 2.11$, bubbly flow is almost absent in the wall jet in the top view visualizations. Churn-like flow dominates the fluid wall jet except in the impinging region, where discrete tiny bubbles can still be recognized. The splashing of the liquid film due to shearing is very strong, and the liquid-vapor interface is heavily disrupted. At this operating point very close to the critical heat flux, transient spikes are observed in the surface temperature signals, which suggest partial dryout of the heated surface. These flow morphology observations, particularly visualizations from the top of the confinement gap, indicate that critical heat flux occurs when a significant portion of the liquid in the wall jet is diverted away from the surface due to splashing and the remaining liquid film that flows attached to the heater surface dries out before reaching the edge.

4.3 Conclusion

Experiments are conducted with a single, confined and submerged water jet undergoing boiling after impinging on a circular heated surface to investigate the coupling between two-phase flow morphology and the extension of the nucleate boiling regime. The flow morphology is characterized across a range of heat fluxes that includes subcooled and saturated exit flow conditions, from incipience to critical heat flux. Under subcooled exit flow conditions, the morphology of vapor structures strongly depends on the heat flux, which controls the vapor generation rate. Frequent collapse of the vapor structures due to condensation induces strong oscillations in the pressure drop. When saturated exit flow conditions are reached at higher heat fluxes, a characteristic dynamic behavior of the vapor structure inside the confinement gap is established. The vapor agglomerates inside the gap into a bowl-like shape that continuously grows due to vapor generation and momentarily shrinks when vapor breaks off at the edge of the orifice plate.

First-of-their-kind flow visualizations from the top of the confinement gap allow us to conclude that the liquid jet flows downward through the vapor structure, impinges on the surface, and then flows underneath the vapor structure as a fluid wall jet; bubbles nucleate at the heated surface and grow inside this fluid wall jet. These observations confirm that continual surface rewetting is the mechanism by which the liquid jet extends the nucleate boiling regime beyond the critical heat flux limit encountered in pool boiling. At high heat fluxes, the fluid wall jet becomes more chaotic with increasing radius, indicating a transition from a bubbly to a churn-

like flow regime. Also, shearing of liquid droplets from the fluid wall jet into the bowl-like vapor structure is observed. At the highest heat flux before critical heat flux, a churn-like flow regime is dominant and significant shearing of liquid droplets occurs. These observations indicate that critical heat flux occurs because the intense vapor generation diverts a considerable portion of the liquid in the wall jet away from the heater, and the remaining portion that is able to wet the surface dries out before reaching the edge.

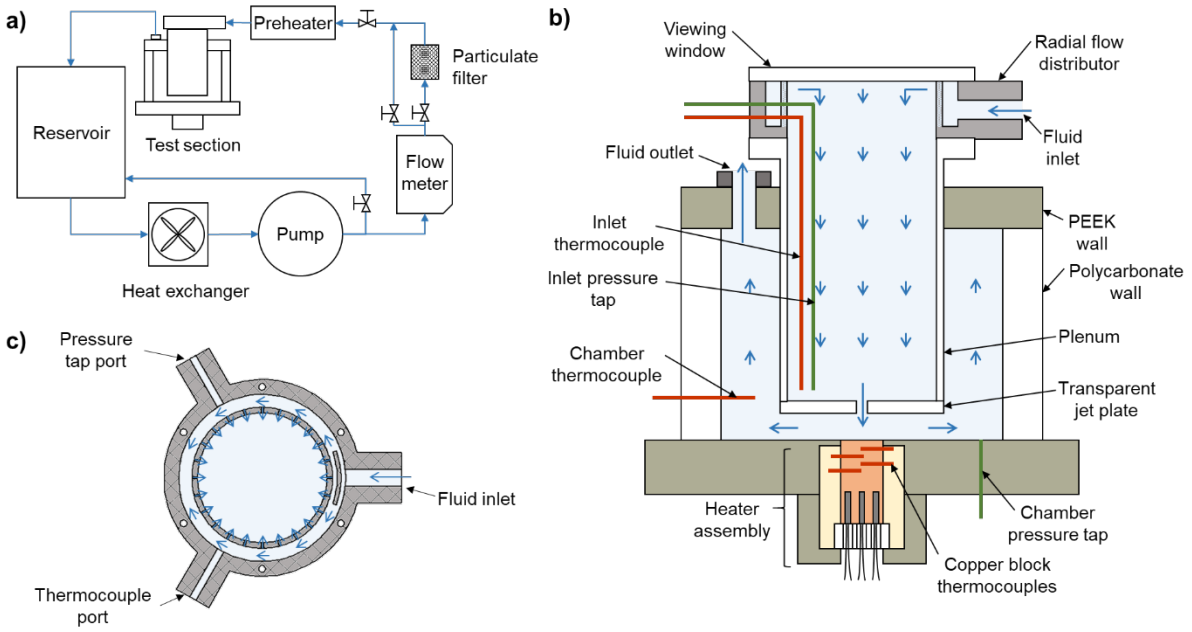

Figure 4.1. (a) Flow loop diagram, (b) schematic illustration of the test section, and (c) cross-sectional top view of the radial flow distributor.

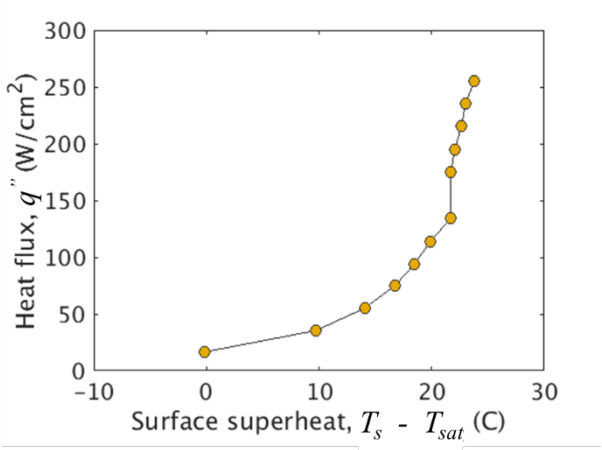

Figure 4.2. Boiling curve during two-phase jet impingement of a water jet on a circular heater (d = 3.75 mm, Re = 15000, H/d = 2, ΔT_{sub} = 10 K, p_{op} = 1 atm).

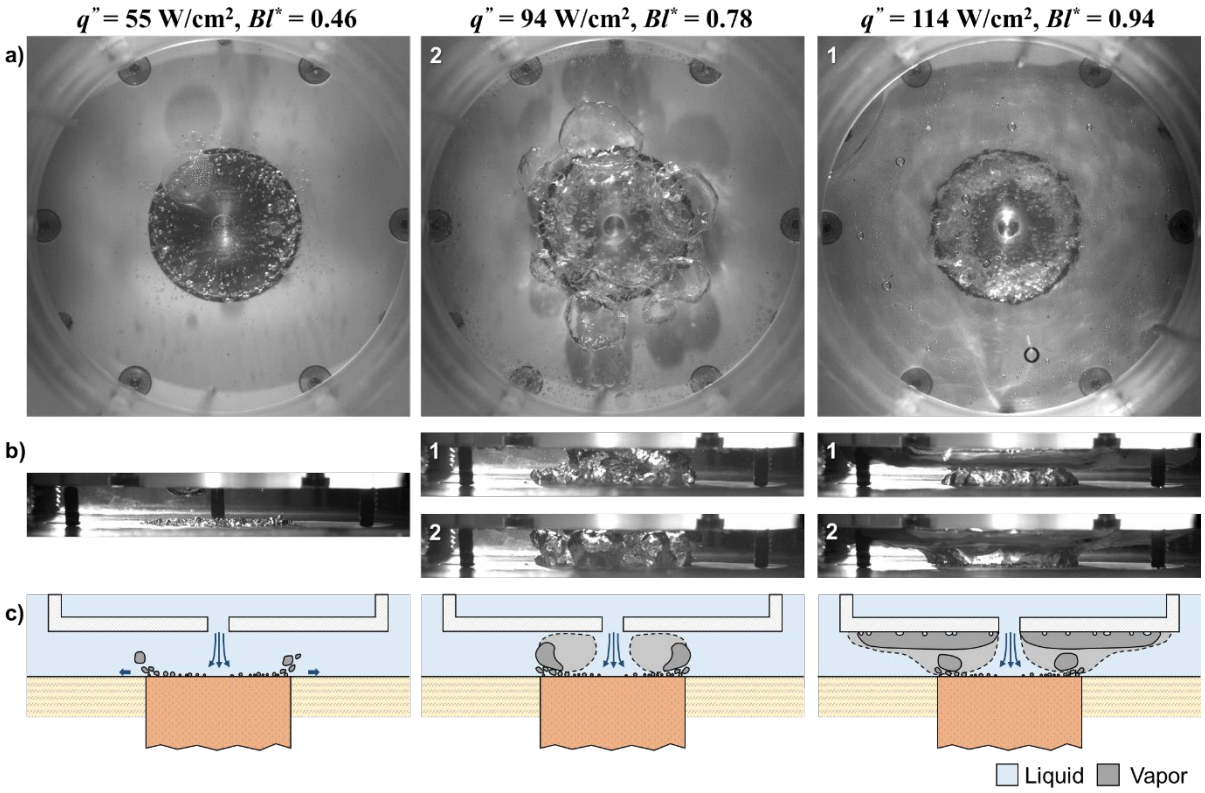

Figure 4.3. (a) Top-view and (b) side-view observations along with (c) sketches of the flow morphology during two-phase jet impingement under subcooled exit flow conditions. State 1 and state 2, as labelled in the side-view images, are respectively drawn in dark and light gray in the flow morphology sketches.

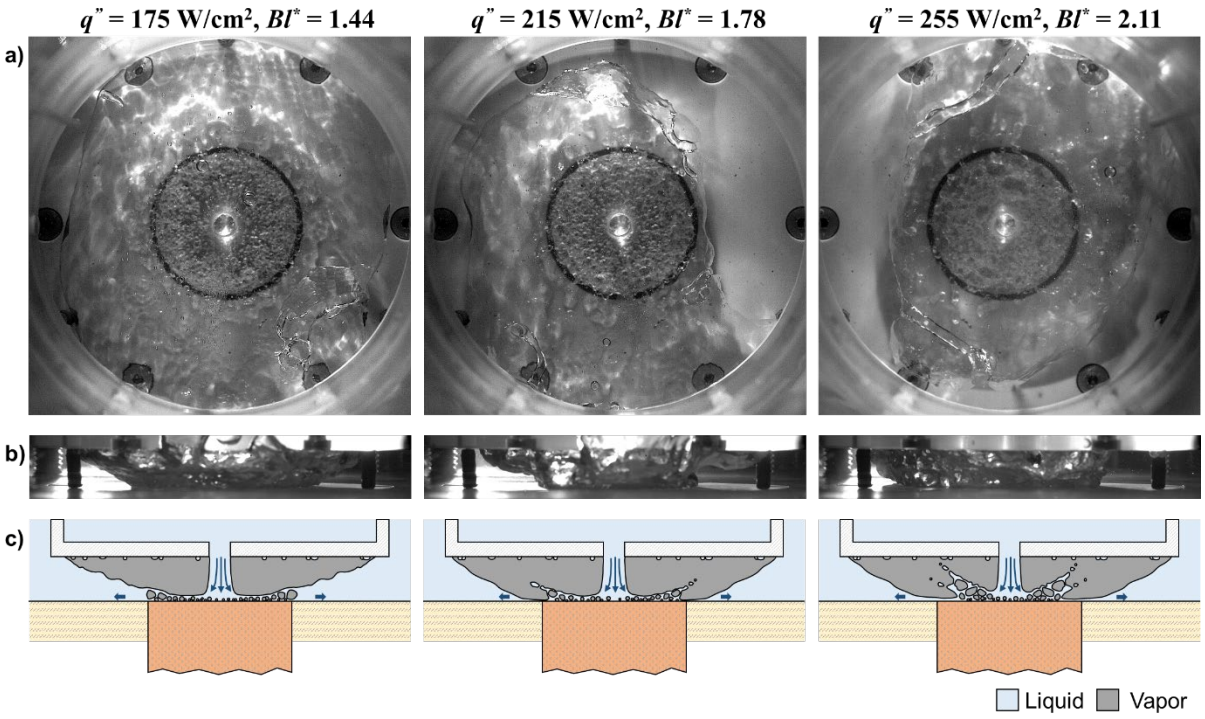

Figure 4.4. (a) Top-view and (b) side-view observations along with (c) sketches of the flow morphology during two-phase jet impingement under saturated exit flow conditions.

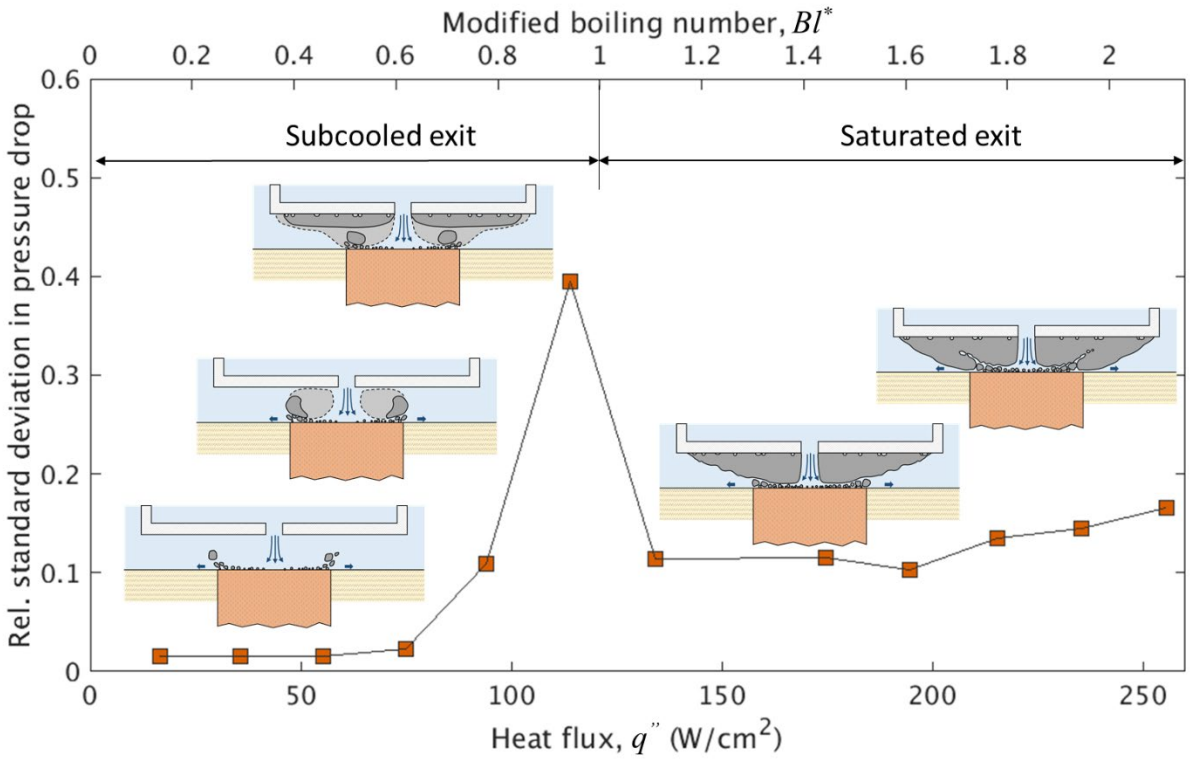

Figure 4.5. Relative standard deviation in pressure drop between the inlet plenum and downstream of the confinement gap as a function of heat flux. Sketches of flow morphology are included.

5. CONCLUSIONS AND FUTURE WORK

The goal of this dissertation was to characterize two-phase flow morphology evolution during nucleate boiling in two different configurations, namely, pool boiling and two-phase jet impingement. The flow morphology investigation aimed to establish the connection between flow and heat transfer phenomena and was performed via non-invasive, high-speed visualizations. Also, a reconstruction technique was developed that provides rich information regarding the location of the liquid-vapor interface from pairs of stereoscopic images. This chapter summarizes the conclusions from the dissertation and suggests avenues of future research.

5.1 Conclusions

In Chapter 3, a liquid-vapor interface reconstruction technique based on high-speed stereoscopic imaging was developed. The technique was applied to the case of pool boiling from a 27.2 mm × 27.2 mm square heated surface over a range of heat fluxes from 36 W/cm^2 to 92 W/cm^2.

- The liquid-vapor interface reconstruction technique produces very good results for regions where the interface is highly textured and the texture is captured with adequate contrast in the images. Interfaces in the vicinity of the heated surface are particularly suited for reconstruction because flow and boiling phenomena cause the interface to be textured. Inadequate contrast near the center of large vapor bubbles and in regions where the illumination is poor induces errors in the reconstructions. The locations of small and smooth vapor bubbles can be inferred from the reconstruction results but their shape is not adequately recovered.
- In the pool boiling experiment, two vapor release modes are clearly identifiable in temporal signals extracted from the reconstruction results: plume-like vapor flow and vapor burst release. During plume-like vapor flow, the behavior of vapor structures above the heated surface is dominated by buoyancy forces, and medium size bubbles form and rise frequently in groups. During the vapor burst release mode, large mushroom-like

vapor structures form and hover above the heated surface before departing with a strong trail that strips most of the vapor from the surface.

- The vapor burst events display a characteristic signature in the temporal signals, which implies that the interface undergoes similar morphological evolution during these events. Analysis of the reconstructed interfaces for a set of vapor burst events shows that a characteristic morphology exists during a vapor burst that is associated with the square shape of the heated surface.

In Chapter 4, a two-phase jet impingement experiment was performed to investigate the connection between flow morphology and the extension of the nucleate boiling regime. The case of a single, confined, submerged water jet (d = 3.75 mm) that impinges on a circular heated surface (D = 25.4 mm) at an orifice-to-target (H/d) of 2, Reynolds number (Re) of 15000 and inlet subcooling (ΔT_{sub}) of 10 K was considered. The range of heat fluxes that were analyzed extended from incipience of nucleate boiling until close to critical heat flux, including subcooled and saturated exit conditions. Synchronized visualization from the side and top of the confinement gap allowed study the evolution of vapor structures inside the gap and two-phase flow phenomena close to the heated surface.

- Under subcooled exit flow conditions, vapor structures frequently form and collapse inside the confinement gap, inducing oscillations in the pressure drop across the jet orifice. When the exit flow conditions are close to saturation, the magnitude of the pressure oscillations reaches a maximum and an unsteady bowl-like structure is observed inside the confinement gap.
- Under saturated exit flow conditions, vapor continuously bridges the confinement gap and a characteristic dynamic behavior of the bowl-like vapor structures is established. The magnitude of pressure oscillations drastically reduces when saturated exit flow conditions are reached; afterwards, the amplitude of pressure oscillations increases almost monotonically with heat flux.
- Examination of the top view visualizations shows that the jet flows through the vapor structure in the confinement gap and impinges on the heated surface. After impingement, the jet transforms into a wall jet that undergoes phase change due to nucleate boiling at

the surface. Continuous surface wetting is confirmed as the mechanism by which the nucleate boiling regime is extended.

- At high heat fluxes, a transition with increasing radius in the flow regime of the wall jet is observed from bubbly to churn-like flow. Intense vapor generation at the heated surface causes shearing of liquid droplets from the wall jet into the bowl-like vapor structure. Critical heat flux appears to occur when a significant portion of the liquid in the wall jet is diverted from the heated surface, and the portion that is able to wet the surface dries out before reaching the edge.

5.2 Suggested Future Work

Possible future research directions are presented in this section. The proposed studies aim to improve the understanding of flow phenomena during nucleate boiling, and better harness the advantages of the liquid-vapor interface reconstruction technique.

1. Although the nucleate pool boiling case to which the liquid reconstruction technique was applied (Chapter 3) is very relevant for cooling applications, the geometry of the liquid-vapor interface and the involved two-phase phenomena are complex, which hinders a direct comparison with numerical models. The liquid-vapor reconstruction technique can be applied to a film boiling situation, which is more approachable for analytical and numerical model. Reconstruction results can provide data to validate predictions on the liquid-vapor interface geometry and interfacial transport, which have been identified as crucial aspects in numerical modeling of two-phase flows.
2. A characteristic morphology of vapor structures above a square heated surface during vapor burst events was identified in Chapter 3. However, the connection between the vapor structure morphology and the hovering time was not analyzed. A force balance approach could be used to estimate the hovering time of the vapor structures, which can be compared with the experimental values. Also, the validity of the spherical shape assumption that is used in some critical flux models can be assessed.
3. The lobed-shape of vapor structures during vapor burst events was associated to the square shape of the heater used in Chapter 3. This observation can be verified by characterizing the morphology of the vapor structures above heated surfaces of different

shape but equal area. The comparison could provide insight into heat source designs that favor the release of the vapor structures and thereby enhance the critical heat flux.

4. The flow morphology characterization during confined and submerged jet impingement presented in Chapter 4 was restricted to a single set of experimental parameters. An exploration of the experimental parameters should be performed to established how the observed flow morphologies are mapped with Reynolds number, modified boiling number and non-dimensional geometric parameters. The dominant flow phenomena that affect the heat transfer performance can depend on the particular combination of non-dimensional parameters; in addition, other mechanisms that were not observed during the study may play an important role at different conditions.
5. The conclusions on the flow morphology during jet impingement were mainly drawn from qualitative observations. Image processing techniques can be applied to determine parameters associated with the flow boiling phenomena, such as: distribution of nucleation site density, nucleation frequency and velocity of vapor bubbles that are dragged in the jet stream. Additionally, stereoscopic reconstruction techniques can be used to determine the angle and velocity at which liquid droplets are sheared off the fluid wall jet. The quantitative characterization can be used to validate and develop heat transfer models.

REFERENCES

[1] Y. Iida and K. Kobayasi, "Distributions of void fraction above a horizontal heating surface in pool boiling," *Bull. JSME*, vol. 12, no. 50, pp. 283–290, 1969.

[2] J. L. Kickhofel, R. Zboray, M. Damsohn, A. Kaestner, E. H. Lehmann, and H. M. Prasser, "Cold neutron tomography of annular coolant flow in a double subchannel model of a boiling water reactor," *Nucl. Instruments Methods Phys. Res. Sect. A Accel. Spectrometers, Detect. Assoc. Equip.*, vol. 651, no. 1, pp. 297–304, 2011.

[3] S. Meissner, J. Herold, L. Kirsten, C. Schneider, and E. Koch, "3D optical coherence tomography as new tool for microscopic investigations of nucleate boiling on heated surfaces," *Int. J. Heat Mass Transf.*, vol. 55, no. 21–22, pp. 5565–5569, 2012.

[4] M. J. Rau, T. Guo, P. P. Vlachos, and S. V. Garimella, "Stereo-PIV measurements of vapor-induced flow modifications in confined jet impingement boiling," *Int. J. Multiph. Flow*, vol. 84, pp. 19–33, 2016.

[5] M. J. Rau, P. P. Vlachos, and S. V. Garimella, "A tomographic-PIV investigation of vapor-induced flow structures in confined jet impingement boiling," *Int. J. Multiph. Flow*, vol. 84, pp. 86–97, 2016.

[6] Y. Haramura and Y. Katto, "A new hydrodynamic model of critical heat flux, applicable widely to both pool and forced convection boiling on submerged bodies in saturated liquids," *Int. J. Heat Mass Transf.*, vol. 26, no. 3, pp. 389–399, 1983.

[7] T. Kumada and H. Sakashita, "Pool boiling heat transfer-II. Thickness of liquid macrolayer formed beneath vapor masses," *Int. J. Heat Mass Transf.*, vol. 38, no. 6, pp. 979–987, 1995.

[8] T. Kumada, H. Sakashita, and H. Yamagishi, "Pool boiling heat transfer-I. Measurement and semi-empirical relations of detachment frequencies of coalesced bubbles," *Int. J. Heat Mass Transf.*, vol. 38, no. 6, pp. 969–977, 1995.

[9] M. J. Rau and S. V. Garimella, "Confined jet impingement with boiling on a variety of enhanced surfaces," *J. Heat Transfer*, vol. 136, no. 10, p. 101503, 2014.

[10] D. H. Wolf, F. P. Incropera, and R. Viskanta, "Jet impingement boiling," *Adv. Heat Transf.*, vol. 23, pp. 1–132, 1993.

[11] L. Qiu, S. Dubey, F. H. Choo, and F. Duan, “Recent developments of jet impingement nucleate boiling,” *Int. J. Heat Mass Transf.*, vol. 89, pp. 42–58, 2015.

[12] F. Bellocchio, N. A. Borghese, S. Ferrari, V. Piuri, and S. Reconstruction, *3D Surface Reconstruction*. New York, NY: Springer New York, 2013.

[13] Y. Liu, X. Yang, Q. Zhu, P. Ju, M. Ishii, and J. R. Buchanan, “Development of the droplet-capable conductivity probe for measurement of liquid-dispersed two-phase flow,” *Int. J. Multiph. Flow*, vol. 88, pp. 238–250, 2017.

[14] F. Murzyn, D. Mouaze, and J. R. Chaplin, “Optical fibre probe measurements of bubbly flow in hydraulic jumps,” *Int. J. Multiph. Flow*, vol. 31, no. 1, pp. 141–154, 2005.

[15] B. Farrar, A. L. Samways, J. Ali, and H. H. Bruun, “A computer-based hot-film technique for two- phase flow measurements,” *Meas. Sci. Technol.*, vol. 6, pp. 1528–1537, 1995.

[16] S. Kim, X. Y. Fu, X. Wang, and M. Ishii, “Development of the miniaturized four-sensor conductivity probe and the signal processing scheme,” *Int. J. Heat Mass Transf.*, vol. 43, no. 22, pp. 4101–4118, 2000.

[17] H. M. Prasser, M. Misawa, and I. Tiseanu, “Comparison between wire-mesh sensor and ultra-fast X-ray tomograph for an air-water flow in a vertical pipe,” *Flow Meas. Instrum.*, vol. 16, no. 2–3, pp. 73–83, 2005.

[18] M. J. Da Silva ., S. Thiele, L. Abdulkareem, B. J. Azzopardi, and U. Hampel, “High-resolution gas-oil two-phase flow visualization with a capacitance wire-mesh sensor,” *Flow Meas. Instrum.*, vol. 21, no. 3, pp. 191–197, 2010.

[19] C. Boyer, A. M. Duquenne, and G. Wild, “Measuring techniques in gas-liquid and gas-liquid-solid reactors,” *Chem. Eng. Sci.*, vol. 57, no. 16, pp. 3185–3215, 2002.

[20] A. Kastengren and C. F. Powell, “Synchrotron X-ray techniques for fluid dynamics,” *Exp. Fluids*, vol. 55, no. 3, 2014.

[21] Y. Fu and Y. Liu, “Experimental study of bubbly flow using image processing techniques,” *Nucl. Eng. Des.*, vol. 310, pp. 570–579, 2016.

[22] M. Honkanen, P. Saarenrinne, T. Stoor, and J. Niinimäki, “Recognition of highly overlapping ellipse-like bubble images,” *Meas. Sci. Technol.*, vol. 16, no. 9, pp. 1760–1770, 2005.

[23] W. Cheng, Y. Murai, T. Sasaki, and F. Yamamoto, “Bubble velocity measurement with a recursive cross correlation PIV technique,” *Flow Meas. Instrum.*, vol. 16, no. 1, pp. 35–46, 2005.

[24] F. Ravelet, C. Colin, and F. Risso, “On the dynamics and breakup of a bubble rising in a turbulent flow,” *Phys. Fluids*, vol. 23, no. 10, 2011.

[25] A. Tokuhiro, M. Maekawa, K. Iizuka, K. Hishida, and M. Maeda, “Turbulent flow past a bubble and an ellipsoid using shadow-image and PIV techniques,” *Int. J. Multiph. Flow*, vol. 24, no. 8, pp. 1383–1406, 1998.

[26] M. J. Sathe, I. H. Thaker, T. E. Strand, and J. B. Joshi, “Advanced PIV/LIF and shadowgraphy system to visualize flow structure in two-phase bubbly flows,” *Chem. Eng. Sci.*, vol. 65, no. 8, pp. 2431–2442, 2010.

[27] M. J. Sathe, C. S. Mathpati, S. S. Deshpande, Z. Khan, K. Ekambara, and J. B. Joshi, “Investigation of flow structures and transport phenomena in bubble columns using particle image velocimetry and miniature pressure sensors,” *Chem. Eng. Sci.*, vol. 66, no. 14, pp. 3087–3107, 2011.

[28] M. Sathe, J. Joshi, and G. Evans, “Characterization of turbulence in rectangular bubble column,” *Chem. Eng. Sci.*, vol. 100, pp. 52–68, 2013.

[29] Z. Liu, Y. Zheng, L. Jia, and Q. Zhang, “Study of bubble induced flow structure using PIV,” *Chem. Eng. Sci.*, vol. 60, pp. 3537–3552, 2005.

[30] X. Zhou, B. Doup, and X. Sun, “Measurements of liquid-phase turbulence in gas–liquid two-phase flows using particle image velocimetry,” *Meas. Sci. Technol.*, vol. 24, no. 12, p. 125303, 2013.

[31] Y. A. Hassan, J. Ortiz-Villafuerte, and W. D. Schmidl, “Three-dimensional measurements of single bubble dynamics in a small diameter pipe using stereoscopic particle image velocimetry,” *Int. J. Multiph. Flow*, vol. 27, pp. 817–842, 2001.

[32] D. Adhikari and E. K. Longmire, “Visual hull method for tomographic PIV measurement of flow around moving objects,” *Exp. Fluids*, vol. 53, no. 4, pp. 943–964, 2012.

[33] S. Im, Y. J. Jeon, and H. J. Sung, “Tomo-PIV measurement of flow around an arbitrarily moving body with surface reconstruction,” *Exp. Fluids*, vol. 56, no. 2, pp. 1–16, 2015.

[34] C. F. Ma, Y. P. Gan, and D. H. Lei, “Liquid jet impingement heat transfer with or without boiling,” *J. Therm. Sci.*, vol. 2, no. 1, pp. 32–49, 1993.

[35] I. Mudawar, “Assessment of high-heat-flux thermal management schemes,” *IEEE Trans. Components Packag. Technol.*, vol. 24, no. 2, pp. 122–141, 2001.

[36] M. J. Rau, E. M. Dede, and S. V. Garimella, “Local single- and two-phase heat transfer from an impinging cross-shaped jet,” *Int. J. Heat Mass Transf.*, vol. 79, pp. 432–436, 2014.

[37] D. T. Vader, F. P. Incropera, and R. Viskanta, “Convective nucleate boiling on a heated surface cooled by an impinging, planar jet of water,” *J. Heat Transfer*, vol. 114, no. 1, pp. 152–160, 1992.

[38] D. H. Wolf, F. P. Incropera, and R. Viskanta, “Local jet impingement boiling heat transfer,” *Int. J. Heat Mass Transf.*, vol. 39, no. 7, pp. 1395–1406, 1996.

[39] N. M. Dukle and D. K. Hollingsworth, “Liquid crystal images of the transition from jet impingement convection to nucleate boiling part II: Nonmonotonic distribution of the convection coefficient,” *Exp. Therm. Fluid Sci.*, vol. 12, no. 3, pp. 288–297, Apr. 1996.

[40] Y. Katto and M. Kunihiro, “Study of the mechanism of burn-out in boiling system of high burn-out heat flux,” *Bull. JSME*, vol. 16, no. 99, pp. 1357–1366, 1973.

[41] C. F. Ma and A. E. Bergles, “Boiling jet impingement cooling of simulated microelectronic chips,” *Heat Transf. Electron. Equip.*, vol. 1, pp. 5–12, 1983.

[42] M. D. Clark, J. A. Weibel, and S. V. Garimella, “Identification of nucleate boiling as the dominant heat transfer mechanism during confined two-phase jet impingement,” *Int. J. Heat Mass Transf.*, vol. 128, pp. 1095–1101, 2019.

[43] C. Mira-Hernández, M. D. Clark, J. A. Weibel, and S. V. Garimella, “Development and validation of a semi-empirical model for two-phase heat transfer from arrays of impinging jets,” *Int. J. Heat Mass Transf.*, vol. 124, pp. 782–793, 2018.

[44] I. Mudawar and D. C. Wadsworth, “Critical heat flux from a simulated chip to a confined rectangular impinging jet of dielectric liquid,” *Int. J. Heat Mass Transf.*, vol. 34, no. 6, pp. 1465–1479, 1991.

[45] R. Cardenas and V. Narayanan, “Heat transfer characteristics of submerged jet impingement boiling of saturated FC-72,” *Int. J. Heat Mass Transf.*, vol. 55, no. 15–16, pp. 4217–4231, 2012.

[46] J. H. Lienhard and R. Eichhorn, “On predicting boiling burnout for heaters cooled by liquid jets,” *Int. J. Heat Mass Transf.*, vol. 22, no. 5, pp. 774–776, 1979.

[47] M. Monde, “Critical heat flux in saturated forced convective boiling on a heated disk with and impinging jet,” *Wärme - und Stoffübertragung*, vol. 19, pp. 205–209, 1985.

[48] M. Monde and T. Inoue, “Critical heat flux in saturated forced convective boiling on a heated disk with multiple impinging jets,” *J. Heat Transfer*, vol. 113, no. 3, p. 722, 1991.

[49] M. Kandula, “Mechanisms and predictions of burnout in flow boiling over heated surfaces with an impinging jet,” *Int. J. Heat Mass Transf.*, vol. 33, no. 9, pp. 1795–1803, 1990.

[50] Y. Katto and M. Shimizu, “Upper limit of CHF in the saturated forced convection boiling on a heated disk with a small impinging jet,” *J. Heat Transfer*, vol. 101, no. 2, p. 265, 1979.

[51] J. P. Mchale and S. V. Garimella, “Nucleate boiling from smooth and rough surfaces – Part 2 : Analysis of surface roughness effects on nucleate boiling,” *Exp. Therm. Fluid Sci.*, vol. 44, pp. 439–455, 2013.

[52] J. W. Westwater and J. G. Santangelo, “Photographic Study of Boiling,” *Ind. Eng. Chem.*, vol. 47, no. 8, pp. 1605–1610, 1955.

[53] R. F. Gaertner, “Photographic Study of Nucleate Pool Boiling on a Horizontal Surface,” *J. Heat Transfer*, vol. 87, p. 17, 1965.

[54] A. M. Bhat, J. S. Saini, and R. Prakash, “Role of macrolayer evaporation in pool boiling at high heat flux,” *Int. J. Heat Mass Transf.*, vol. 29, no. 12, pp. 1953–1961, 1986.

[55] T. P. Allred, J. A. Weibel, and S. V. Garimella, “Enabling Highly Effective Boiling from Superhydrophobic Surfaces,” *Phys. Rev. Lett.*, vol. 120, p. 174501, 2018.

[56] L. H. Quam, “Hierarchical warp stereo,” *Readings in computer vision*. pp. 80–86, 1984.

[57] R. Tsai, “A versatile camera calibration technique for high accuracy 3D machine vision metrology using off-the-shelf TV cameras and lenses,” *IEEE J. Robot. Autom.*, vol. 3, no. 4, p. 32344, 1987.

[58] K. Levenberg, “A method for the solution of certain non-linear problems in least squares,” *Q. Appl. Math.*, vol. 2, no. 2, pp. 164–168, 1944.

[59] D. W. Marquardt, “An algorithm for least-squares estimation of nonlinear parameters,” *J. Soc. Ind. Appl. Math.*, vol. 11, no. 2, pp. 431–441, 1963.

[60] B. Wieneke, “Stereo-PIV using self-calibration on particle images,” *Exp. Fluids*, vol. 39, no. 2, pp. 267–280, 2005.

[61] “MATLAB.” The Mathworks, Inc., Natick, Massachusetts, 2016.

[62] E. Trucco and A. Verri, *Introductory Techniques for 3-D Computer Vision*. Upper Saddle River, New Jersey: Prentice Hall, 1998.

[63] D. V. Papadimitriou and T. J. Dennis, "Epipolar line estimation and rectification for stereo image pairs," *IEEE Trans. Image Process.*, vol. 5, no. 4, pp. 672–676, 1996.

[64] D. G. Lowe, "Distinctive image features from scale-invariant keypoints," *Int. J. Comput. Vis.*, vol. 60, no. 2, pp. 91–110, 2004.

[65] D. S. Szeliski, "A Taxonomy and Evaluation of Dense Two-Frame Stereo Correspondence Algorithms," *Int. J. Comput. Vis.*, vol. 47, no. 1–Mar, pp. 7–42, 2002.

[66] A. Vedaldi, "An implementation of SIFT detector and descriptor," *Int. J.*, vol. 1, pp. 1–7, 2008.

[67] E. Tola, V. Lepetit, P. Fua, and S. Member, "DAISY: An efficient dense descriptor applied to wide-baseline stereo.pdf," *IEEE Trans. Pattern Anal. Mach. Intell.*, vol. 32, no. 5, pp. 815–830, 2010.

[68] L. Alvarez, J. Weickert, and J. Sánchez, "Reliable estimation of dense optical flow fields with large displacements," *Int. J. Comput. Vis.*, vol. 39, no. 1, pp. 41–56, 2000.

[69] J. G. Santiago, S. T. Wereley, C. D. Meinhart, D. J. Beebe, and R. J. Adrian, "A particle image velocimetry system for microfluidics," *Exp. Fluids*, vol. 25, no. 4, pp. 316–319, 1998.

[70] C. Willert, "Adaptive PIV processing based on ensemble correlation," in *14Th International Symposium on Applications of Laser Techniques to Fluid Mechanics*, 2008.

[71] C. H. Shin, K. M. Kim, S. H. Lim, and H. H. Cho, "Influences of nozzle-plate spacing on boiling heat transfer of confined planar dielectric liquid impinging jet," *Int. J. Heat Mass Transf.*, vol. 52, no. 23–24, pp. 5293–5301, 2009.

[72] HP Development Company, "HP 3D High Reusability PA 12," Palo Alto, CA, 2017.

[73] S. M. You, A. Bar-Cohen, and T. W. Simon, "Boiling incipience and nucleate boiling heat transfer of highly wetting dielectric fluids from electronic materials," *IEEE Trans. Components, Hybrids, Manuf. Technol.*, vol. 13, no. 4, pp. 1032–1039, 1990.

[74] N. Zuber, "On the stability of boiling heat transfer," *Trans. ASME*, vol. 80, 1958.

[75] M. J. Rau and S. V. Garimella, "Local two-phase heat transfer from arrays of confined and submerged impinging jets," *Int. J. Heat Mass Transf.*, vol. 67, pp. 487–498, 2013.

[76] C. T. Chang, G. Kojasoy, F. Landis, and S. Downing, “Confined single- and multiple-jet impingement heat transfer-I. Turbulent submerged liquid jets,” *Int. J. Heat Mass Transf.*, vol. 38, no. 5, pp. 833–842, Mar. 1995.

[77] S. V. Garimella and R. A. Rice, “Confined and submerged liquid jet impingement heat transfer,” *J. Heat Transfer*, vol. 117, no. 4, pp. 871–877, 1995.

[78] 3M, “3M Novec Engineered Fluid HFE-7100 for Heat Transfer,” St. Paul, MN, 2002.

[79] C. T. Chang, G. Kojasoy, F. Landis, and S. Downing, “Confined single- and multiple-jet impingement heat transfer-II. Turbulent two-phase flow,” *Int. J. Heat Mass Transf.*, vol. 38, no. 5, pp. 843–851, Mar. 1995.

[80] R. A. Buchanan and T. A. Shedd, “Extensive Parametric Study of Heat Transfer to Arrays of Oblique Impinging Jets With Phase Change,” *J. Heat Transfer*, vol. 135, no. 11, p. 111017, 2013.

[81] E. A. Browne, G. J. Michna, M. K. Jensen, and Y. Peles, “Microjet array single-phase and flow boiling heat transfer with R134a,” *Int. J. Heat Mass Transf.*, vol. 53, no. 23–24, pp. 5027–5034, Nov. 2010.

[82] E. A. Browne, M. K. Jensen, and Y. Peles, “Microjet array flow boiling with R134a and the effect of dissolved nitrogen,” *Int. J. Heat Mass Transf.*, vol. 55, no. 4, pp. 825–833, 2012.

[83] D. Copeland, “Single-phase and boiling cooling of a small hear source by multiple nozzle jet impingement,” *ASME*, vol. 1, 1992.

[84] C. de Brún, R. Jenkins, T. L. Lupton, R. Lupoi, R. Kempers, and A. J. Robinson, “Confined jet array impingement boiling,” *Exp. Therm. Fluid Sci.*, vol. 86, pp. 224–234, 2017.

[85] F. J. Hong, C. Y. Zhang, W. He, P. Cheng, and G. Chen, “Confined jet array impingement boiling of subcooled aqueous ethylene glycol solution,” *Int. Commun. Heat Mass Transf.*, vol. 56, pp. 165–173, 2014.

[86] S. N. Joshi, M. J. Rau, and E. M. Dede, “An experimental study of a single-device jet impingement cooler with phase change using HFE-7100,” in *ASME 2013 International Mechanical Engineering Congress and Exposition IMECE 2013*, 2013, pp. 1–10.

[87] M. Monde and Y. Mitsutake, “Critical heat flux in forced convective subcooled boiling with multiple impinging jets,” *J. Heat Transfer*, vol. 117, pp. 241–243, 1996.

[88] E. N. Wang, L. Zhang, L. Jiang, J. M. Koo, J. G. Maveety, E. A. Sanchez, K. E. Goodson, and T. W. Kenny, "Micromachined jets for liquid impingement cooling of VLSI chips," *J. Microelectromechanical Syst.*, vol. 13, no. 5, pp. 833–842, 2004.

[89] B. M. Werneke, "Microjet array impingement heat transfer crossflow effects in single-phase and flow boiling," Rensselaer Polytechnic Institute, 2015.

[90] S. J. Wu, C. H. Shin, K. M. Kim, and H. H. Cho, "Single-phase convection and boiling heat transfer: Confined single and array-circular impinging jets," *Int. J. Multiph. Flow*, vol. 33, no. 12, pp. 1271–1283, 2007.

[91] M. T. Meyer, I. Mudawar, C. E. Boyack, and C. A. Hale, "Single-phase and two-phase cooling with an array of rectangular jets," *Int. J. Heat Mass Transf.*, vol. 49, no. 1–2, pp. 17–29, 2006.

[92] H. Martin, "Heat and mass transfer between impinging gas jets and solid surfaces," *Adv. Heat Transf.*, vol. 13, pp. 1–60, 1977.

[93] C. Li and S. V. Garimella, "Prandtl-number efects and generalized correlations for confinned and submerged jet impingement," *Heat Mass Transf.*, vol. 44, pp. 3471–3480, 2001.

[94] K. Stephan and M. Abdelsalam, "Heat-transfer correlations for natural convection boiling," *Int. J. Heat Mass Transf.*, vol. 23, no. 1, pp. 73–87, 1980.

[95] M. G. Cooper, "Heat flow rates in saturated nucleate pool boiling-A wide-ranging examination using reduced properties," *Adv. Heat Transf.*, vol. 16, no. C, pp. 157–239, 1984.

[96] L. A. Campbell, R. Simons, and M. J. Ellsworth, "Experimental Investigation of the Heat Transfer Performance of Arrays of Round Jets With Sharp-Edged Orifices and Peripheral Effluent: Convective Behavior of Water on a Heated Silicon Surface," in *ASME 2005 Summer Heat Transfer Conference collocated with the ASME 2005 Pacific Rim Technical Conference and Exhibition on Integration and Packaging of MEMS, NEMS, and Electronic Systems*, 2005, pp. 1–8.

[97] M. J. Rau, "Turbulent liquid-vapor flow interactions and heat transfer in confined jet impingement boiling," Purdue University, 2015.

APPENDIX A. VALIDATION OF LIQUID-VAPOR INTERFACE RECONSTRUCTION TECHNIQUE

The liquid-vapor interface reconstruction technique is validated by imaging samples of known geometry. The samples are thin-walled, hollow, transparent and smooth plastic spheres (diameters of 30, 40 and 50 mm) with light-gray speckle pattern painted on the exterior surface. The use of transparent and smooth plastic samples mimics the transparency and specular reflectivity of liquid-vapor interfaces, which deviate from the typical opaque and diffuse reflecting objects that are used in standard stereo surface reconstruction, and can induce ambiguity during the correspondence search. Also, the transparency of the samples replicates the non-uniform illumination characteristics of real vapor bubbles that result from the lensing effect of curved objects immersed in a medium of higher optical density. The speckle pattern is widely used in the digital image correlation community and provides randomly distributed features of different sizes that are favorable for the correspondence search. The characteristics of the actual liquid-vapor interfaces that form during boiling are extremely difficult to replicate in a controlled and representative manner; however, the texture captured in the acquired images for vapor structures generally appear to have randomness in shape and orientation. The spherical shape of the samples allows evaluation of the effects of the disparity gradient on the correspondence search due to distortion of features between the left and right views. A spherical surface covers the entire range of orientations of surface patches with respect to the camera configuration, which is critical because the magnitude of the disparity gradient increases with inclination. Disparity gradients also intensify with increasing curvature; hence, samples of different radii are considered in the validation.

The validation samples are place inside the test section filled with deionized water at room temperature. Stereoscopic images of the samples are taken using the same camera configuration as for the images acquired during the pool boiling experiments. Figure A.1a presents the left grayscale images of the validation samples. The reconstruction of the front surface of the validation samples is performed following the same general process as for the pool boiling images. The only differences are the manual creation of the masks due to the simple geometry, and the use of single-frame correlation because the validation samples are static. The parameters for feature extraction, corresponding search and reconstruction filtering are identical

as for the pool boiling images. For estimating the error in the reconstruction results, the location of the center of each sample is found by fitting a spherical surface of fixed known diameter to the reconstructed surface. To facilitate the interpretation of the results, the reconstructed surfaces are translated to make the coordinates origin coincident with the center of the samples. Figure A.1b presents the resulting reconstructions for the validation samples with dimensions normalized by the sample radius. The surface reconstructions exhibit some discontinuities on the periphery due to reduced contrast in the captured features and significant distortion of the features between views. Discontinuities are also observed near the center of each reconstruction, where the reconstruction process is affected by ambiguity between the features on the front surface and features on the rear surface and by the distorted image of the rear illumination window that is generated due to the sample lensing effect; similar discontinuities are observed in the reconstruction of real vapor bubbles. The error is computed as the difference between the sample radius and the distance of the reconstructed points to the sample center. Figure A.1c presents the reconstruction error map normalized by the validation sample radius. The reconstruction error is low, aside from outliers near the previously mentioned discontinuities. Figure A.1d presents the probability distribution of the normalized error for the three samples. The normalized error distribution becomes narrower with increasing sample size, which is a consequence of the error normalization. Standard bounds for the normalized error, *i.e.* 68.5% coverage, are 0.024, 0.016, 0.014, which correspond to dimensional standard bounds of 0.36 mm, 0.32 mm and 0.35 mm for samples diameters of 30, 40 and 50 mm respectively.

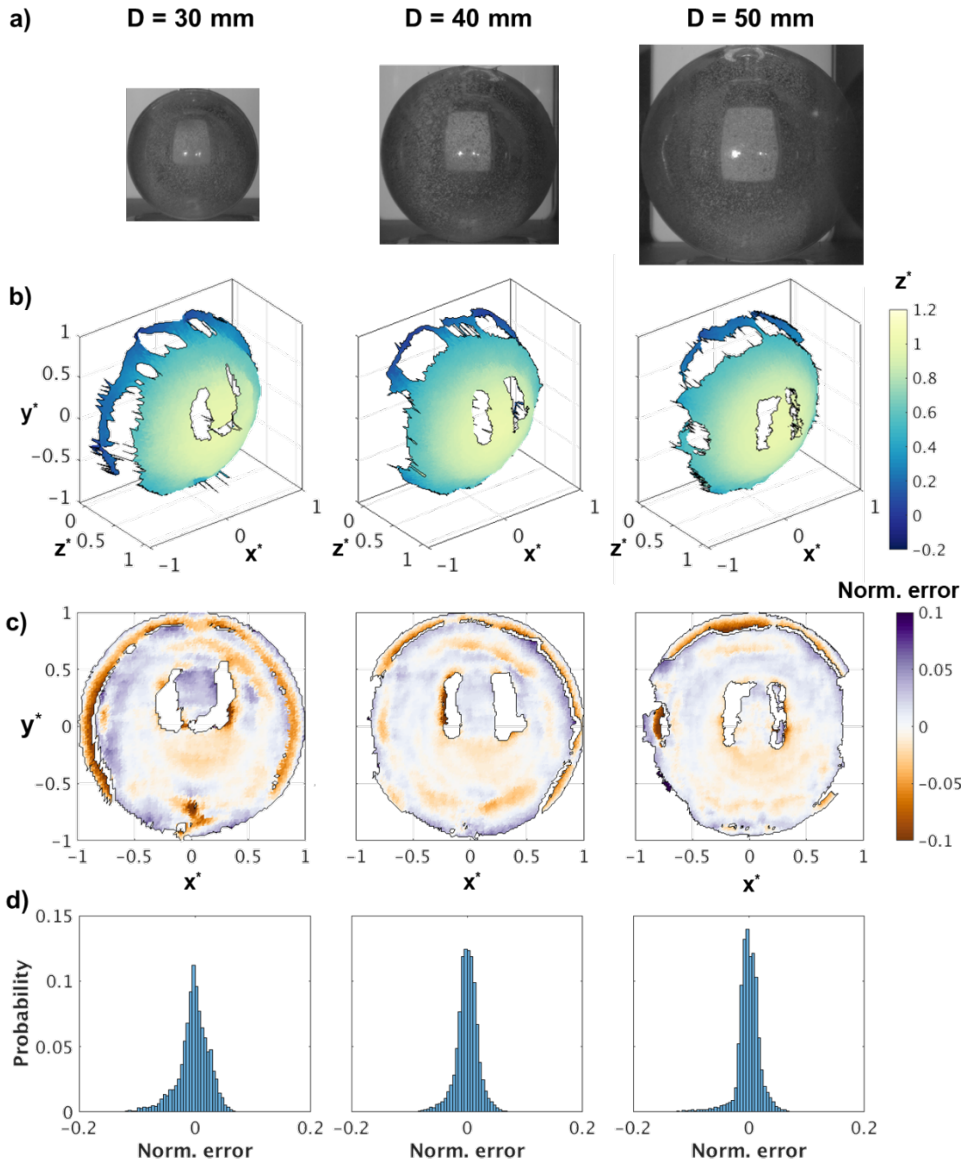

Figure A.1. Validation samples (a) original left grayscale image, (b) reconstructed surface and depth map, (c) normalized error map, and (d) normalized error distribution.

APPENDIX B. PINHOLE CAMERA MODEL PARAMETERS AND CAMERA CALIBRATION PROCEDURE

B.1 Pinhole Camera Model

The pinhole camera model establishes the relationship between three-dimensional coordinates of points with respect a world coordinate system and pixel coordinates. The parameters of the pinhole camera model used in the present thesis correspond to those proposed by Tsai [57], and are classified as external and internal. The external parameters define a coordinate transformation from the world coordinate system to the camera coordinate system. The origin of the camera coordinate system is located at the center of projection. The coordinate transformation is of the following form:

$$\vec{X}_c = \mathbf{R}\vec{X}_w + \vec{T} \tag{B.1}$$

where, $\vec{T}$ is a translation vector of components $\left[T_x, T_y, T_z\right]$ and **R** is a rotation matrix of the form:

$$\mathbf{R} = \begin{bmatrix} r_{11} & r_{12} & r_{13} \\ r_{21} & r_{22} & r_{23} \\ r_{31} & r_{32} & r_{33} \end{bmatrix} = \begin{bmatrix} \cos\theta_z & \sin\theta_z & 0 \\ -\sin\theta_z & \cos\theta_z & 0 \\ 0 & 0 & 1 \end{bmatrix} \begin{bmatrix} \cos\theta_y & 0 & -\sin\theta_y \\ 0 & 1 & 0 \\ \sin\theta_y & 0 & \cos\theta_y \end{bmatrix} \begin{bmatrix} 1 & 0 & 0 \\ 0 & \cos\theta_x & \sin\theta_x \\ 0 & -\sin\theta_x & \cos\theta_x \end{bmatrix}$$

The internal parameters determine the location of the projection plate (focal length) and the transformation from image plane coordinates to pixel coordinates. The undistorted coordinates of projected points are found as:

$$\begin{aligned} x_u &= f\frac{X_c}{Z_c} \\ y_u &= f\frac{Y_c}{Z_c} \end{aligned} \tag{B.2}$$

A radial distortion model is used to account for non-linear effects induced by the optical system. In this these, only second-order radial distortion is considered, and the relationship between distorted and undistorted coordinates is found as:

$$\begin{aligned} x_u &= x_d\left(1 + k_1 r_d^2\right) \\ y_u &= y_d\left(1 + k_1 r_d^2\right) \end{aligned} \tag{B.3}$$

where, $r = \sqrt{x_d^2 + y_d^2}$ is the distance from the optical center. Finally, considering parameters specific to the camera sensor of image center, separation between pixels and pixel skew factor, the pixel coordinates are determined as:

$$u = -\frac{s_x}{d_{pix}} x_d + u_0$$
$$v = -\frac{1}{d_{pix}} y_d + v_0 \tag{B.4}$$

B.2 Camera Calibration Procedure

The calibration image processing and estimation of pinhole camera parameters are performed with an in-house code using MATLAB [61]. Starting from acquired calibration images, the camera calibration procedure continues with determining, for each image, the pixel coordinates for the dots in the calibration target. For processing the calibration images, a simple graphical user interface is developed and shown in Figure B.1. The user performs and defines the parameters for the following steps.

1) Create of mask of region in image with calibration dots.
2) Binarize image of calibration target. To account for illumination gradients, a local threshold is defined by bi-linear interpolation of threshold values for the image corners. The user needs to judge that the calibration dots appear in the binarized image with similar size when choosing the thresholds for the corners.
3) Detect calibration dots. The MATLAB function regionprops is used for this step.
4) Arrange detected calibration dots. The user chooses the dot at the origin of the coordinate system, the first dot in the x-direction and the first dot in the y-direction.
5) Define physical parameters of the calibration target (dot spacing, plane spacing and z-coordinate of first calibration plane).
6) Export pixel and world coordinates of calibration dots.

Once the coordinates of the calibration dots have been determined, the camera parameters that best fit the pinhole model are found. A first estimate of the pseudo-camera parameters is obtained following the procedure outlined by Tsai [57], in which distortion effects are neglected and the pixel size and pixel coordinates for the image center are assumed to be known. The estimate is further refined using Levenberg-Marquardt optimization algorithm [58,59].

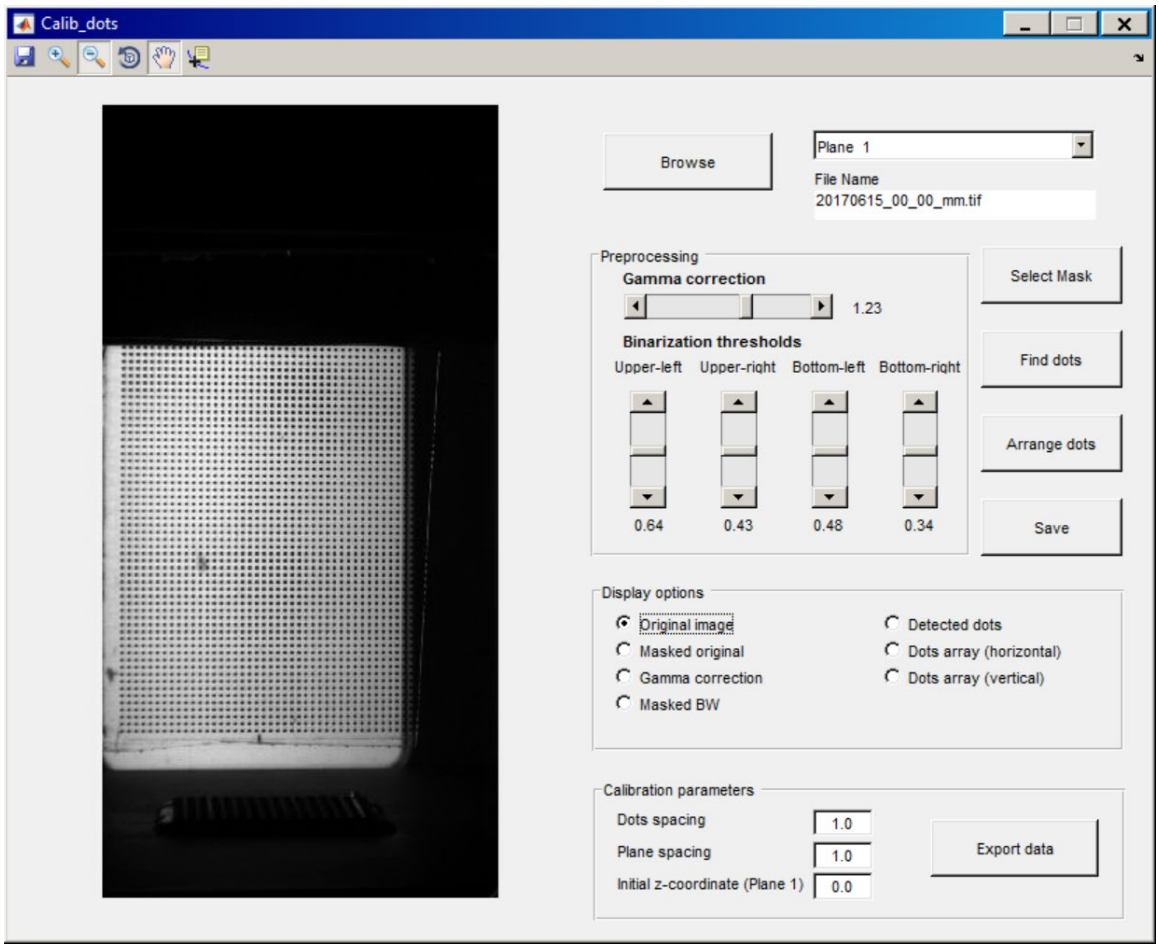

Figure B.1. MATLAB graphical user interface for image processing of calibration target images.

APPENDIX C. SEMI-EMPIRICAL MODEL FOR TWO-PHASE HEAT TRANSFER FROM ARRAYS OF IMPINGING

Two-phase jet impingement is an attractive approach for cooling densely packed electronics systems due to the integration of highly effective heat transport mechanisms into a compact and flexible design. The heat transfer behavior of an impinging jet array is dependent on many design parameters, such as the orifice dimensions, array size and distribution, orifice-to-target spacing, and operating/boundary conditions, as illustrated in Figure C.1. Prediction of the heat transfer performance when the jets undergo phase change is particularly challenging due to the coupled phase-change phenomena and flow dynamics. On the other hand, exhaustive parametric evaluation via experimentation is infeasible.

A semi-empirical is developed and validated for the prediction of area-averaged two-phase heat transfer from a surface subjected to jet array impingement. The model considers confined and submerged liquid jet arrays impinging on a smooth, flat surface generating a uniform heat flux. The modeling approach is based on experimental observations of single-phase and boiling heat transfer occurring simultaneously at different portions of the surface. The model separately treats the single-phase and boiling regions, and thereby is uniquely able to provide performance predictions across the single-phase, partial boiling, and fully boiling heat transfer regimes. Correlations from the literature are used to predict the single- and two-phase heat transfer coefficients in sub-regions of a unit cell under each jet. An analysis is performed to assess sensitivity of the model outputs to changes in key input parameters. Experiments are performed for different orifice-to-target spacings and array geometries to validate the model. The model predictions are also compared against experimental data available in the literature. This study was performed in collaboration with Matthew D. Clark who performed the experiments. A version of the materials in this Appendix have been published in the International Journal of Heat and Mass Transfer [43].

C.1 Model Description

The jet impingement system being modeled is illustrated in Figure C.2. Liquid jets are formed when subcooled liquid passes through an orifice plate with a square array of circular

orifices. The flow through all the orifices is assumed to have the same, constant inlet temperature and to be equally distributed among the orifices, yielding jets of the same velocity. The jets issue into a gap filled with the same fluid, leading to a submerged jet impingement situation. The jets impinge on a flat surface that is being heated at a uniform flux. As heat is removed from the surface and the temperature of the fluid increases, boiling may occur either in selected regions or over the entire surface. After impingement, the spent fluid is forced outwards through the confinement gap bounded on the top and bottom by the orifice plate and the impingement surface, respectively. The resultant average temperature of the surface depends on a set of geometrical parameters, operating conditions, and fluid properties. The geometrical parameters accounted for in the model include the jet diameter, orifice-to-target spacing and jet-to-jet spacing; the operating conditions include the fluid flow rate, operating pressure, inlet subcooling, and surface heat flux.

C.1.1 Unit-Cell-Based Modeling Approach

The jet array is divided into unit cells, as shown in Figure C.2(a), which are assumed to have identical, spatially periodic heat transfer behavior. Inside each unit cell, two distinct regions are identified at each heat flux, namely, a region undergoing single-phase convective heat transfer and another undergoing nucleate boiling heat transfer. Figure C.2(b) shows this division inside each unit cell schematically. These regions are in concordance with the experimental observation of boiling starting at the periphery of the wall jet (in the regions between neighboring jets), and creeping inwards towards the stagnation region as the heat flux increases [75].

As shown in Figure C.2(c), it is assumed that heat transfer in the single-phase region is identical to that for a reference case in which only single-phase jet-impingement heat transfer occurs across the entire unit cell. In the boiling region, on the other hand, a uniform nucleate pool boiling coefficient is assumed, similar to the behavior reported by Rau and Garimella [75]. The area-averaged surface temperature inside the jet unit cell is then found as:

$$\overline{T_s} = \frac{q''}{A_c}\left(\int_{A_{sp}} \frac{1}{h_{ref}(r)} dA + \frac{A_{nb}}{h_{nb}} \right) + T_j \tag{C.1}$$

To delineate the regions, the model assumes that nucleate boiling occurs in those regions of the unit cell where the heat transfer coefficient due to nucleate boiling exceeds that due to

single-phase convection. Hence, the location of the boiling front is defined at the intersection of the single-phase heat transfer profile and the horizontal line representing a constant nucleate pool boiling heat transfer coefficient, as shown in Figure C.2(c). The single-phase heat transfer coefficient is assumed to monotonically decrease from the stagnation point, and a unique intersection point is found at the radial coordinate where:

$$h_{ref}(r)\Big|_{r=r_{nb}} = h_{nb} \tag{C.2}$$

A nucleate pool boiling correlation appropriate for the surface-fluid combination can be used to estimate the boiling heat transfer coefficient. The assumed functional form of the single-phase heat transfer coefficient profile for jet impingement is described in Section C.1.2, and requires as inputs empirical correlations for the area-averaged and the stagnation heat transfer coefficient.

The boiling area is estimated as the area of the square unit cell minus its intersection with a circle of radius r_{nb}. The area of the single-phase region is simply found as:

$$A_{sp} = A_c - A_{nb} \tag{C.3}$$

To facilitate the evaluation of the area-integral in the single-phase region in Eq. (1), this region is approximated as a circular area of radius:

$$r_{sp} = \sqrt{A_{sp}/\pi} \tag{C.4}$$

The average surface temperature is then computed as:

$$\overline{T_s} \approx \frac{q''}{A_c}\left(2\pi\int_0^{r_{sp}} \frac{r}{h_{ref}(r)}dr + \frac{A_{nb}}{h_{nb}}\right) + T_j \tag{C.5}$$

C.1.2 Single-Phase Heat Transfer Coefficient Profile

The single-phase heat transfer profile used in the model is inspired by prior experimental observations during jet impingement of a bell-shaped local heat transfer coefficient distribution with a maximum value at the stagnation point and a monotonic decrease in the outward radial direction [76]. The following function is proposed for the single-phase heat transfer coefficient.

$$\frac{1}{h_{ref}(r)} = \frac{\left(T_{s,ref}(r) - T_j\right)}{q''} = C_1 - C_2 \exp\left(\frac{-r^2}{2\sigma^2}\right) \tag{C.6}$$

The function is expressed as the inverse of the local heat transfer coefficient in order to facilitate the estimation of the area-averaged surface temperature by Eq. (1). The profile does not account

for the possible existence of a secondary peak in the single-phase heat transfer coefficient distribution. Such a secondary peak has been observed in cases with small orifice-to-target spacings, large jet-to-jet spacings, and high Reynolds numbers [77].

The width parameter of the single-phase heat transfer profile, σ, is set as 1, which implies that the inflection point of the profile occurs near the transition from impingement to wall jet behavior at $r/d = 1$. Also, the profile is constrained to comply with the empirical values for the stagnation heat transfer coefficient and the area-averaged heat transfer coefficient:

$$h_{ref}(r)\Big|_{r=0} = h_{0,ref} \tag{C.7}$$

$$\frac{1}{A_c}\int_{A_c}\frac{1}{h_{ref}(r)}dA = \frac{1}{\overline{h}_{ref}} \tag{C.8}$$

Correlations appropriate to the specific geometrical parameters and operating conditions can be used for the area-averaged and the stagnation heat transfer coefficient. For the single-phase heat transfer correlations, fluid properties are evaluated at a film temperature, taken as the mean value of the jet inlet temperature and reference average surface temperature that would be achieved by single-phase jet impingement in the absence of boiling.

The square unit cell is approximated to a circular area of radius:

$$r_{eq} = s/\sqrt{\pi} \tag{C.9}$$

Eq. (7) and Eq. (8) are combined to determine the constants in the single-phase heat transfer profile, C_1 and C_2:

$$C_1 = \frac{\dfrac{1}{\overline{h}_{ref}} - \dfrac{1}{h_{0,ref}}\left\{\dfrac{2\sigma^2}{r_{eq}^2}\left[1-\exp\left(\dfrac{-r_{eq}^2}{2\sigma^2}\right)\right]\right\}}{1-\dfrac{2\sigma^2}{r_{eq}^2}\left[1-\exp\left(\dfrac{-r_{eq}^2}{2\sigma^2}\right)\right]} \tag{C.10}$$

$$C_2 = \frac{\dfrac{1}{\overline{h}_{ref}} - \dfrac{1}{h_{0,ref}}}{1-\dfrac{2\sigma^2}{r_{eq}^2}\left[1-\exp\left(\dfrac{-r_{eq}^2}{2\sigma^2}\right)\right]} \tag{C.11}$$

C.2 Experimental Methods

Experiments are conducted to provide data for validation of the modeling approach, namely, the prediction of the area-averaged surface temperature and the different heat transfer modes and transitions that occur during two-phase jet impingement.

C.2.1 Flow Loop

The custom-developed two-phase jet impingement facility used in the experiments is described in detail in Ref. [9] and is shown schematically in Figure C.3. The dielectric liquid HFE-7100 [78] is circulated through the loop by a magnetically coupled gear pump, and the flow rate is coarsely set by tuning the rotation speed of the pump. Fine adjustments to the flow rate are then made using metering valves in the bypass loop line and at the test section inlet. Mass flow rate is measured by a Coriolis flow meter (CMFS015, Emerson) with +/- 0.1% accuracy. Subcooling at the jet inlet is maintained at 8 °C by adjusting the voltage supplied to a 1.2 kW inline preheater. For degassing purposes, the reservoir is equipped with a 1 kW immersion heater and two Graham reflux condensers connected to a chiller. Fluid exiting the reservoir is cooled before entering the pump by a copper-finned liquid-to-air heat exchanger equipped with a voltage-regulated fan; this prevents cavitation in the pump and provides greater control over the jet inlet subcooling temperature.

C.2.2 Test Section

The test section, shown in Figure C.4, was originally developed in Ref. [9] , but the heater assembly was modified for the current study to ensure that the heated surface is completely covered by the jet array, so as to achieve spatially periodic unit cells. The specific modifications include a smaller heater surface area and new orifice plates with the jet arrays spanning over a larger area. The walls of the test section are constructed of polyether ether ketone (PEEK) for thermal insulation and include polycarbonate front and back walls for visualization. Fluid enters through the top of the test section into the cylindrical plenum, where it passes through two screens and a honeycomb to condition the flow. Inlet pressure and temperature are respectively measured by a pressure tap and a T-type thermocouple placed just upstream of the jet array. The jet array is formed by an interchangeable orifice plate sealed by an O-ring to the bottom of the plenum. Two different array geometries are studied for the current

experiments, namely, a 3 × 3 square array of 2 mm-diameter round jets and a 5 × 5 square array of 1.2 mm-diameter round jets. In both cases, the orifice aspect ratio *l/d* is chosen to be 2 and the nondimensional jet-to-jet spacing *s/d* is 3.33. Both arrays have the same total open orifice area, resulting in equal jet velocities for a given flow rate. The orifice-to-target spacing (*H/d*) is precisely set by resting the orifice plate on three spacer pins inserted into the bottom of the test section. An O-ring creates a seal between the plenum and the PEEK ceiling of the test section, allowing the plenum to translate vertically so that its position can be adjusted to provide the required confinement height.

Jets issue from the orifice plate into submerged conditions and spent fluid exits through an outlet port at the top of the test section. Pressure at the outlet of the jets is measured with a pressure tap (Gems 2200BG3F002A3UA) in the bottom of the test section. Insertion of a T-type thermocouple through the side wall of the test section allows measurement of the fluid bath temperature.

The jets impinge on a 20 mm × 20 mm square heated surface, which is aligned such that it is completely covered by an integer number of square unit cells with a side length equal to the jet-to-jet spacing (3.33 jet diameters). The test surface is heated by means of twelve 100 W cartridge heaters inserted into the bottom of an oxygen-free copper block. The copper block is equipped with three thermocouple rakes located along the centerline and along two opposing sidewalls of the block, which allow for calculation of the area-averaged surface temperature from extrapolated surface values obtained for the three rakes. The centerline rake consists of four T-type thermocouples inserted at 2.54 mm intervals in the vertical direction. The near-sidewall rakes consist of two T-type thermocouples each, spaced by 7.62 mm vertically. Fiberglass insulation is packed into the cavities between the heater block and the surrounding PEEK carrier; the heater block is supported from below by a ceramic block to provide further insulation. The smooth top surface of the heater is mounted flush with the bottom of the test section and a small bead of sealant (Q3-6611, Dow Corning) is carefully applied into a 1 mm chamfer cut into the tightly fitting 4 mm thick PEEK plate surrounding the edges of the test surface. By applying the sealant into a recessed chamfer, the bead can be made smooth and flush with the upper edges of the heater block and the surrounding PEEK plate, while maintaining proper adhesion to the copper side walls.

C.2.3 Experimental Procedure

Prior to each test run, the HFE-7100 in the flow loop is degassed by circulating it at a flow rate of 650 ml/min while using the immersion heater and the inline heater to boil the fluid. Noncondensable gases are allowed to vent to the atmosphere through the two Graham reflux condensers on the reservoir. This initial degassing procedure is carried out for 2 h. During experimentation, the facility is run in an open-loop configuration, using the immersion heater to maintain the fluid in the reservoir at the saturation temperature corresponding to the atmospheric pressure (101.3 kPa), while continuing to vent noncondensable gases to the atmosphere. This ensures that the HFE-7100 remains degassed throughout the experiment.

The HFE-7100 flow rate desired for testing (1300 ml/min in all cases presented here) is then set, and the power input to the inline heater is adjusted to maintain an inlet subcooling of 8 °C, relative to the saturation temperature calculated according to the outlet pressure. Power input to the heater block is incremented in steps of 8 W, and 2 min of steady-state data are collected at each step. The system is considered to be at a steady state when a surface temperature change of less than 1 °C/h is measured. Data are recorded at a frequency of 0.5 Hz, capturing 60 steady-state measurements per step.

Experiments were performed at nondimensional orifice-to-target distances (H/d) of 4, 1, and 0.5 for the 3 × 3 array, corresponding to actual confinement heights (H) of 8 mm, 2 mm, and 1 mm, respectively. Nondimensional orifice-to-target distances of 4 and 1 were tested for the 5 × 5 array, corresponding to actual confinement heights of 4.8 mm and 1.2 mm, respectively. All experiments were carried through to a critical heat flux condition, as indicated by a rapid surface temperature rise upon incrementing power to the heater block. The final reported data point corresponds to the steady-state data recorded prior to the sudden temperature rise. A summary of experimental conditions is provided in Table C.1.

C.2.4 Data Reduction

The area-averaged surface temperature of the copper heater is extrapolated from the temperature gradient inside the block measured by the thermocouple rakes, assuming one-dimensional conduction. Thermocouple measurement uncertainties are estimated to be ±0.3 °C, such that the average surface temperature extrapolation resulted in an uncertainty from ±0.4 °C at a low heat flux to ±0.6 °C at the maximum heat flux of 49 W/cm^2. Heat loss from the block is

estimated by a numerical heat loss model, following the procedure in Ref. [9], and is subtracted from the electrical power supplied to the heater for calculation of heat flux to the fluid. Uncertainty in heat flux was estimated to be less than 2% based on a 95% confidence interval. All uncertainties are calculated as described in Ref. [9].

C.3 Predicted Behavior and Model Sensitivity

To demonstrate the heat transfer behavior predicted by the model as a function of heat flux, a baseline array geometry is chosen that matches one of the current experimental cases. This geometry consists of a 3 × 3 array of 2 mm-diameter round orifices with an aspect ratio (l/d) of 2, an orifice-to-target spacing (H/d) of 4, and jet-to-jet spacing (s/d) of 3.33. As in the current experiments, the working fluid is HFE-7100 with an inlet subcooling of 8 °C (T_{in} = 51 °C), operating pressure of 101.3 kPa, and jet velocities of 1 and 4 m/s. For this baseline geometry and operating conditions, the same correlations are used as for the model validation in Section C.4.1 as presented in Table C.2. At this baseline, the sensitivity of the model predictions to changes in key model input variables is also assessed by calculating the bounds of the model outputs for a $\pm 15\%$ change from the baseline case in each of the model input variables considered. The four model input variables studied are the average single-phase Nusselt number ($\overline{\mathrm{Nu}}_{ref}$), the single-phase stagnation Nusselt number ($\mathrm{Nu}_{0,ref}$), the single-phase width parameter (σ), and the nucleate boiling heat transfer coefficient (h_{nb}). The variables allow an assessment of the sensitivity of the model to the primary empirical inputs in each heat transfer regime, as well as a confirmation that the assumed functional form of the single-phase heat transfer profile does not significantly influence the predictions.

In Figure C.5(a), boiling curves show the predicted surface superheat (defined as the difference between the area-averaged surface temperature and the saturation temperature of the fluid ($\overline{T}_s - T_{sat}$)) as a function of the surface heat flux. The bounding envelopes in Figure C.5(a) correspond to the deviation of predicted superheat from the baseline prediction, represented by a solid black line, for changes in two empirical inputs. The blue shaded envelope corresponds to a ±15% change in the average single-phase Nusselt number ($\overline{\mathrm{Nu}}_{ref}$), while the gray shaded envelope corresponds to a ±15% change in the nucleate pool boiling heat transfer coefficient (h_{nb}). In Figure C.5(b), the predicted normalized heat transfer coefficient distributions (h/h_0) are

plotted within a unit cell for three different heat fluxes at the higher jet velocity of 4 m/s; these predictions correspond to the baseline values as indicated by the matching symbols on the boiling curves in Figure C.5(a).

While prediction of the *local* heat transfer coefficient distributions is not the objective of the model, Figure C.5(b) is useful to illustrate the heat transfer behavior predicted by the model as a function of heat flux. The three heat fluxes shown in Figure C.5(b) are chosen to represent the three main regimes in two-phase jet impingement: the single-phase regime, the partial boiling regime, and the fully boiling regime. During purely single-phase operation at 12 W/m^2, the model predicts a local heat transfer coefficient distribution strictly according to the proposed single-phase profile. During the partial boiling regime, at 18 W/m^2, boiling is predicted to occur over an outer region within each jet unit cell, and a transition can be seen from the bell-shaped single-phase profile to the constant nucleate pool boiling heat transfer coefficient. During the fully boiling regime, at 25 W/m^2, the model predicts boiling to occur across the entire surface. At low heat fluxes, the area-averaged behavior in Figure C.5(a) follows the single-phase prediction, which has a constant area-averaged heat transfer coefficient with increasing heat flux, seen as a linear slope in the boiling curves. Once boiling begins in the partial boiling regime, the area-averaged heat transfer coefficient increases due to inclusion of the nucleate boiling heat transfer coefficient (h_{nb}) in the boiling regions on the surface. The curves in Figure C.5(a) corresponding to two different jet velocities converge in the fully boiling regime. The average heat transfer coefficient in this regime is equal to h_{nb}, which is independent of jet velocity.

The bounding envelopes in Figure C.5(a) show the sensitivity of the model to changes in the average single-phase Nusselt number ($\overline{\mathrm{Nu}}_{ref}$) and nucleate boiling heat transfer coefficient (h_{nb}) traversing the regimes as a function of heat flux. In the single-phase regime, an increase in $\overline{\mathrm{Nu}}_{ref}$ delays the appearance of nucleate boiling to higher heat fluxes; this is because the nucleate boiling heat transfer coefficient must exceed a higher single-phase heat transfer coefficient per the transition criteria imposed by the model. As the boiling front creeps inward toward the center of each jet unit cell in the partial boiling regime, the nucleate boiling heat transfer increasingly becomes the dominant heat transfer mechanism, reducing the impact of changes in $\overline{\mathrm{Nu}}_{ref}$ on the predictions and increasing the impact of h_{nb}. In the fully boiling regime, h_{nb} exclusively impacts the predicted superheat. These sensitivity results illustrate the critical need to select correlations

appropriate for the specific system under consideration for the current modeling approach to provide accurate predictions.

The effects of changes in the other two parameters on the boiling curve predictions, namely the single-phase stagnation Nusselt number ($Nu_{0,ref}$) and the single-phase width parameter (σ), are not included in Figure C.5(a) for clarity, and because they have a comparatively smaller effect. The single-phase width parameter, σ, primarily affects model predictions in the partial boiling regime; the maximum deviation of predicted superheat is 4.43% (*i.e.*, deviation of 3.04 °C) for a relative change of 15% in σ from the baseline prediction (for which $\sigma = 1$) at a heat flux of 6 W/cm^2 for the jet velocity of 1 m/s. Similarly, the stagnation Nusselt number ($Nu_{0,ref}$) has the greatest impact on the partial boiling regime, though the maximum deviation of predicted superheat is only 0.68% (*i.e.*, deviation of 0.49 °C) for a relative change of 15% in $Nu_{0,ref}$ from the baseline prediction at a heat flux of 16 W/cm^2 for the jet velocity of 4 m/s. While the single-phase width parameter and the stagnation Nusselt number do impact model results, the model predictions are significantly more sensitive to the average single-phase Nusselt number and the nucleate pool boiling heat transfer coefficient.

C.4 Model Validation

For validation of the proposed modeling approach, model predictions are compared with experimental results obtained in the current work as well as those available in the literature for which the geometrical and operating parameters lie within the ranges of available correlations. In addition, comparisons were limited to those studies in which the jet array covers all of a uniformly heated area. While there are a number of experimental studies on two-phase jet array impingement [75,79,88–91,80–87], only Rau and Garimella [75] and de Brún *et al.* [84] meet these criteria and are used in this validation. While Rau and Garimella [75] use a thin-film heater which extends beyond the boundary of the outer jet unit cells in the arrays tested, the lack of lateral conduction in the thin-film and the use of infrared thermography to acquire spatial temperature measurements allow the heat transfer data within the array to be extracted and used for validation. The local temperature data acquired within jet unit cells is also useful for comparison with the local profile predicted by the model. In the experimental study of de Brún *et al.*[84], a 35 mm × 35 mm × 3 mm copper plate is heated from below by a large copper heater over a central 15 mm × 15 mm area. Geometric features are incorporated in the copper plate to

prevent heat spreading outside of the heated area. Because the 15 mm × 15 mm heated area on the copper chip surface extends to the edge of the outer unit cells for their 3 × 3 array of 1 mm jets (s/d = 5), the average surface temperature data reported in Ref. [84] is useful for validation. The working fluids used in these studies are HFE-7100 [75] and distilled water [84]. For each comparison, the choice of correlations from the literature was based on their applicability to the parameter ranges of the experimental data obtained here, as well as their providing the best fit to the data, as we recommend based on the analysis performed in Section C.3.

C.4.1 Comparison to the Current Experimental Results

The predictions of the semi-empirical model developed here are validated against the area-averaged surface temperatures obtained as described in Section C.2.4. The fluid is HFE-7100 and the inlet subcooling is 8 °C. The flow rate for all cases is 1300 ml/min, which corresponds to Reynolds numbers of 5400 for the 3 × array and 3300 for the 5 × 5 array. Three different nondimensional orifice-to-target spacings, H/d, are tested using the 3 × 3 array, namely, 0.5, 1 and 4. Spacings of H/d = 1 and 4 are tested using the 5 × 5 array. Table C.1 summarizes the geometrical parameters and operating conditions. Correlations used in this comparison include: Martin [92] for area-averaged single-phase Nusselt number, Li and Garimella [93] for the stagnation Nusselt number, and Stephan and Abdelsalam [94] for the nucleate boiling heat transfer coefficient (C_4 = 1.7). A summary of these correlations can be found in Table C.2.

The boiling curves obtained from the experiments and predicted by the model for the 3 × 3 and 5 × 5 jet arrays are shown in Figure C.6 and Figure C.7, respectively, with a mean absolute error in the predicted surface temperature of 0.53 °C compared to the experiments. For the three orifice-to-target spacings, the model predicts small differences in the curves in the single-phase and partial boiling regimes; the predicted surface temperatures are identical for all cases when boiling occurs over the entire surface, as the nucleate pool boiling heat transfer coefficient predicted by the correlation is independent of gap height. In the experimental boiling curves, small differences in boiling curve slopes are also observed during single-phase heat transfer among the three orifice-to target spacings, and the magnitude of measured superheat is in reasonable agreement with the model predictions. Discrepancies in superheat within the single-phase regime might be attributed to experimental parameters that are slightly outside the applicability range of the correlations. However, once boiling occurs on the entire surface,

differences in surface superheat between the three confinement heights are much smaller than in the single-phase regime, and both the experimental boiling curves and model predictions converge. The temperature overshoot just before boiling incipience is commonly observed when a highly wetting fluid is used [9]; this phenomenon is not captured by the model.

C.4.2 Comparison to Studies in the Literature

The model predictions are first compared to local heat transfer results obtained for arrays of impinging jets by Rau and Garimella [75]. In this prior study, a thin-foil heater backed by an infrared-transparent window allowed localized temperature mapping of the heated surface during two-phase jet impingement. The fluid used was HFE-7100. Table C.3 summarizes the geometrical parameters and operating conditions for the experiments in [75]. Correlations used in evaluation of the model for comparison to this data again include Martin [92] for area-averaged single-phase Nusselt number, and Li and Garimella [93] for the stagnation Nusselt number. In addition, Cooper's [95] correlation is used for the nucleate boiling heat transfer coefficient (R_p = 1 μm).

Figure C.8 and Figure C.9 compare model predictions with the experimental data [75] for the 3 × 3 and 5 × 5 jet arrays, respectively. The experimental data lie exclusively in either the single-phase regime or the partial boiling regime, because the experiments were terminated prior to boiling having been initiated over the entire surface. This partial boiling regime is critical to assess the model accuracy, as discussed in Section C.3, because the model predictions are sensitive to the assumptions regarding the single-phase heat transfer coefficient distribution and the location of the boiling front. Excellent agreement is observed between the predicted and measured boiling curves based on the area-averaged surface temperature for all of the regimes (Figure C.8(a) and Figure C.9(a)), with a mean absolute error in the predicted surface temperature of 0.79 °C compared to the experimental data.

The local heat transfer coefficient distribution characteristics underpin the estimate of area-averaged surface temperature. Figure C.8(b) and Figure C.9(b) compare the predicted and measured local heat transfer coefficients as a function of the radial coordinate and normalized with respect to the value at the stagnation point, for the maximum heat flux tested. The model predicts a bell-shaped distribution of the heat transfer coefficient in the single-phase region, and a uniform heat transfer coefficient in the boiling region. The experimental local heat transfer

coefficient profile is obtained by averaging values along annular bands. There is reasonable agreement between the heat transfer coefficient profile assumed by the semi-empirical model and the local experimental data in the single-phase and boiling regions.

The excellent agreement of the predictions for the area-averaged surface temperature within the single-phase regime of the boiling curves (Figure C.8(a) and Figure C.9(a)) indicates that Martin's correlation [92] accurately estimates the single-phase area-averaged Nusselt number for this experiment. Also, from the data for the local heat transfer coefficients (Figure C.8(b) and Figure C.9(b)), it is apparent that the boiling heat transfer coefficient measured in Ref.[75] is well-represented by the Cooper correlation [95]. However, the stagnation heat transfer coefficient is, in general, slightly over-predicted by the correlation of Li and Garimella [93]; the discrepancies may be due to the use of the correlation outside the original ranges for which it was developed.

Area-averaged results from a recent study by de Brún *et al.*[84] are now compared against model predictions in Figure C.10. The geometric configuration consists of a 3 × 3 array of 1 mm diameter jets, jet-to-jet spacing (s/d) of 5, and an orifice-to-target distance (H/d) of 2. The jets of distilled water impinge onto a 15 mm × 15 mm copper surface under submerged and confined conditions. The average surface temperature is extrapolated from thermocouples embedded in the copper surface. As summarized in Table C.3, operating parameters include a subcooling of 8 °C and flow rates of 500 mL/min (v_j = 1.18 m/s) and 670 mL/min (v_j = 1.57 m/s). Both of the tests included in this comparison were carried through to a critical heat flux condition. To account for the lower confinement height (H/d = 2), the correlation of Campbell *et al.*[96] is used for the area-averaged single-phase Nusselt number. Li and Garimella [93] and Cooper [95] (R_p = 1 μm) are again used for $\mathrm{Nu}_{0,ref}$ and h_{nb}, respectively. The trend in area-averaged single-phase performance with respect to flow rate is properly captured, indicating that the Campbell *et al.* correlation [96] accurately predicts the average single-phase Nusselt number. Partial-boiling heat transfer is represented by the model prediction with reasonable accuracy, and, as suggested by de Brún *et al.*[84], Cooper's correlation [95] predicts the fully boiling regime heat transfer coefficient well. The final jump in surface temperature (shift of the curve to the right in Figure C.10) at the onset of critical heat flux is not captured by the model, which does not include a prediction of critical heat flux. Excluding these points, the mean absolute error in surface temperature prediction is 1.34 °C for this dataset.

C.4.3 Summary of Comparisons

Figure C.11 compares the predicted and measured boiling curves for de Brún *et al.*[84], Rau and Garimella [75], and the jet array configuration investigated in the current study. Apart from the outliers in the current data set due to temperature overshoot at incipience and onset of critical heat flux (denoted as open symbols in Figure C.11), experimental data in all three cases, which include the single-phase, partial boiling, and fully boiling regimes, are well-predicted. The mean absolute percentage error (MAPE) in comparing the current experimental results with model predictions in terms of the difference between surface temperature and jet inlet temperature is 3.61%. In this calculation, the data points corresponding to temperature overshoot at boiling incipience were omitted. For the comparisons to Rau and Garimella [75] and de Brún *et al*. [84], the MAPE is 3.75% and 4.42%, respectively. In the MAPE calculation for de Brún *et al*. [84], the data points corresponding to critical heat flux were omitted. The overall mean absolute error across all experimental data points is 3.88%.

C.5 Conclusions

The sensitivity analysis indicates that the predictions are most sensitive to the average single-phase Nusselt number ($\overline{\mathrm{Nu}}_{ref}$) and the nucleate boiling heat transfer coefficient (h_{nb}), while the single-phase stagnation Nusselt number ($\mathrm{Nu}_{0,ref}$) and the single-phase width parameter (σ) have more modest effects. Sensitivity of the predictions to each of these parameters is dependent on the operating regime. Comparison with experimental obtained in this study and data available in the literature further demonstrates that the proposed approach properly predicts the boiling curve behavior during two-phase jet impingement across single-phase, partial boiling, and fully boiling heat transfer regimes. Across all experimental data comparisons considered, the mean absolute percentage error of model predictions is 3.88%. If appropriate correlations for area-averaged single-phase heat transfer, stagnation point heat transfer, and nucleate pool boiling heat transfer are chosen, the proposed model is capable of accurately predicting two-phase heat transfer from confined and submerged arrays of impinging jets. This modeling approach offers a practical tool in the development of two-phase jet impingement cooling systems, as it allows parametric exploration of the design space.

Table C.1. Geometrical parameters and operating conditions for the two-phase jet array impingement experiments performed in the current study.

N	D (mm)	H/d	s/d	$\dot{V}$ (ml/min)	v_j (m/s)	Re	ΔT_{sub} (°C)	p_{op} (kPa)	Pr
3×3	2	4 1 0.5	3.33	1300	0.77	5450	8	101.3	7.85
5×5	1.2	4 1	3.33	1300	0.77	3300	8	101.3	7.85

Table C.2. Empirical correlations used in model validation with current experimental data set.

Correlation	Ref
Area-averaged single-phase Nusselt number $\overline{\mathrm{Nu}}_{ref} = 0.5\,\mathrm{Re}^{0.667}\,\mathrm{Pr}^{0.42} \times \left\{1+\left(\frac{(H/d)\sqrt{\pi}/2}{0.6(s/d)}\right)^{6}\right\}^{-0.05} \times \left(\frac{\sqrt{\pi}}{s/d}\right)\frac{1-1.1\sqrt{\pi}/(s/d)}{1+0.1(H/d-6)\sqrt{\pi}/(s/d)}$ $2000 \le \mathrm{Re} \le 100{,}000$ $4.43 \le s/d \le 14.01$ $2 \le H/d \le 12$	Martin [92]
Stagnation Nusselt number $\mathrm{Nu}_{0,ref} = 1.409\,\mathrm{Re}^{0.497}\,\mathrm{Pr}^{0.444}\,(l/d)^{-0.058}\,(2r_{eq}/d)^{-0.272}$ $4000 \le \mathrm{Re} \le 23000$ $1.59\ \mathrm{mm} \le d \le 6.35\ \mathrm{mm}$ $1 \le H/d \le 5.0$ $0.25 \le l/d \le 12$ $r_{eq} = 5.64$ $7.1 \le \mathrm{Pr} \le 25.2$	Li and Garimella [93]
Nucleate pool boiling heat transfer coefficient $h_{nb} = C_4 q''^{0.745}$ $3\times10^{-3} \le p_{op}/p_c \le 0.78$ Fluid: Refrigerants	Stephan and Abdelsalam [94]

Table C.3. Geometrical parameters and nominal operating conditions for jet array experiments available in the literature for comparison.

N	d (mm)	H/d	s/d	$\dot{V}$ (ml/min)	v_j (m/s)	p_{op} (kPa)	ΔT_{sub} (°C)	Re_j	Fluid	Ref
3×3	1.25	4	4	450	0.68	120	10	3144	HFE-7100	Rau and Garimella [75]
				900	1.35			6289		
				1800	2.72			12577		
5×5	0.75	4	4	450	0.68	120	10	1887	HFE-7100	Rau and Garimella [75]
				900	1.35			3773		
				1800	2.72			7546		
3×3	1	2	5	500	1.18	100	8	3685	Water	de Brún *et al*. [84]
				670	1.57			4903		

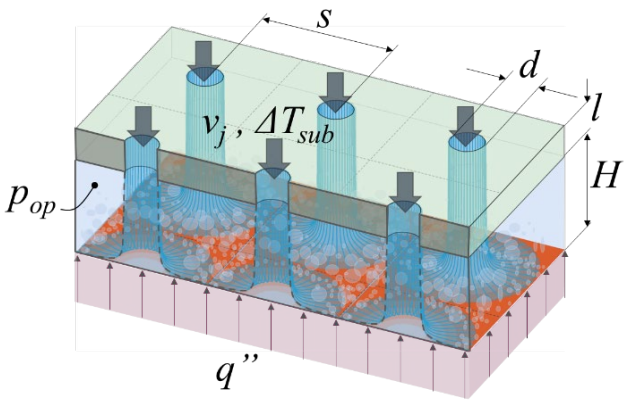

Figure C.1. Geometrical parameters and operating conditions relevant in jet array impingement heat transfer.

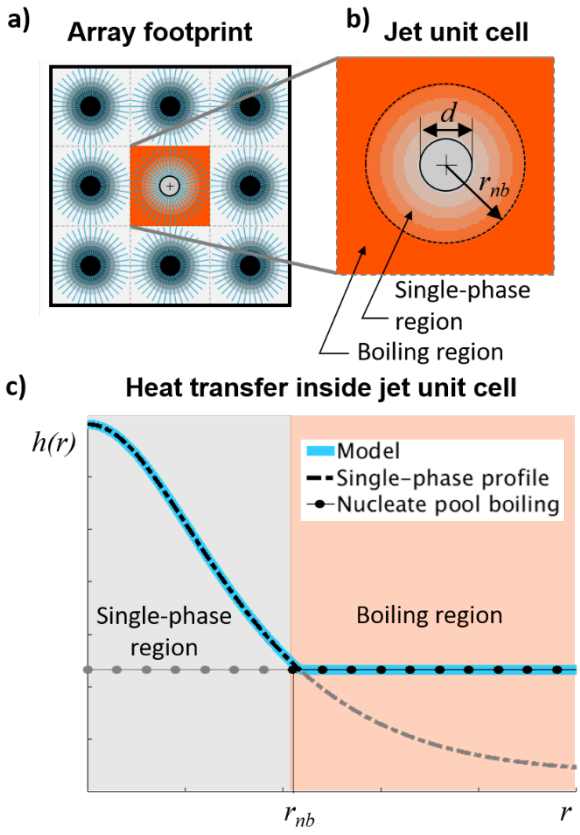

Figure C.2. Modeling approach for (a) heat transfer in a jet array based on the analysis of (b) a jet unit cell, inside which single-phase and boiling regions are defined based on (c) expected distributions of the heat transfer coefficient.

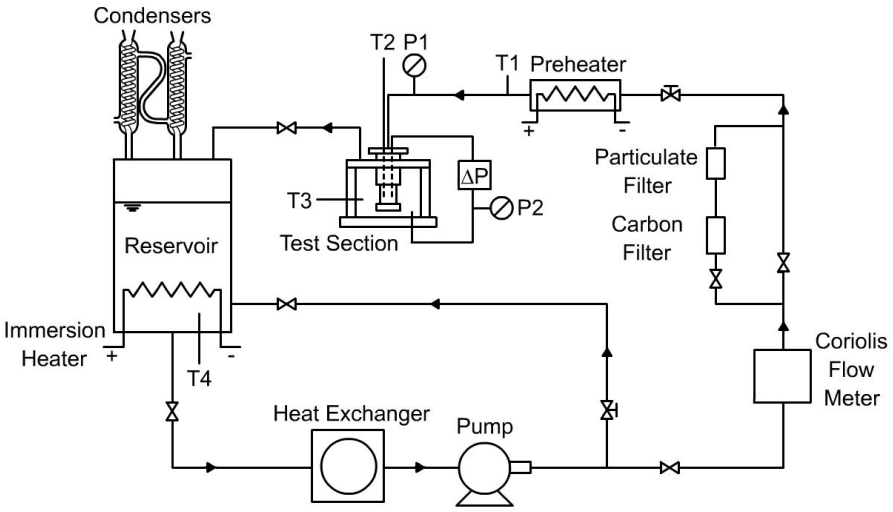

Figure C.3. Flow loop schematic diagram.

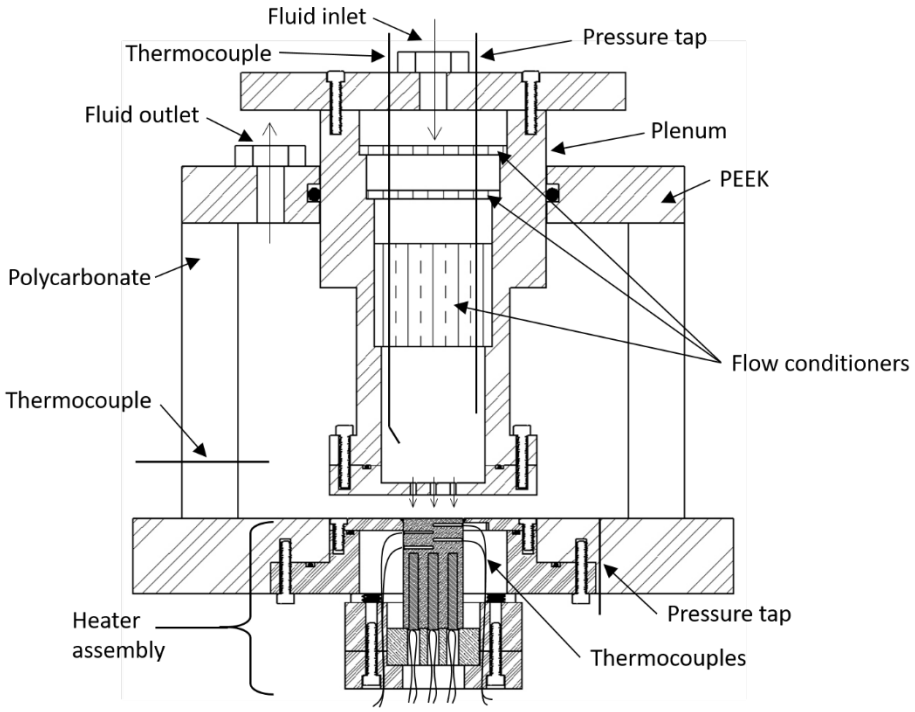

Figure C.4. Cross-sectional view of test section.

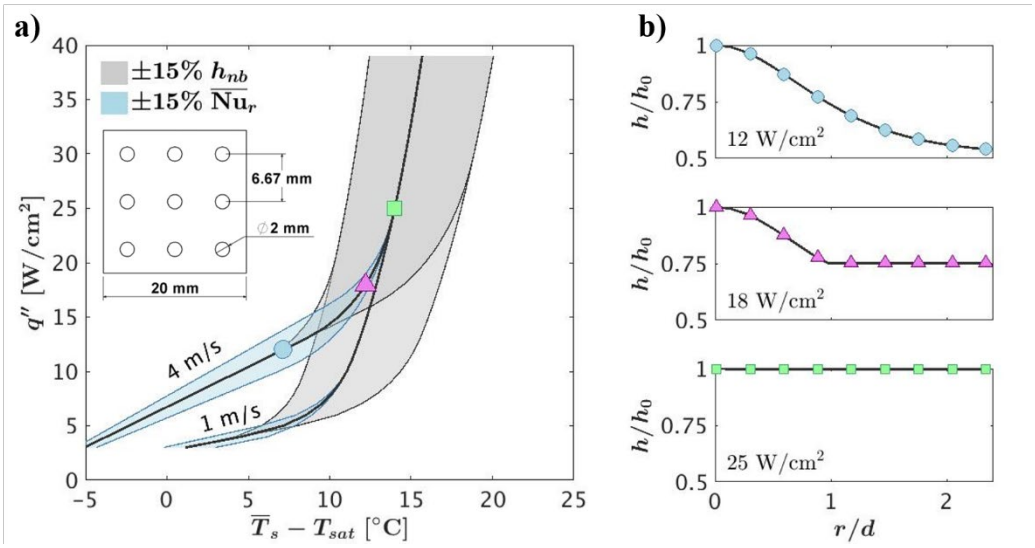

Figure C.5. Sensitivity analysis results: (a) blue and gray shaded envelopes correspond to changes in superheat predictions for a ±15% variations in area-averaged single-phase Nusselt number and nucleate pool boiling heat transfer coefficient, respectively; (b) predicted radial heat transfer coefficient distributions for a single unit cell at three different heat fluxes at a jet velocity of 4 m/s, corresponding to the symbols shown in (a). Correlations used for the baseline prediction: $\overline{\mathrm{Nu}}_{ref}$ [92], $\mathrm{Nu}_{0,ref}$ [93], h_{nb} [94].

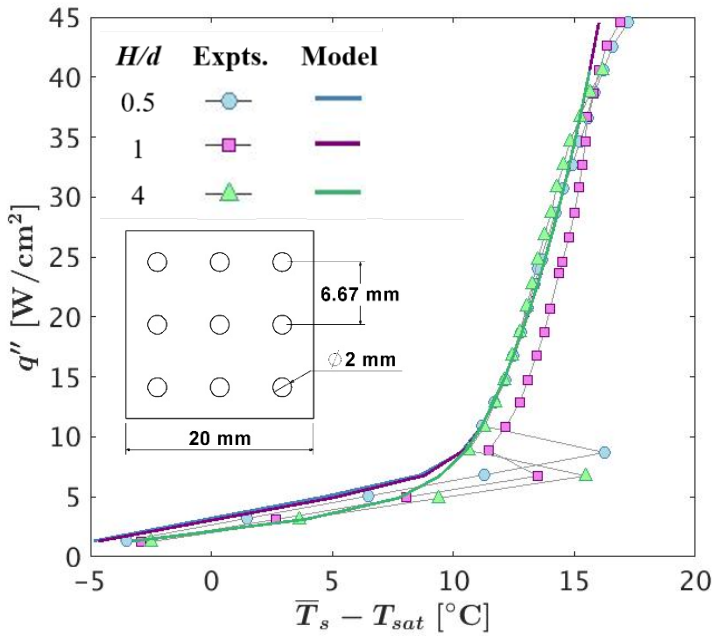

Figure C.6. Model predictions of area-averaged surface superheat for the conditions of Table C.1 for the 3×3 array at a flow rate of 1300 mL/min (v_j = 0.77 m/s) compared to the current experimental data. Correlations used in this comparison: $\overline{\mathrm{Nu}}_{ref}$ [92], $\mathrm{Nu}_{0,ref}$ [93], h_{nb} [94].

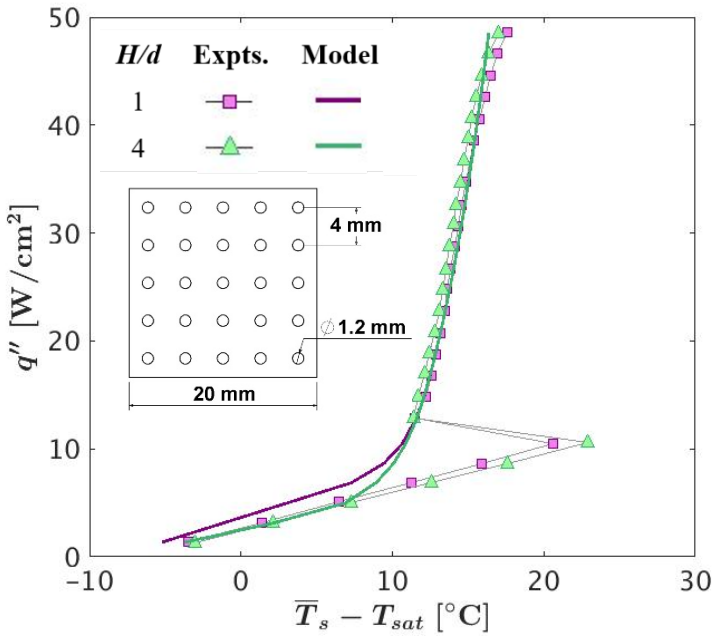

Figure C.7. Model predictions of area-averaged surface superheat for the conditions of Table C.1 for the 5×5 array at a flow rate of 1300 mL/min (v_j = 0.77 m/s) compared to the current experimental data. Correlations used in this comparison: $\overline{\mathrm{Nu}}_{ref}$ [92], $\mathrm{Nu}_{0,ref}$ [93], h_{nb} [94].

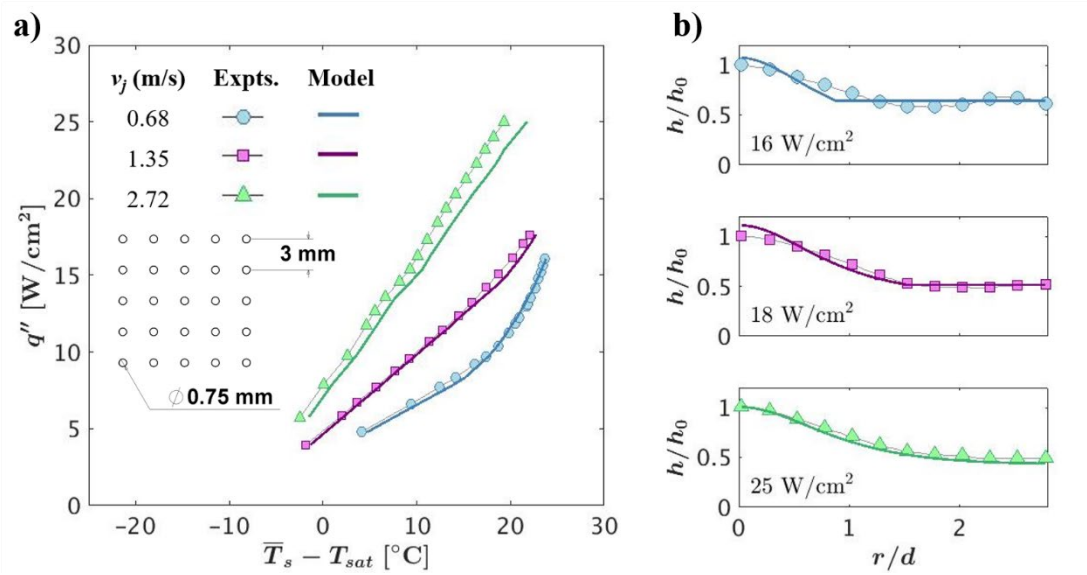

Figure C.8. Model predictions for the conditions of Table C.3 for the 3×3 array compared to the experimental data in [75]: (a) Boiling curves based on the area-averaged surface superheat, and (b) local heat transfer coefficient distributions in the central jet unit cell for the maximum heat flux tested at each jet velocity. Model predictions are shown as solid lines colored to distinguish between the different labelled flow rates. Correlations used in this comparison: $\overline{\mathrm{Nu}}_{ref}$ [92], $\mathrm{Nu}_{0,ref}$ [93], h_{nb} [95].

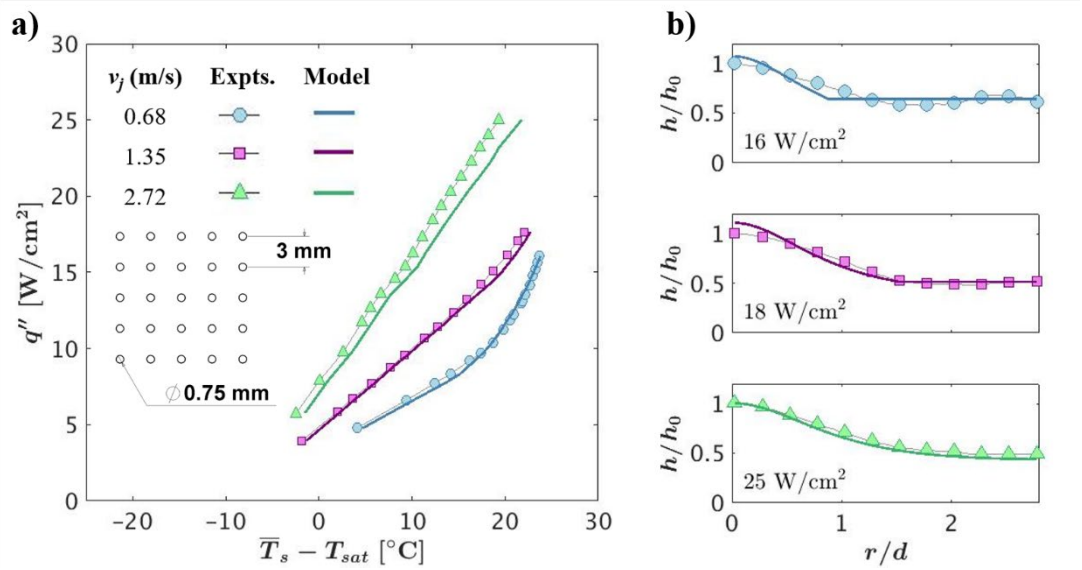

Figure C.9. Model predictions for the conditions of Table C.3 for the 5×5 array compared to the experimental data in [75]: (a) Boiling curves based on area-averaged surface superheat, and (b) local heat transfer coefficient distributions in the central jet unit cell for the maximum heat flux tested at each jet velocity. Model predictions are shown as solid lines colored to distinguish between the different labelled flow rates. Correlations used in this comparison: $\overline{\mathrm{Nu}}_{ref}$ [92], $\mathrm{Nu}_{0,ref}$ [93], h_{nb} [95].

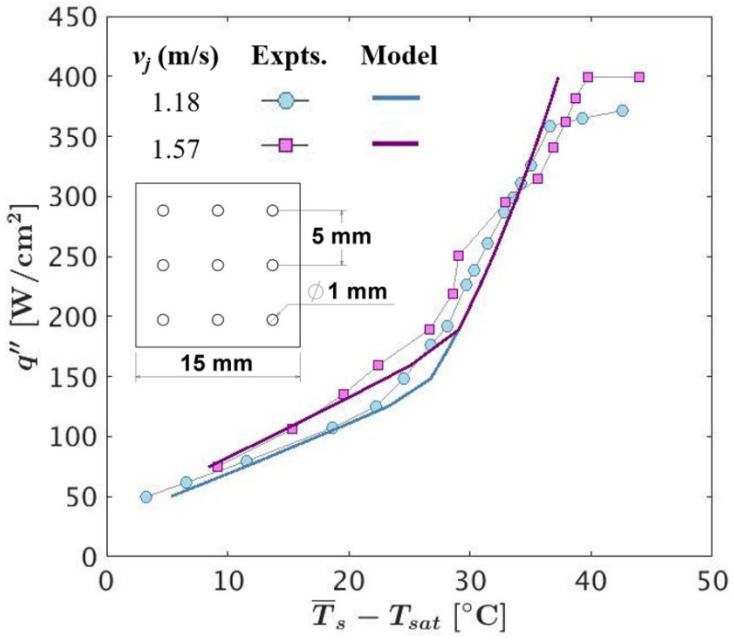

Figure C.10. Comparison of boiling curves predicted by the model against the experimental data of de Brún *et al.* [84] for a 3×3 array and flow rates of 500 mL/min (v_j = 1.18 m/s) and 670 mL/min (v_j = 1.57 m/s). Correlations used in this comparison: $\overline{\mathrm{Nu}}_{ref}$ [96], $\mathrm{Nu}_{0,ref}$ [93], h_{nb} [95].

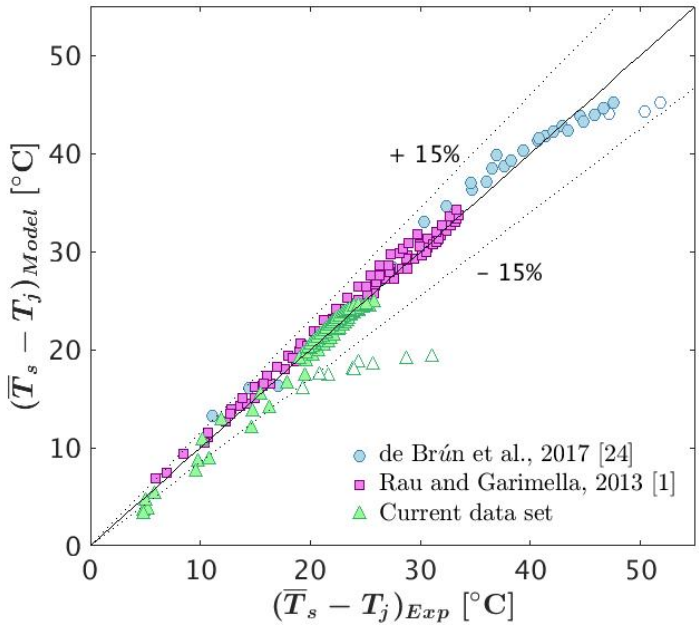

Figure C.11. Comparison of predicted area-averaged surface superheat against experimental results from de Brún *et al.* [84], Rau and Garimella [75], and the current experiments. Empty symbols for the current data set correspond to overshoot at boiling incipience and those for de Brún *et al.* [84] correspond to critical heat flux.

APPENDIX D. DRAWINGS OF THE MODIFIED PLENUM FOR VISUALIZAITON FROM TOP OF THE CONFINEMENT GAP

Technical drawings of the parts of the modified plenum for optical visualization from the top of the confinement gap are included in this Appendix. Details of the other components of the test section that were not modified can be found in Ref. [97].

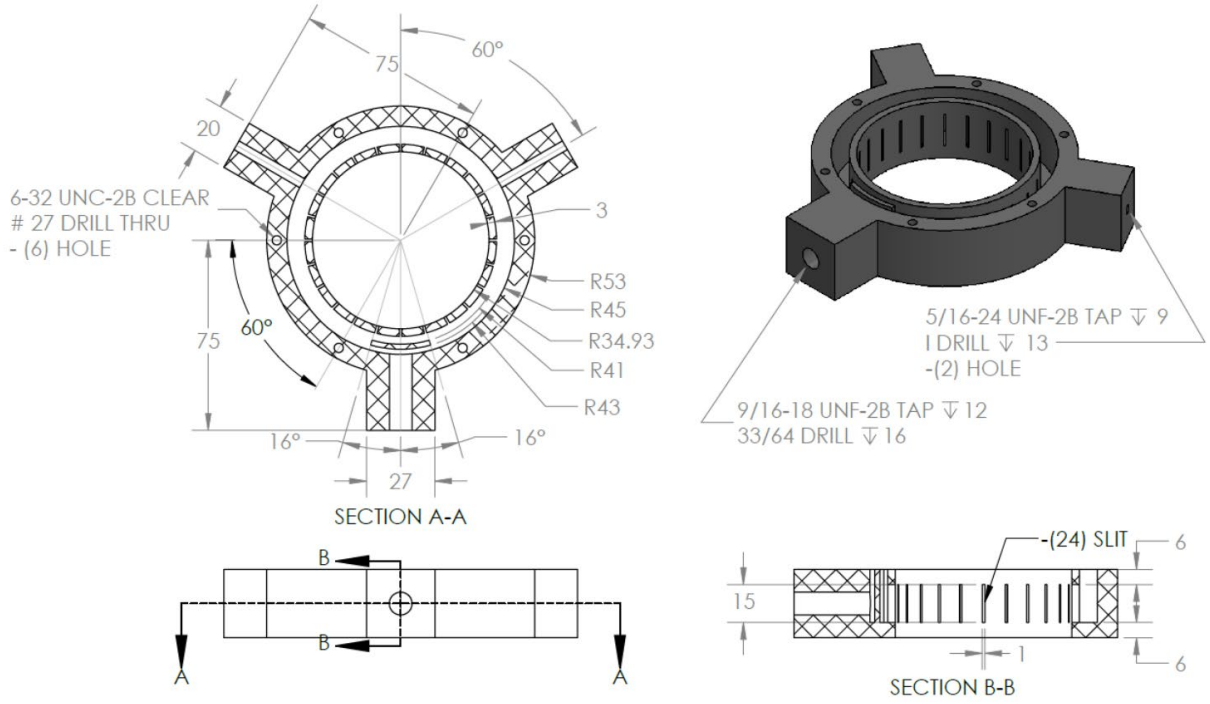

Figure D.1. Radial flow distributor.

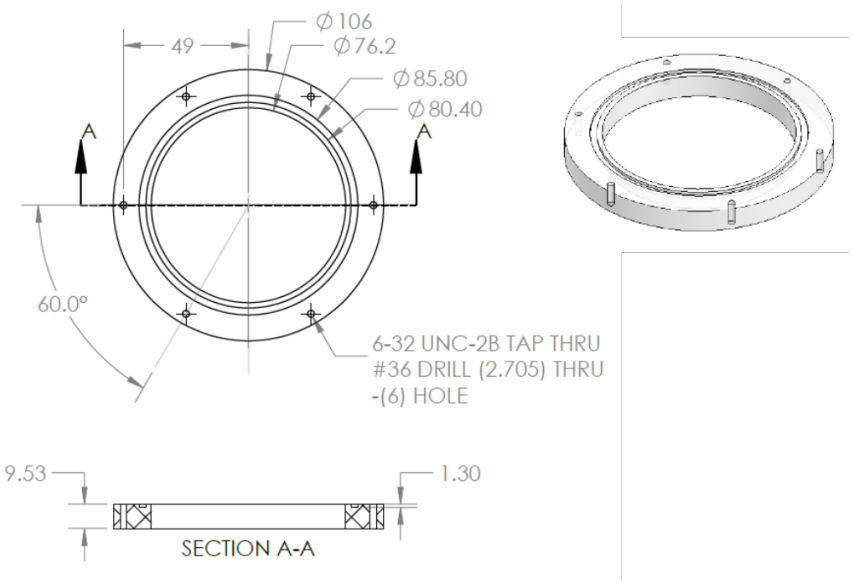

Figure D.2. Plenum top flange.

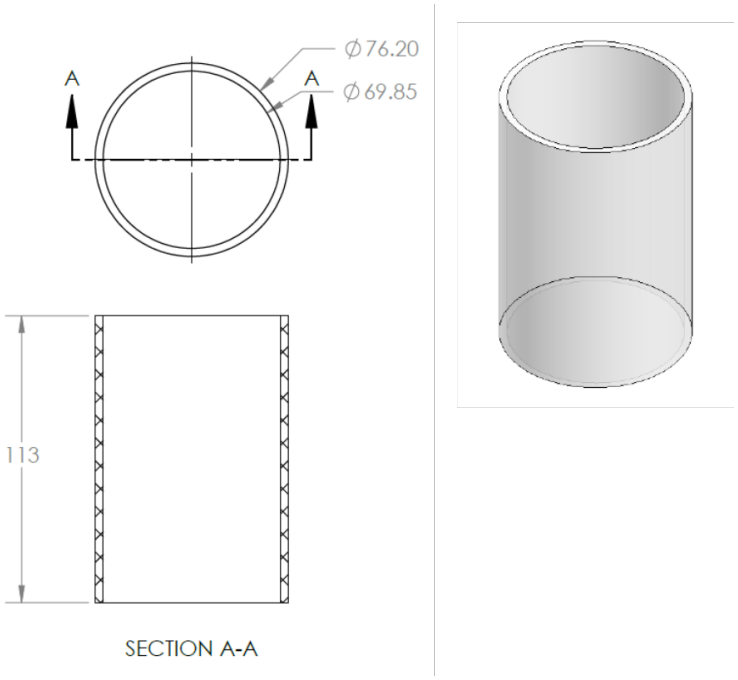

Figure D.3. Plenum straight section.

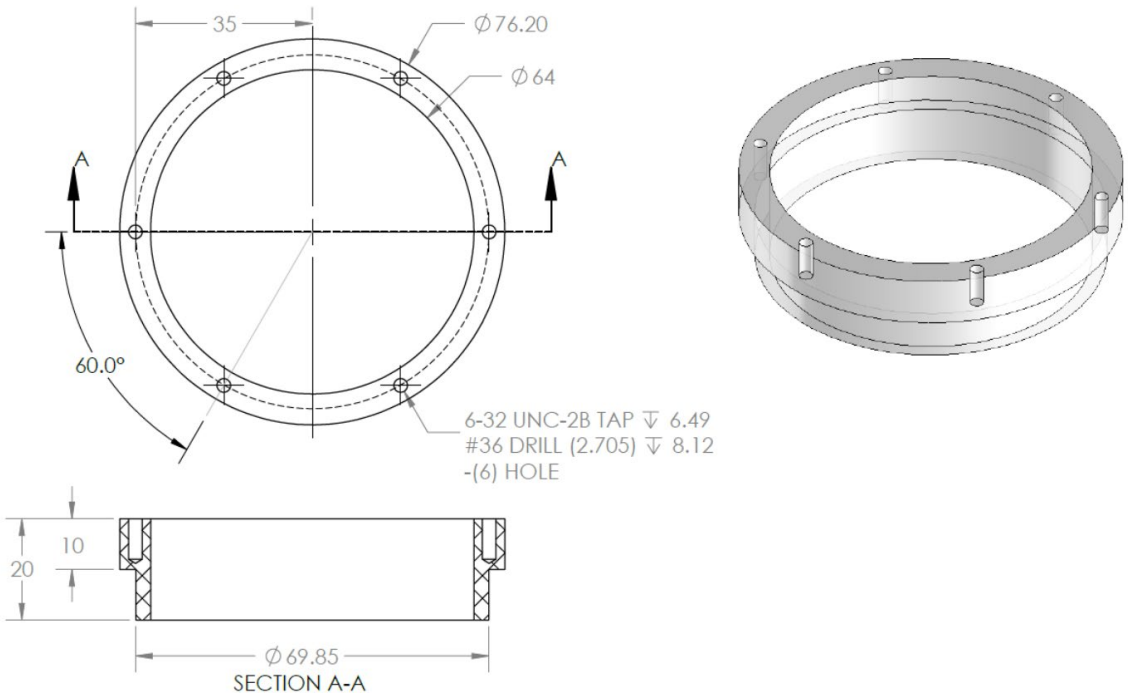

Figure D.4. Plenum bottom flange.

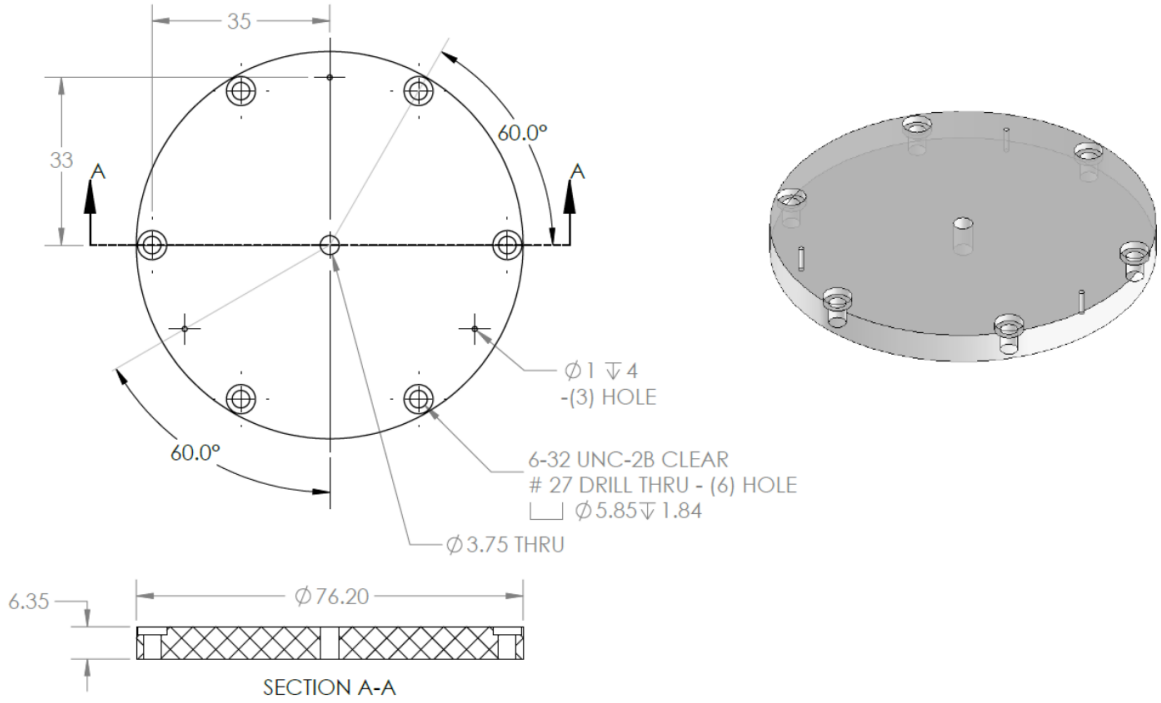

Figure D.5. Jet orifice plate.

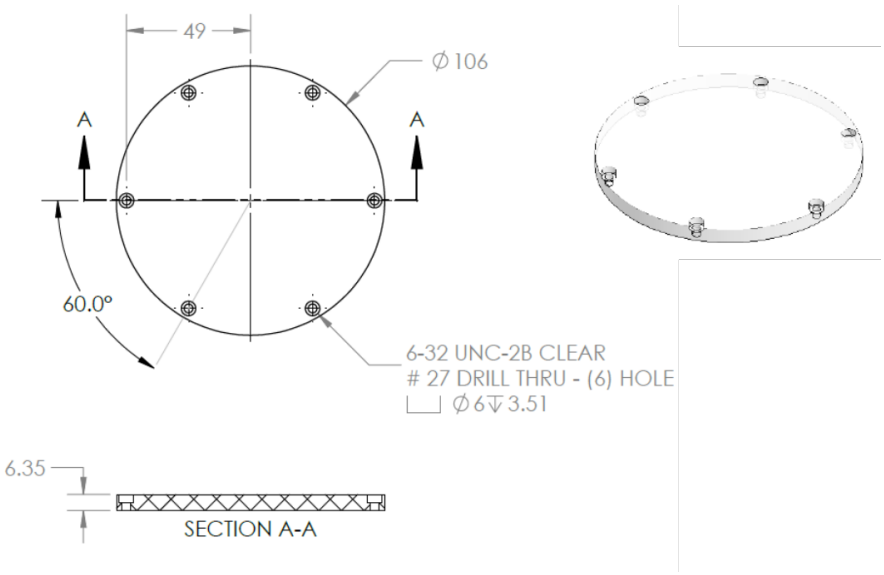

Figure D.6. Top viewing window.

VITA

Carolina Mira Hernández was born in Medellín, Colombia. She received her bachelor's degree in Mechanical Engineering in 2007, bachelor's degree in Engineering Physics in 2012 and master's degree in Mechanical Engineering in 2012 from EAFIT University, Colombia. She was a lecturer in the same institution for five years for undergraduate courses in Mechanical Engineering, including: fluid mechanics, thermodynamics, heat transfer and statics. She is as a recipient of the COLCIENCIAS (Colombian Administrative Department of Science, Technology and Innovation) fellowship for doctoral studies abroad. She studies the interactions of liquid-vapor interface dynamics with heat transfer and flow phenomena during boiling. In addition to phase change phenomena, her research interests include renewable energy systems and thermal energy storage. She participated in SERIIUS (Solar Energy Research Institute for India and the United States) exploring thermocline tanks as alternatives for thermal energy storage in concentrating solar power plants.

PUBLICATIONS

Mira-Hernández, C., Weibel, J. A., Garimella, S. V., "Visualizing near-wall two-phase flow morphology during confined and submerged jet impingement boiling to the point of critical heat flux," (In review)

Mira-Hernández, C., Weibel, J. A., Vlachos, P. V., Garimella, S. V., "Three-Dimensional Liquid-Vapor Interface Reconstruction from High-Speed Stereo Images during Pool Boiling," *International Journal of Heat and Mass Transfer*, (In press)

Mira-Hernández, C., Clark, M. D., Weibel, J. A., Garimella, S. V., "Development and Validation of a Semi-Empirical Model for Two-Phase Heat Transfer from Arrays of Impinging Jets," *International Journal of Heat and Mass Transfer*, vol. 124, pp. 728-793, 2018.

Mira-Hernández, C., Clark, M. D., Weibel, J. A., Garimella, S. V., "A semi-empirical model for two-phase heat transfer from arrays of confined impinging jets," presented at the *16th IEEE Intersociety Conference on Thermal and Thermomechanical Phenomena in Electronic Systems (ITherm),* Orlando, Florida, USA, pp. 90-97, 2017.

Hatte, S., Mira-Hernández, C., Advaith, S., Tinaikar, A., Chetia, U. K., Manu, K. V., Chattopadhyay, K., Weibel, J. A., Garimella, S. V., Srinivasan, V. and Basu, S., "Short and Long-Term Sensitivity of Lab-Scale Thermocline based Thermal Storage to Flow Disturbances," *Applied Thermal Engineering*, vol. 109, part B, pp.936-948, 2016.

Mira-Hernández, C., Weibel, J. A., Groll E. A., and Garimella, S. V., "Compressed-Liquid Energy Storage with an Adsorption-Based Vapor Accumulator for Solar-Driven Vapor Compression Systems in Residential Cooling," *International Journal of Refrigeration*, vol. 64, pp. 176-186, 2016.

Mira-Hernández, C., Flueckiger, S. M., and Garimella, S. V., "Comparative Analysis of Single- and Dual-Media Thermocline Tanks for Thermal Energy Storage in Concentrating Solar Power Plants," *Journal of Solar Energy Engineering*, vol. 137, no. 3, pp. 031012, 2015.

Mira-Hernández, C, Flueckiger, S. M., and Garimella, S. V., "Numerical Simulation of Single- and Dual-Media Thermocline Tanks for Energy Storage in Concentrating Solar Power Plants," presented at *SolarPACES*, Las Vegas, Nevada, USA, Energy Procedia 49: 916–26, 2013.